Design and Evaluation of a Fine-Resolution Radar for Mapping Near-Surface Layers Using Plane-Waves

by

Timothy P. Rink

B.S. Electrical Engineering

The University of Kansas, 2003

Submitted to the Department of Electrical Engineering and Computer Science and the Faculty of the Graduate School of the University of Kansas in partial fulfillment of the requirements for the degree of Master of Science.

Thesis Committee:

_____
Chair: Pannirselvam Kanagaratnam

_____
Sivaprasad Gogineni

_____
David Braaten

_____
Date Defended

The Thesis Committee for Timothy Rink certifies
that this is the approved version of the following thesis:

Design and Evaluation of a Fine-Resolution Radar for Mapping Near-Surface Layers Using Plane-Waves

Thesis Committee:

_____
Chair: Pannirselvam Kanagaratnam

_____
Sivaprasad Gogineni

_____
David Braaten

_____
Date Approved

ABSTRACT

More accurate estimates of snow accumulation fluctuations need to be established for validation of satellite measurements. To validate spaceborne altimeter measurements of mass trends, more information on the nature of spatial accumulation fluctuations is needed. Current methods using ice cores do not reveal enough information on accumulation fluctuations; they provide only mean accumulation and are prone to errors due to sparse sampling.

To aid in the interpretation of satellite data, a 12-18 GHz frequency-modulated continuous-wave radar has been developed to map near-surface layers with 3 cm vertical resolution to a depth of about 20 m. The system has been developed to be mobile and self-contained so that spatial variability of the accumulation over a large area can be characterized. The system employs the use of plane-wave illumination and wide bandwidth to discriminate layers and reject clutter from off-nadir surfaces. The fine-resolution radar has undergone testing in laboratories at the University of Kansas, as well as field experiments conducted at Summit, Greenland, in 2005. The data taken from the field experiment in Greenland have been analyzed and compared to models constructed from actual snow density profiles and stratigraphy taken directly from snow pits. Data processing algorithms have been developed and implemented which account for the system effects and conditions at time of measurement. Layer tracking software has also been developed to aid in the determination of accumulation rates for recent years.

The radar system has also been used at the WAIS Deep Divide in Antarctica during the 2005 field season, and will be used in future field experiments

To my amazing and loving wife, Stacia

ACKNOWLEDGEMENTS

I would like to extend my sincere thanks to both Dr. Pannir Kanagaratnam and Dr. Prasad Gogineni. Dr. Gogineni originally granted me work at the University of Kansas Remote Sensing Laboratory during my undergraduate studies. Work in my undergraduate degree laid the foundation for my invaluable opportunity to work under the supervision of Dr. Pannir Kanagaratnam in this thesis work. His guidance, teaching, and kind demeanor help make the thesis work a success and a greatly-appreciated learning experience. Many thanks are also owed to Mr. Torry Akins, who helped me with practical design work such as hands-on mechanical work, circuit board layout concepts and digital implementations. I would also like to thank Mr. John Paden who also helped with radar theory while juggling other students and his own Ph.D. research. Gratitude is owed to Dr. David Braaten for his help in data collection in the field, and his help with my geological understanding of the thesis work. I would also like to thank Mr. Gunashekar Jayaraman and Ms. Kirby Zimmerman for their help collecting layer information and digging snowpits during the Greenland field experiment. Finally, I would like to thank Mr. Paul Rink, who unknowingly fostered my interest and abilities while working in his machine shop; and I would like to thank Mr. Brandon Heavey and Mr. Bharath Parthasarathy for their valuable friendship, advice and knowledge, which has challenged me and influenced my development as an engineer.

This work was supported by grants from NASA (#NGT5-30508) and the National Science Foundation (#OPP-0230378).

TABLE OF CONTENTS

LIST OF FIGURES

LIST OF TABLES

CHAPTER 1

INTRODUCTION

1.1 Motivation for Studying Polar Ice

Global climate change is a concern that has been getting more attention over the last few decades, and there is great reason to investigate it. Climate change and sea rise have the potential to affect the millions of people who populate coastal areas [22]. Scientists need to better understand the physics of the global climate in order to understand how human actions affect the global environment. To make predictions, scientists have formulated models that predict past and future climate conditions. The polar ice sheets are a major source of variability in climate models [32]. The ability to investigate the internal content of the ice sheets, and the ability to track accumulation rates and ice sheet movements, will greatly aid in improving the accuracy of current mass balance estimates. Investigating deep layers in the ice sheet reveals information about accumulation and ice flow history, while the near-surface layers show recent accumulation. Information on the temporal and spatial distribution of snow accumulation rates is essential in quantifying the mass balance of an ice sheet.

The fine-resolution radar of this thesis work, developed at the University of Kansas, will help scientists better understand the internal content of ice sheets by imaging the top 20 m of ice and snow. The fine-resolution radar will implement a frequency-

modulated continuous-wave (FMCW) design, operating over the frequencies of 12-18 GHz to obtain 2.5 cm free-space resolution. Because only the upper layers are of interest, the transmit power was kept low, thus enabling the physical size of the radar to be kept small. The radar will be able to resolve layers at a fine resolution due to the wide bandwidth and the use of plane-wave target illumination. The use of plane-waves allows the radar to spatially filter out incoherent scattering from the distributed target area. The radar system will also serve other scientific missions. The radar will investigate small spatial fluctuations in accumulation, providing more information than just a mean measurement. The CryoSAT and ICESAT systems will use the data collected by the radar to verify data and concepts. The data collected by the radar will be compared to the data collected by ICESAT. The success of the radar will serve as ground truth for the CryoSAT mission; the radar can be bandwidth-limited post-process to directly compare measurements between CryoSAT and the radar.

1.2 Importance of Mass-balance and Accumulation Rate

Glaciers are a source of climate history, and information on layer depth and thickness provides a historical look back on the conditions of a glacier. Information on past glacier conditions can be used to help predict future conditions of glaciers and the climate as a whole [17]. While glaciers hold a vast amount of historical data, they also hold a vast amount of water. Complete melting of the world's ice sheets would result in a sea level rise of approximately 70 m [23]. Granted, it is highly unlikely that the glaciers will melt off completely, but sea level has been rising at about 1.8 mm per year, with global temperature rises as the primary suspected culprit [4]. Glaciers are extremely

sensitive to climate change, so it is natural to look to glaciers as an indication of the status of the global climate and as a contributor to sea level rise. One of the most important health indicators of a glacier is its mass balance [16]. Current methods for determining mass balance are prone to errors due to the sparse sampling of ice sheets. Errors in calculating the mass balance are caused chiefly by uncertainties in calculating accumulation rates over the ice sheets [32]. Sparse sampling of the ice sheets, using ice cores to determine the accumulation rate over a broad area, does not provide a good picture of the total accumulation over an area [20]. Data from the radar show that annual layers may vary as much as 20 cm in depth over a distance of 10 m. A better means of determining accumulation rate is needed.

1.3 Reasoning for Studying Near-Surface Layers

Better estimates of accumulation for ice sheets are needed to create more accurate mass balance assessments. Near-surface layers are of interest to climatologists and the scientific community because they contain information on accumulation rates of recent years. Hoar layers, which exist only in the first 10s of meters and form on an annual basis, create boundaries for annual accumulation [23]. Space-based altimeters alone cannot accurately determine the accumulation rate. Dibb et al. [5] have determined that compaction occurs over short periods of time, making altimeter estimates of accumulation rates difficult to use in mass balance calculations. By using a fine-resolution radar to find annual layers, the accumulation rate can be more accurately determined.

1.4 Objectives and Approach

The principle reasoning for this thesis work is to provide a more accurate solution to determining the accumulation rates by imaging the near-surface layers of polar ice sheets. The radar developed in this thesis work can also be used to verify measurements taken by ICESAT and CryoSAT, and to help interpret the data obtained with those satellites. Operational bandwidth was selected to include the operational bandwidth of CryoSAT instrumentation and to cover a wide bandwidth so as to achieve a theoretical resolution of less than 3 cm. The antenna system was chosen to produce a plane-wave for the purpose of reducing clutter from incoherent scattering.

The design was approached by investigating the problem of resolving near-surface layers, and then deriving systems requirements based on desired functionality, medium properties and environmental conditions. From the derived requirements, simulations were used to optimize the radar before construction and testing. In general, the most salient concerns to overcome were to operate over enough bandwidth to provide fine resolution, while operating in the same band as CryoSAT, and to minimize clutter seen from incoherent scattering. Primary design considerations were focused on the antenna system and the frequency synthesizer. System models were built using performance data taken from actual components. The final radar configuration was optimized according to models created in simulation software. Upon design finalization, the radar was assembled to fit into a small housing, mounting directly on the antenna. Component, subsystem and system-wide testing was completed in laboratory facilities at the University of Kansas. Field testing was also conducted at Summit Camp, Greenland in July 2005.

1.5 Organization

This thesis is organized into 7 chapters. Chapter 2 outlines the history of near-surface remote sensing as well as information on the connection between ICESAT, CryoSat and this thesis work. Also contained in chapter 2 is fundamental information about near-surface firn, and fundamentals about the operation of frequency-modulated continuous-wave radars as well as other electrical engineering and radar-related concepts. The system design is detailed in chapter 3, while chapter 4 encompasses the simulation, testing and implementation of the radar system. Chapter 5 outlines the techniques used to process the radar data, and the field experiment is discussed in chapter 6. The thesis is concluded in chapter 7 with a discussion on the outcomes of this thesis work and suggestions for future work.

CHAPTER 2

BACKGROUND

2.1 History of Internal Layer Remote Sensing

The technique of using microwave energy to extract information about ice is not a new concept; the idea was first pursued by US Army researchers after the pilots from the United States armed forces reported that radar altimeters gave erroneous altitudes when flying over ice. After being alerted to the possibility of using radio waves to find the thickness of glacial ice, the Scott Polar Research Institute at Cambridge University produced the first radar for sounding glaciers. As well as imaging the glacial ice surface and underlying bedrock, radars developed for sounding ice showed reflections from internal layering. Realizing the value of information on climate history gathered from layer data, scientist began to refine radars to specifically image internal layers [7].

Concentrated efforts specifically aimed at imaging internal layers of ice sheets arose in the early 1970s at the University of Munster. Vickers et al.. [30] produced a 1 ns pulse radar to determine stratigraphy, density and thickness. Development in internal layer imaging radars has continued to the present, using both pulse and frequency-modulated continuous-wave systems. Kanagaratnam developed two systems at the University of Kansas: one ground-based system in 1998 and another airborne system in

2001. The ground-based system, developed for imaging near-surface layers, provided a free-space resolution of 8.2 cm to a depth of approximately 300 m and operated over the frequency range of 170 – 2000 MHz. Using modeling and data collected from the ground-based system, the airborne system was developed for imaging internal layers. The airborne system operated over the frequency band of 600 – 900 MHz and provided 50 cm free-space resolution to a depth of approximately 100 m [14].

Researchers at the University of Kansas and other institutions continued development of fine-resolution radars to image annual and inter-annual layers. In 2003, Parthasarathy et al.. [26] developed a 500 – 2000 MHz radar designed to track accumulation layers to a depth of approximately 100 m with a free-space resolution of 10 cm. Table 2.1 contains a summary of radars developed at the University of Kansas. The University of Kansas is not the only institution developing fine-resolution radars. Arcone et al.. [2] at the US Army Engineer Research and Development Center used a 300 – 500 MHz short-pulse radar developed in 2002 to track accumulation layers at a resolution of 30 – 40 cm up to a depth of 90 m.

Year	Operating Frequency (MHz)	Free Space Resolution (cm)	Maximum Depth (m)
1998	170 – 2000	8.2	300
2001	600 – 900	50	100
2003	500 – 2000	10	200

Table 2.1: Internal layer imaging radars developed at KU.

The increased capabilities of radars are most notably due to component availability and advances in signal processing technology. Development of more technologies utilizing upper frequency bands in recent years has led to wider availability of high-bandwidth components. Using higher frequency bands makes obtaining wider

bandwidths more easily attainable, thereby increasing capabilities of resolution. Additionally, advances in digital technology have allowed for the development of radars with more sensitivity.

2.2 ICESAT and CryoSat Mission Support

One of the goals of the grant associated with this thesis work is to provide support to the ongoing missions of ICESAT and CryoSat. This thesis work will provide a better estimate of accumulation layer characteristics to aid in the validation of satellite data.

Ice, Cloud and land Elevation SATellite (ICESAT), designed by NASA, is an instrument designed to track yearly accumulation rates using a laser altimeter. The laser altimeter system aboard the instrument, Geoscience Laser Altimeter System (GLAS), is capable of detecting changes in accumulation at a resolution of approximately 1.5 cm/yr [10]. The radar constructed for this thesis research will be used to validate data taken by ICESAT and help interpretation of the data by providing ground truth measurements.

The CryoSat mission is a project under development by the European Space Agency (ESA) to help answer the question of whether global climate change is impacting the mass balance of the polar ice sheets. CryoSAT will track changes in surface elevation using a radar altimeter operating in the Ku band. The instrument can operate in a normal, low-resolution pulse mode, SAR and Interferometric SAR (InSAR) [6]. This thesis work will support the CryoSat mission by operating over the same frequency band. Although the radar in this thesis work will take data over a wider bandwidth, the operational bandwidth can be limited post-process to serve as a validation of data taken with the CryoSat instrument set.

Both the ICESAT and CryoSat space instruments are designed to observe changes in snow accumulation. The measurements taken with altimeters have measured fluctuations in elevation, but the nature of the fluctuations in the measurements is not precisely known. Information on spatial variation is needed in order to interpret the variations in altimeter measurements. Current sampling in Antarctica is severely lacking in spatial density, and measurements in Greenland are only a little more dense. The covariability of the fluctuation of accumulation is needed, and current ice core measurements only provide mean accumulation. The accumulation layer depth can be considered a random variable. Spatial covariance information on accumulation layer will quantify the spatial relationship of the fluctuations in layer thickness. This information will provide a better understanding of the measurements taken by the space-based altimeters. The current high-density measurements that are available to space-based altimeters do not have enough spatial resolution to determine nature of the accumulation fluctuations. [33].

The radar in this thesis work can provide high spatial density measurements to space-based instruments to help determine the nature of accumulation fluctuations.

2.3 Physical Properties of Near-Surface Layers

The characteristics of the near-surface layers of ice sheets are highly complex. The near-surface firn layers are, by nature, different from year to year. Specific weather patterns, which vary from season to season and year to year, each make their mark on the layer characteristics. As accumulation events occur, layers are compacted and pushed to greater depths; while individual layer stratigraphy varies, density profiles for locations

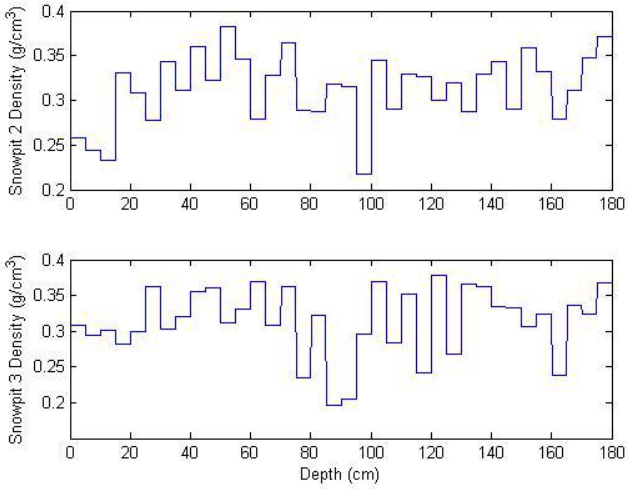

Figure 2.1: Density profiles from Greenland snowpits July 2005.

experiencing similar conditions remain somewhat similar. Winebrenner et al.. analyzed density from four snowpits dug up to depths up to 4 m at a sampling of 2 cm. The density profiles show that, while the trend tends toward the density of ice, there is little correlation between samples, with juxtaposed density measurements differing by as much as 0.075 g/cm^3 [32]. Stratigraphy and density measurements taken in Greenland during field work supporting this thesis suggest similar conclusions. Figure 2.1 shows density profiles of two snowpits. The two density profiles are somewhat similar, as

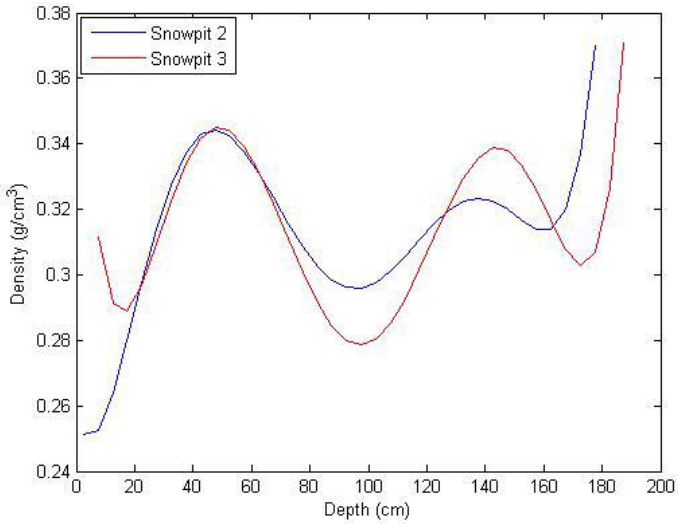

Figure 2.2: Density trend lines from Greenland snowpits July 2005.

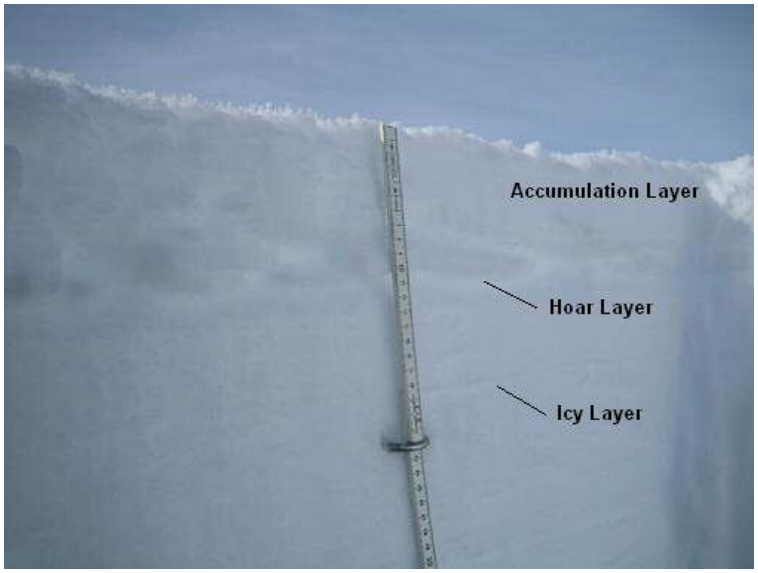

Figure 2.3: Stratigraphy from snowpit showing three firn characteristics.

clearly shown in Figure 2.2, while consecutive measurements vary as much as 0.125 g/cm^3.

The wildly differing densities are due to the physical structure of particular layers. As the density of the firn increases towards the density of ice with depth, layers ofdifferent structure still exist. While the molecular structure of these layers is beyond the scope of this thesis, the nature and formation of these layers will be discussed. Figure 2.3 shows accumulation layers observed in Greenland firn, July 2005. The most salient types of layers (for the purpose of this research) fall into three classes of firn: accumulation layers, icy layers and depth hoars.

The greatest amount of firn near the surface of the ice sheet falls into the recent accumulation category. Accumulation layers form directly from precipitation accumulating on the surface of the ice sheet. As more accumulation events occur, previous accumulations are buried and compacted deeper into the ice sheet, generally becoming more dense with greater depth. The weight of other accumulation layers is not the only action by which layers increase in density. Accumulation density can widely

vary from layer to layer. Heat flux can cause layers to change density and structure forming depth hoars, while high winds may cause icy crusts form. In addition to effects from heat flux and wind, firn density is dependent on initial particle size, while over time, the firn attempts to maintain the lowest energy structure. Despite the initial size or shape of the snow crystals, particles combine to form larger particles—reducing the overall surface area, and thus the energy of the structure.

Hoar layers are among the most visible layers in near-surface layers, as illustrated in Figure 2.3. Hoar layer formation is cased by sublimation of ice crystals when temperature gradients are large. Strong temperature gradients can form when surface air temperature is warmer than the near-surface layers [35]. Water vapor is exchanged from grain to grain, redistributing the density of the layers [34]. Hoar layers are much less dense than the surrounding layers and cause substantial reflections of electromagnetic energy in near-surface layers because of the large contrast in density compared to adjacent layers.

Icy layers account for only a small volume of the near-surface layers, but cover vast areas. Icy layers, or crusts, form under many conditions including precipitation, temperature and wind conditions. Although rain and melting does not occur in the dry snow region, mechanisms that form crusts in dry snow are kinetic heating and compaction. During periods of strong wind, kinetic energy is absorbed in the form of heat when ice and snow crystals blow across the surface of the ice sheet. This heating can cause a slight melting, which freezes to form a thin ice crust [36]. Crusts formed in this manner are often referred to as wind crusts or wind glaze. Ice crusts can also form barriers to sublimation, forming hoar layers just beneath the ice crust [18].

2.4 FMCW Radar Fundamentals

A frequency-modulated continuous-wave (FMCW) radar is an efficient and elegant implementation to achieve high-resolution with relatively low power.

The basic operation of an FMCW radar is to transmit a frequency-modulated transmit signal (commonly called a "chirp") and mix the time-delayed receive signal with transmit signal, which produces a sum and difference frequency. The difference frequency, or beat frequency, is related to the range of the target. After the transmit and receive signals are beat together, the IF signal is filtered to extract only the beat frequency. Figure 2.4 illustrates the transmit and received signals in an FMCW system.

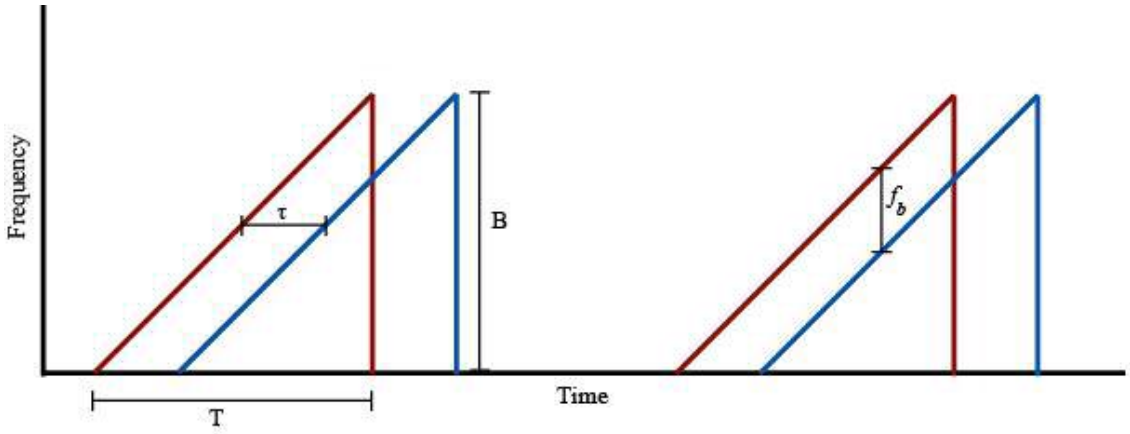

Figure 2.4: FMCW transmit chirp (red) and receive signal (blue).

In the above figure f_b is the beat frequency, T is the chirp time, B is the bandwidth of the chirp, and τ is the two-way time delay between the transmitter and the target. Using the geometry from the illustration in Figure 2.4, the following expression can be constructed:

$$f_b = \frac{B\tau}{T} \qquad [2.1]$$

Assuming that the signal travels at the speed of light, the transit delay can be related to the target range by:

$$R = \frac{c\tau}{2} \qquad [2.2]$$

An expression for the difference frequency, or beat frequency, relating to target range can be found by combining equations [2.1] and [2.2]:

$$f_b = \frac{2RB}{cT} \qquad [2.3]$$

Equation [2.3] shows that target range can be related to a beat frequency.

In the presence of multiple targets, the beat signal will be the superposition of multiple beat frequencies corresponding to the respective target distances. Using the Fourier transform, the beat signal can be used to determine range to individual targets. Since the chirp is finite in length, the spectrum of the beat frequency will not be populated by single delta functions, but with sinc functions of the form:

$$\text{sinc}\left(\frac{f - f_b}{T}\right) \qquad [2.4]$$

with zero crossings at T^{-1} constraining the minimum spacing between beat frequencies:

$$\Delta f_b = \frac{1}{T} \qquad [2.5]$$

Reordering equation [2.1] and using minimum spacing given by equation [2.5] gives the minimum resolvable two-way travel time:

$$\Delta\tau = \frac{1}{B} \qquad [2.6]$$

The resolution of an FMCW system can be found by using equations [2.2] and [2.6]:

$$\Delta R = \frac{c}{2B} \qquad [2.7]$$

Notably, the range resolution result of equation [2.7] corresponds with the equation governing the resolution of a traditional pulse radar system where B is the bandwidth of a pulse. According to equation [2.7], the range resolution of a radar system is inversely proportional to the bandwidth of the system. The simple pulse radar is the most intuitive approach for microwave remote detection of targets, but is usually not the most efficient use of resources. Although requiring the same bandwidth, frequency-modulated continuous-wave radars achieve the same resolution while utilizing resources such as power and data acquisition more efficiently. By using a continuous wave system, the target is under constant illumination. To illuminate a target with the same amount of power using a conventional pulse radar system requires that all the power contained in a chirp be contained in a single pulse. Additionally, the return pulse must be sampled over the entire bandwidth. It is unnecessarily costly to generate a high-powered, high-bandwidth pulse and to sample it with an A/D converter that runs at that bandwidth. The FMCW concept will enable high-resolution at a much lower cost, but will introduce range side lobes which can mask adjacent returns.

A time domain expression for the beat frequency can be derived. A frequency-modulated transmit signal can be expressed by the following equation:

$$V_t(t) = A\cos\left(2\pi f_0 t + \frac{\pi B}{2T}t^2 + \theta_0\right) \qquad [2.8]$$

where f_0 is the initial modulation frequency, θ_0 is the initial phase and A is an arbitrary amplitude. The transmit signal is transmitted into a medium, and upon encountering a boundary of differing dielectric composition located at a two-way travel time of τ, a portion of the signal is reflected back to the receiver. The expression for the reflected

signal is given below, assuming ideal system responses from the antenna, transmitter and receiver.

$$V_r(t) = A\left|\Gamma\left(f(t)\right)\right|\cos\left(2\pi f_0(t-\tau)+\frac{\pi B}{2T}(t-\tau)^2+\theta_0+\phi\left(f(t)\right)\right) \qquad [2.9]$$

where $|\Gamma(f(t))|$ is the frequency-dependent reflection coefficient and $\phi(f(t))$ is the frequency-dependent phase component of the reflection coefficient.

The range information is found by mixing the received signal with the original transmit signal. Multiplication of the two signals yields the following result (omitting the phase terms):

$$V_{IF}(t) = A^2\left|\Gamma\left(f(t)\right)\right|\Psi(t) \qquad [2.10]$$

where

$$\Psi(t) = \frac{1}{2}\left[\cos\left(\frac{\pi B}{T}t^2-\pi\frac{B\tau}{T}t+2\pi(2f_0)t+\frac{\pi}{2}\frac{B\tau}{T}\tau-2\pi f_0\tau\right)+\cos\left(\pi\frac{B\tau}{T}t-\frac{\pi}{2}\frac{B\tau}{T}\tau+2\pi f_0 t\right)\right]$$

Since only the beat frequency contains information about target range, the higher-order terms can be dropped (this is accomplished by a lowpass filter in system implementation); additionally, by using equation [2.1], V_{IF} can be related to the beat frequency to form the following expression:

$$V_{IF}(t) = \frac{A^2}{2}\left|\Gamma\left(f(t)\right)\right|\left[\cos\left(-\left[2\pi f_0\tau+\pi f_b t-\frac{\pi}{2}f_b\tau\right]\right)+\cos\left(2\pi f_0\tau+\pi f_b t-\frac{\pi}{2}f_b\tau\right)\right] \qquad [2.11]$$

Reducing and recalling phase terms yields an expression for the beat frequency:

$$V_{IF}(t) = A^2\left|\Gamma\left(f(t)\right)\right|\cos\left(2\pi f_0\tau+\pi f_b t-\frac{\pi}{2}f_b\tau-\phi\left(f(t)\right)\right) \qquad [2.12]$$

Equation [2.12] contains both amplitude and phase information about the target.

2.5 Effects of Modulation

In an ideal FMCW radar system, the transmit signal is a perfectly-linear chirp, increasing in frequency according to equation [2.8] and experiencing no fluctuations in amplitude over the time of transmit. Unfortunately, ideal transmit chirps cannot be implemented in real systems so it is necessary to investigate the effects of non-ideal modulation on FMCW radar system performance.

2.5.1 Amplitude Modulation

Amplitude modulation (AM) can severely limit the performance of a radar. Amplitude modulation of the transmit signal may be caused by reasons such as, but not limited to, constructive and destructive interference caused by poorly-matched components, gain variations in oscillator output and gain variations in amplification. Amplitude modulation of the transmit signal can cause characteristic AM sidelobes to appear in the beat frequency spectrum of the radar. If the modulation is severe enough, AM sidelobes may mask weaker target returns spaced closely to targets with stronger returns.

The effect of amplitude modulation on the transmit signal can be demonstrated mathematically. Assume the transmit signal of equation [2.8] is modulated by another signal, $x(t)$, with m being the modulation factor:

$$V_t(t) = (1 + mx(t))\cos\left(2\pi f_0 t + \frac{\pi B}{2T}t^2 + \theta_0\right) \qquad [2.13]$$

The reflected signal may be expressed as:

$$V_r(t) = (1 + mx(t-\tau))\cos\left(2\pi f_0 (t-\tau) + \frac{\pi B}{2T}(t-\tau)^2 + \theta_0 + \phi(f(t))\right) \qquad [2.14]$$

Following the same procedure used to find equation [2.12]:

$$V_{IF}(t) = \left[1 + mx(t) + mx(t-\tau) + m^2 x(t)x(t-\tau)\right]\cos\left(2\pi f_0 \tau + \pi f_b t - \frac{\pi}{2} f_b \tau - \phi(f(t))\right)$$

[2.15]

The effect on the beat frequency spectrum can be better appreciated by example. Assume the modulating signal is a single frequency sinusoid and that m is sufficiently small enough that the m^2 term can be ignored. Figure 2.5 shows the effects of amplitude modulation. The beat frequency is 5 kHz, the modulating signal is 100 Hz, the modulation index is 0.125 and τ is 0. Amplitude modulation sidelobes will be the largest when there is no delay between transmitted and received signals.

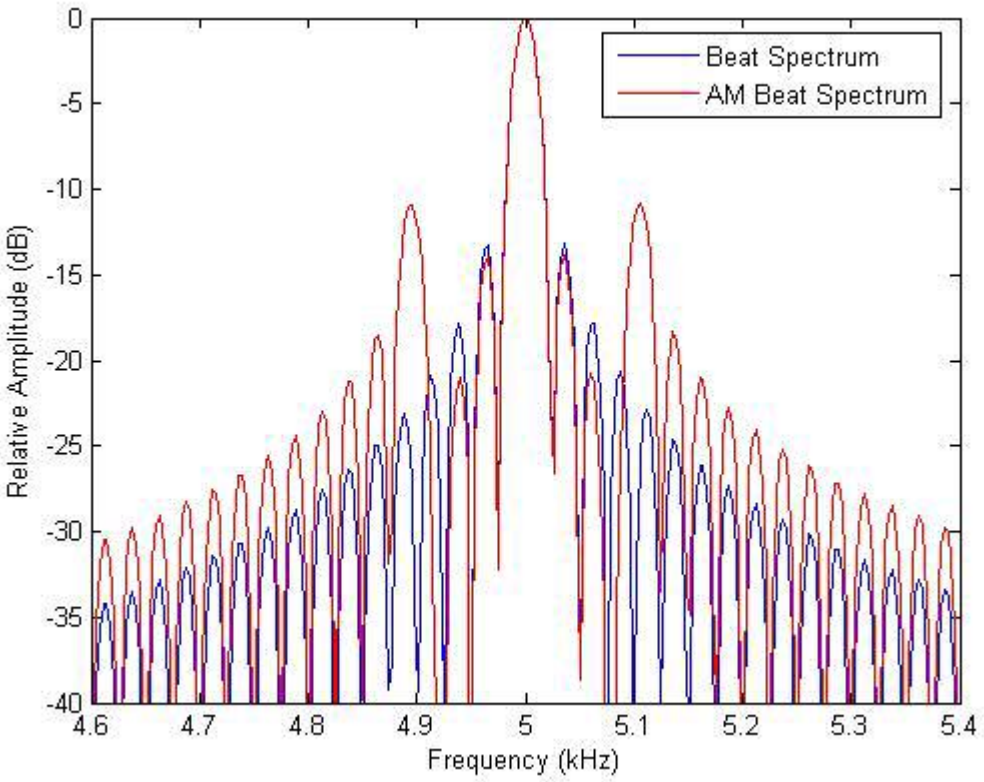

Figure 2.5: Effects of amplitude modulation on frequency spectrum.

2.5.2 Frequency Modulation

Frequency modulation can also severely degrade radar system performance. It is important to note that by system design, the radar transmit signal is frequency modulated, but non-ideal modulation creates additional sidelobes that degrade the beat frequency spectrum. Ideally, an FMCW sweep should be completely linear, following equation [2.8]. Most frequency modulation problems in an FMCW radar occur when the linear transmit sweep contains nonlinearities. Unwanted frequency modulation most easily occurs in FMCW systems though the transmit sweep generation. It is extremely difficult to account for all nonlinearities associated with an oscillator. Like amplitude modulation, unwanted frequency modulation can create sidelobes, which can mask weaker adjacent returns.

The effect of unwanted frequency modulation on the beat frequency spectrum can be demonstrated mathematically. Assume the transmit signal in equation [2.8] is frequency modulated by signal $\Delta\phi(t)$:

$$V_t(t) = \cos(2\pi f_0 t + \frac{\pi B}{2T} t^2 + \theta_0 + \Delta\phi(t)) \qquad [2.16]$$

The reflected signal may be expressed as:

$$V_r(t) = \cos\left(2\pi f_0 (t-\tau) + \frac{\pi B}{2T}(t-\tau)^2 + \theta_0 + \phi(f(t)) - \Delta\phi(t-\tau) \right) \qquad [2.17]$$

The received signal is multiplied with the instantaneous transmit signal to form lower-order terms derived earlier. An expression for the intermediate frequency signal can be formed by making a simplification that the frequency distortion during the time delay, τ, is linear, and ignoring any constant phase terms:

$$V_{IF}(t) = \cos(2\pi f_b t + \tau \frac{d}{dt}\Delta\phi) \qquad [2.18]$$

Using a model of white noise phase nonlinearity, it can be shown that the beat spectrum can be represented as [9]:

$$V_{IF} = e^{j2\pi f_b t}\left[1 + \sum_{i=1}^{\infty}\left(\frac{\beta}{2}e^{-j2\pi f_i t} - \frac{\beta}{2}e^{j2\pi f_i t}\right)\right] \qquad [2.19]$$

where $\beta = 2\pi f_\Delta \sqrt{2}\xi_n \tau$, ξ_n is the root-mean-squared noise voltage and f_Δ is the oscillator frequency sensitivity.

The effect of frequency modulation on the beat frequency spectrum can be shown in the frequency domain. Figure 2.6 shows the effects of unwanted frequency modulation of the transmit sweep. Assume that the rms noise voltage is 1 mV, the frequency sensitivity of the oscillator is 340 MHz/V and τ is 4 ns. Sidelobes are largest when τ is large.

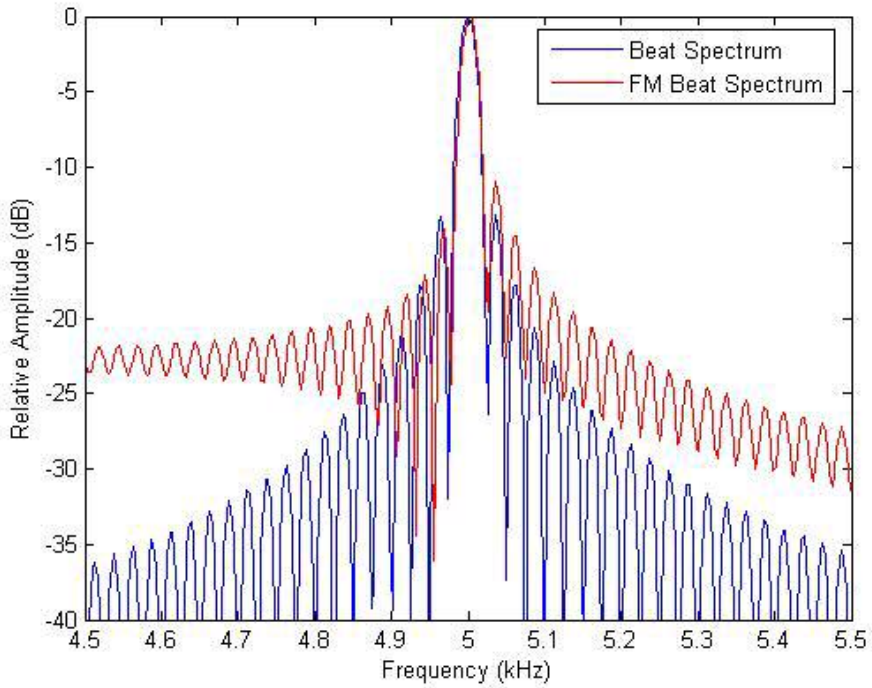

Figure 2.6: Effects of unwanted frequency modulation on frequency spectrum.

2.6 Layer Detection

Internal layering in ice sheets is a product of differing atmospheric conditions during accumulation events. These layers have different densities and conductivities caused by atmospheric contaminants or by melt events. Rising temperatures can cause a layer of snow and ice to melt, becoming denser as the temperature drops and it refreezes; volcanic eruptions can cause layers to become more acidic, changing the conductivity of the layer. These are two primary ways in which the electric properties of the layer can change (temperature is also an important factor). Near surface layers are generally dominated by dielectric changes caused by density differences, ruling any changes in conductivity insignificant. For our interest, it is important to note that these electrical changes result in a change in the permittivity of a layer; therefore, there will be dielectric contrasts from layer to layer. Dielectric contrasts cause reflections at the dielectric boundary according to the following equation [25]:

$$\Gamma = \frac{\sqrt{\varepsilon_{r2}} - \sqrt{\varepsilon_{r1}}}{\sqrt{\varepsilon_{r2}} + \sqrt{\varepsilon_{r1}}} 2\sin(\frac{2\pi l}{\lambda_m}) \qquad [2.20]$$

where ε_r is the relative complex permittivity of the respective layers, l is the thickness of layer two, and λ_m is the wavelength in layer two. These reflections caused by the contrast of permittivity between layers are exploited to return signal power back to a radar antenna. This is the physical electromagnetic mechanism which allows the remote sensing of the ice sheet internal layers.

2.7 Scattering and Clutter

In order to properly design a radar receiver and to interpret the returned signal to the receiver, something should be known about the way electromagnetic energy interacts

with the target and/or the target medium. Scattering is a term used to describe the way electromagnetic energy disperses when encountering an object. "Scattering" and "clutter" can be ambiguous terms at times; clutter for some systems may actually be targets for other systems, or vice versa. Clutter generally refers to reflected electromagnetic energy coming from objects other than the target(s) of interest.

When a target is illuminated, energy can be scattered in one or all directions. For a perfectly smooth surface, all incident energy is reflected back at the angle of incidence; this scattered energy is called specular, or coherent scattering. For rough surfaces, in addition to the specular return, some of the incident energy is reflected back in directions other than the angle of incidence; this scattered energy is called incoherent scattering. Both forms of scattering are illustrated in Figure 2.7.

For this system, the incoherent return is considered clutter; a parabolic dish antenna is used to create a very narrow beam to spatially filter out incoherent returns. The plane-wave radar's target of interest is the surface of an ice sheet. Although the internal layers of the ice sheet have relatively smooth boundaries, the surface of the ice sheet is rough compared to the operational wavelength. Because of the roughness of the

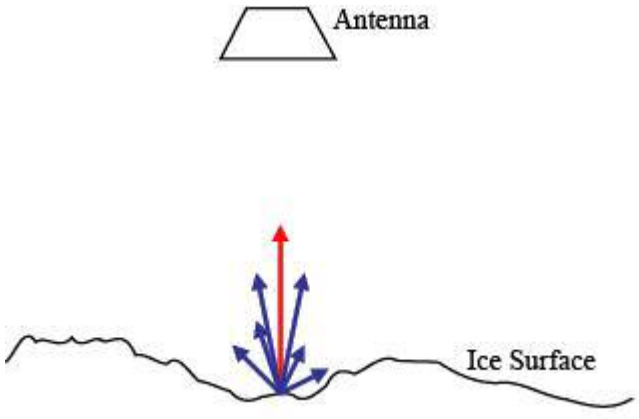

Figure 2.7: Scattering from rough surface. Coherent scattering (red). Incoherent scattering (blue). This figure assumes initial radiation towards nadir.

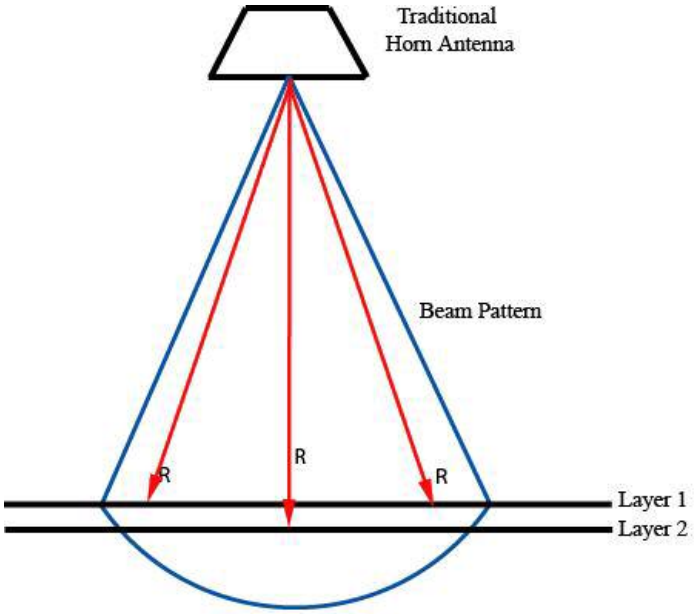

Figure 2.8: Horn antenna illumination. Spherical spreading causes energy returned from different layers to have the same travel time.

ice sheet surface, the transmit signal will be scattered in all directions. Figure 2.8 illustrates the need for a narrow-beam antenna. Using a conventional wide-beam antenna, scattered energy from the surface at off-nadir angles can experience the same time delay as energy returned from internal layers. Because time delay measurement is essentially the range measurement, the returns from the two targets cannot be distinguished from each other. Additionally, since the dielectric contrast between the surface of the ice sheet and the air is stronger than the internal layer dielectric contrasts, the return from the surface will be much stronger than the internal returns. These stronger surface returns will mask internal layers. In order to resolve the internal layers with fine resolution, the surface clutter must be reduced. This can be done by using a very narrow beam antenna which will not receive signals which are incoherently scattered.

2.8 Plane-Wave Illumination

Plane-wave illumination of the target area will ideally eliminate layer resolution problems caused by incoherent scattering. The radar in this thesis work uses a parabolic reflector to accomplish plane-wave illumination. The geometry of the plane-wave antenna is shown in Figure 2.10.

Traditional horn antennas have a radiation pattern that is generally conical, with the phase front expanding spherically. A typical radiation pattern for a traditional horn antenna is shown in Figure 2.9. Although a horn antenna configuration does not provide plane-wave illumination in the near field, a traditional horn antenna can be used in conjunction with a parabolic reflector to approximate plane-wave illumination. Figure 2.8 shows a horn antenna as a feed antenna to a parabolic reflector. The parabolic dish acts to reflect the spherically spreading wave originating at the focal point of the reflector into a plane-wave. The conversion of a spherical wave into a plane-wave is not perfect because of the finite nature of the parabolic reflector. Wave fronts reflecting from the

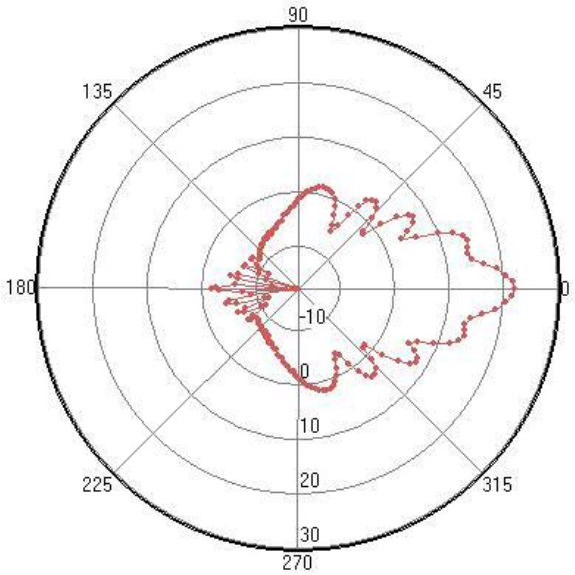

Figure 2.9: Typical gain pattern for a horn antenna. [29]

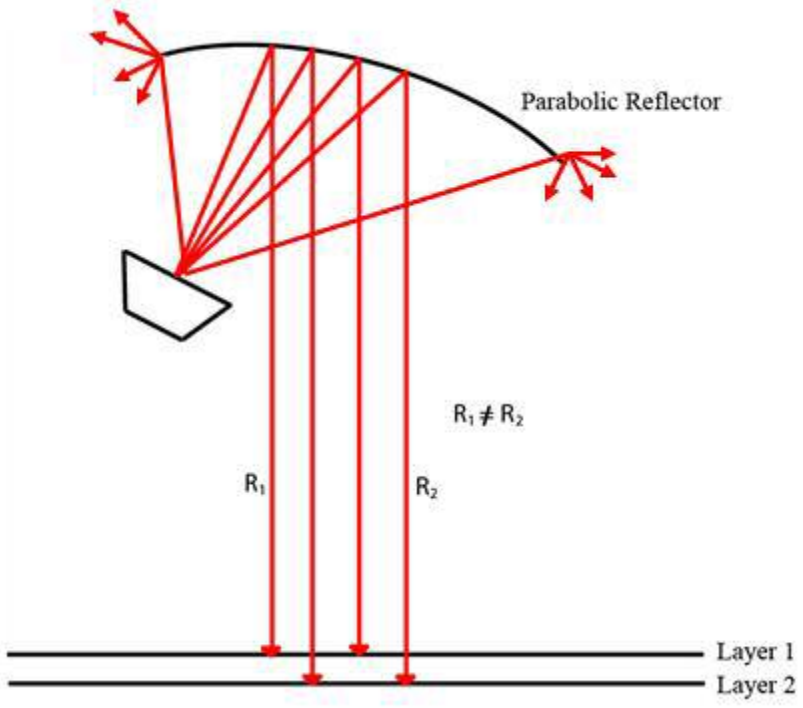

Figure 2.10: Plane-wave illumination using a parabolic reflector. Returns from individual layers do not share the same travel time.

parabolic dish can be dispersed due to diffracting fields from the edge of the dish, aperture blockage from the feed horn arm and feed spillover. Figure 2.10 illustrates how rays near the edge of the reflector dish get diffracted, contaminating the equal-phase wave front. Pistorius et al.. [27] have documented problems with plane-wave illumination arising from the finite nature of a parabolic reflector. Serrated or rolled edges and the use of absorber material to solve the problem of diffracting fields have been investigated by Johnson et al. [12]

Because there is no spherical spreading associated with a plane-wave, ideal plane-wave illumination should expect to see no spreading loss. Spreading loss for conventional antennas is r^{-2}, where r is the radius from the point of origin.

CHAPTER 3

SYSTEM DESIGN

3.1 Introduction

The design of any electrical system starts with understanding the objective or problem that the system needs to solve. Once an approach for solving the problem is established, requirements for the system can be derived. Electrical design must take into account conspicuous requirements such as power consumption, signal-to-noise ratio, link budget and bandwidth requirements. System design also includes less obvious constraints such as product availability, component lead-time, durability, cost and manufacturability.

In addition to the electrical concerns in system design, system engineering must keep in mind the mechanical constraints such as portability, practicality and size limitations. When designing at the circuit board level, the designer must keep in mind issues such as temperature, heat dissipation, mounting and many others.

The design of ground-penetrating radar systems also includes the distinction of considering interactions between electromagnetic energy and the target medium. In order to properly design a radar receiver, something must be known about the target medium in order to properly handle returned signals.

The radar design in this thesis work starts with identifying overall system requirements and then deriving individual subsystem requirements.

3.2 System Design Considerations

Radar system design considerations include system-level requirements, component interactions and derived requirements based on the target medium.

3.2.1 System-Level

The system-level design considerations are based on fundamental goals of system use. The driving design consideration for overall system design for this thesis work is the detection of near-surface layers in firn by use of a ground-based mobile system; system-level design requirements will be derived from those goals. The derived system requirements are largely driven by determining the power necessary to detect internal layers. System-level requirements center on providing a sufficient level of signal-to-noise ratio (SNR) to detect layers. The system block diagram is pictured in Figure 3.1.

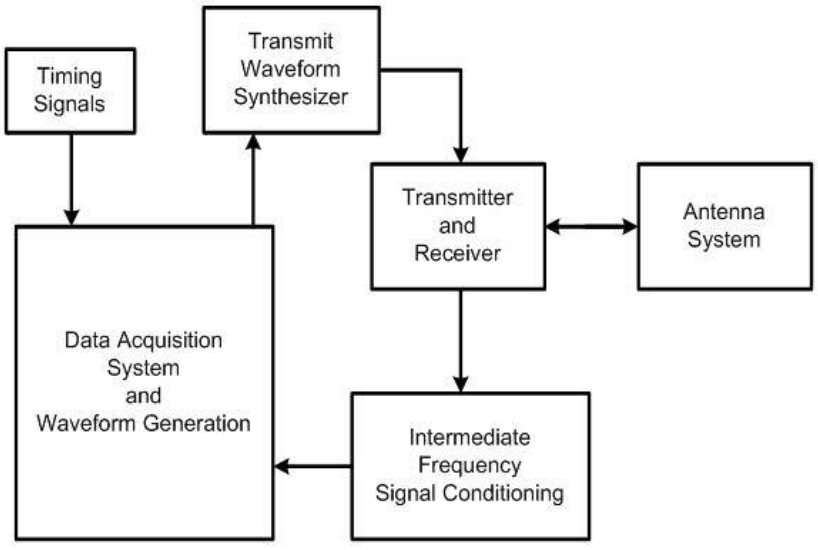

Figure 3.1: System block diagram.

The data acquisition (DAQ) system uses a 12-bit analog-to-digital (A/D) converter. The SNR for an A/D converter follows the expression:

$$SNR = \frac{3\left(2^{2N}\right)}{2} = 10\log\left(\frac{3\left(2^{2(12)}\right)}{2}\right) \approx 74 \text{ dB} \qquad [3.1]$$

where N is the number of bits in the A/D quantizer. The maximum voltage level that can be digitized in the DAQ is 0.5 V_p [1]. Assuming a 50 Ω system, the maximum DAQ power level follows:

$$P_{\max} = \frac{V_p^2}{2R} = \frac{0.5^2}{2(50)} = 2.5 \text{ mW} \approx 4 \text{ dBm} \qquad [3.2]$$

The corresponding noise A/D noise floor is approximately -70 dBm.

The radar system noise floor minimum is constrained by the ambient system noise. The minimum system noise floor follows the expression:

$$N = kTBF \qquad [3.4]$$

where T is the ambient temperature in Kelvin, k is Boltzmann's constant (1.38×10^{-23}), B is the bandwidth of a single range bin and F is the receiver noise figure. The bandwidth of a single range bin can be expressed:

$$B_{bin} = \frac{f_s}{N_{DFT}} \qquad [3.5]$$

where f_s is the DAQ sampling rate and N_{DFT} is the number of discrete Fourier transform (DFT) points before zero padding. The DAQ system sampling rate is 5 MHz. Since we are only interested in data acquired during the transmit sweep, the number of DFT points will follow:

$$N_{DFT} = Tf_s \qquad [3.6]$$

where T is the transmit signal sweep time. Combining equations [3.5] and [3.6] yields a

simple equation for the bandwidth of one range bin:

$$\frac{1}{T} = 1 \text{ kHz} \qquad [3.7]$$

The noise figure in equation [3.4] must be found using the Friis equation:

$$F = F_1 + \sum_{n=2}^{N} \frac{F_n - 1}{\prod_{i=1}^{N-1} G_i} \qquad [3.8]$$

The noise floor calculation includes only the receiver components. Table 3.1 details the components included in the noise floor calculation and lists their electrical specifications. The noise figure of a lossy component is equal to the component loss. The noise figure calculation will not include information from the antenna.

Component	**Gain (dB / Linear)**	**Noise Figure (Linear)**
Attenuator	-3 / 0.50	2.00
Circulator	-0.5 / 0.89	1.12
Attenuator	-20 / 0.01	100
Mixer	-6.5 / 0.22	4.47

Table 3.1: Front-end receiver component specifications.

Using the specifications from Table 3.1, the noise figure of the front-end receiver components can be calculated:

$$F = 2 + \frac{(1.12-1)}{0.5} + \frac{(100-1)}{(0.5)(0.89)} + \frac{(4.47-1)}{(0.5)(0.89)(0.01)} \approx 30 \text{ dB} \qquad [3.9]$$

Using the values found in equations [3.7] and [3.9], the noise floor of equation [3.4] can be found. From equation [3.4], the minimum detectible signal is -114 dBm.

Radar systems using traditional horn antennas can expect to receive valid data for any signal detectible above the noise floor. Since this radar uses a parabolic reflector to

launch plane-waves, the depth penetration limit is ultimately dependent on the validity of the equal-phase wave front. A plane-wave launched from a parabolic reflector remains a plane-wave over the distance governed by the following equation [3]:

$$d_{pw} = \frac{A^2}{2\lambda} = \frac{0.9^2}{2(0.02)} = 20.25 \text{ m} \qquad [3.10]$$

where λ is the operational wavelength and A^2 is the aperture of the antenna. The aperture of the antenna is 90 cm and the wavelength at 15 GHz is 2 cm. Using equation [3.10], exclusive layer information will only come from depths of 20.25 m or less. After that distance, the wave front begins to experience spherical spreading, and the radar will begin to receive incoherent returns as well. Annual layers will still be detectible past this depth if the nadir return is stronger than the incoherent returns at the same time delay.

The radar signal also experiences loss as it travels through the firn. The attenuation due to scattering and absorption can be calculated using the following equation [14]:

$$\alpha = e^{2R\kappa_e(f)} \qquad [3.11]$$

where R is the range to the target and $\kappa_e(f)$ is the frequency dependent extinction coefficient. The attenuation experienced by frequencies in the Ku band is estimated to have a maximum of about 0.5 dB/m. This estimate includes extinction due to both scattering and absorption. The attenuation is dependent on frequency, which is illustrated in Figure 3.2. The surface reflection is estimated to be about 15 dB. Power reflection from the depths of about 20 m must also be taken into account. Using density data from Summit camp and GISP2 sites in Greenland, the reflection coefficient may be as high as 24 dB between layers when the reflection is from hoar boundaries. A note of caution should be noted when calculating the reflection coefficient for depths in near-surface

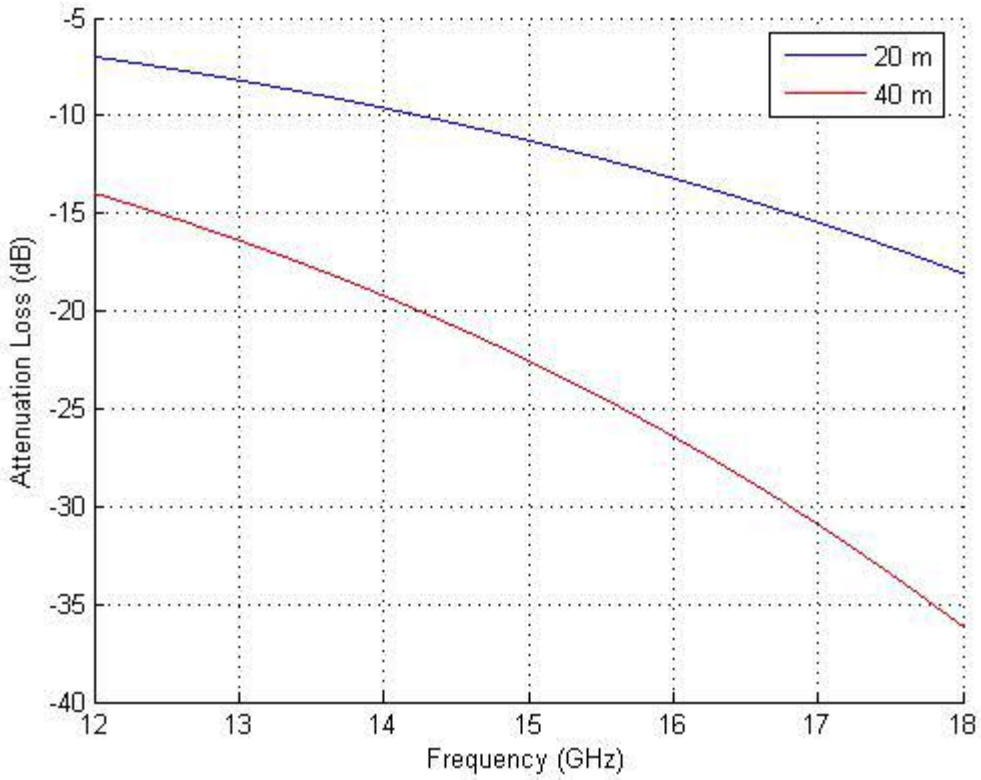

Figure 3.2: Expected attenuation through firn.

layers; this figure is very hard to estimate, given that the density of near-surface layers is not strongly correlated to depth.

Ignoring the degradation of the plane-wave over distances more than 20.25 m, the maximum range is also limited by the sampling rate of the DAQ. The sampling rate of the DAQ is 5 MHz, which limits the beat frequency to about 2 MHz. After 2 MHz, which is about 20% below the Nyquist rate, aliasing will begin to occur. Assuming a relative dielectric constant of 1.6, a beat frequency at 2 MHz will correspond to a depth

Depth (m)	Maximum Expected Attenuation (dB)
20	18
40	36

Table 3.2: Expected signal attenuation.

of about 40 m. Table 3.2 shows the expected signal attenuation.

The SNR of the received signal can be enhanced by integrating sweeps. Coherent integration provides an improvement in SNR by reducing the noise floor according to the following equation:

$$G_{\text{int}} = N \qquad [3.12]$$

where N is the number of coherent integrations. The system in this thesis work uses 10 coherent integrations, providing a gain of 10 dB.

The system power can be evaluated using the information on loss gathered. Ignoring the antenna gain, the necessary receiver gain, G_{rcvr}, may be found using the following expression:

$$S + P_t + G_{int} + G_{rcvr} > \text{A/D Noise Floor} + \text{SNR} \qquad [3.13]$$

Using the limiting amplifier as the main transmitting amplifier, the transmitter outputs a power of 10 dBm. Using a depth of 20 m, and if a 20 dB minimum SNR is wanted, the receiver gain needed according to equation [3.13] is -13 dB. The limiting amplifier will have enough power to reach 20 m with no gain from the receiver. For interest's sake, the calculation can be done for the maximum depth of 40 m. Equation [3.13] indicates $G_{rcvr} > 5$ dB.

The intermediate frequency (IF) amplifier has a gain of 42 dB, and the front-end receiver has a loss of 30 dB. The total gain of the receiver is 12 dB, which is unnecessary for the detection of coherent data in the first 20 m, but used to better utilize the available dynamic range. The IF amplifier gain may not be sufficient to clearly detect layers to a depth of 40 m if there is not a strong return from deep layers (such as a hoar

layer), but a good SNR is not needed at depths much beyond 20 m due to the uncertainty in the structure of the phase front.

The frequency of operation for the radar is chosen to be 12 – 18 GHz, which is in the Ku band. Use of frequencies in the Ku band allows the results obtained with this radar to be directly compared to measurements taken by CryoSat.

Signals which feed through the circulator from the transmitter to receiver, as well as reflections from the antenna, antenna structure and sled, will contribute large amounts of power to the beat spectrum. In order to keep the beat frequencies at very low frequencies, a short cable length is employed. A short cable length will incur only a small delay to system internal reflections and be easier to filter. To facilitate the use of a small cable, the radar transmitter and receiver are located on the feed arm of the parabolic reflector. The cable connecting the radar to the feed horn is only 4 inches in length.

3.2.2 Frequency Synthesizer

The frequency synthesizer consists of a phase-locked loop (PLL), operating from 12 – 18 GHz. Sweeping over this band of frequencies will afford 6 GHz of bandwidth, providing a maximum resolution capability of 2.5 cm. Also by using these frequencies of

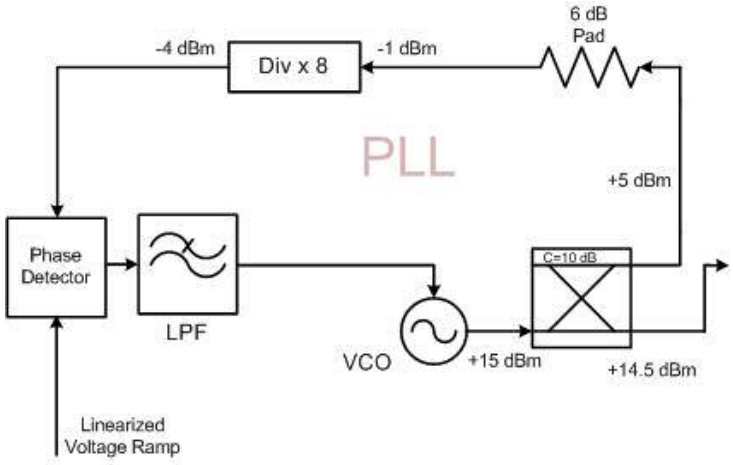

Figure 3.3: Frequency synthesizer block diagram.

operation, any harmonics generated by the oscillator will be out of band. The block diagram for the frequency synthesizer is in Figure 3.3.

The frequency synthesizer uses a phase-locked loop to implement the transmit sweep. The main oscillator is a 12 – 18 GHz voltage controlled oscillator (VCO). The tuning curve of the VCO is not linear as a function of voltage, so if the VCO is swept with a linear control voltage, the frequency modulation of the transmit sweep will not be sufficiently linear. As shown in section 2.5.2, non-linear frequency modulation can severely degrade the performance of the radar. The PLL is used in conjunction with a highly-stable, low-frequency oscillator to produce a highly-linear 12 – 18 GHz transmit sweep. The highly-stable reference sweep is a 10 – 15 MHz chirp generated from the data acquisition system utilizing a direct digital synthesizer (DDS) [1].

Since the radar system is mobile, it is necessary to consider the maximum velocity of the radar when specifying a pulse repetition frequency (PRF) and transmit sweep rate. It is necessary to maintain sweep correlation while the radar is in motion so that the radar area of illumination does not change too much during a single sweep duration. The following expression governs the minimum PRF of a mobile monostatic radar:

$$PRF = \frac{4v}{\lambda} \qquad [3.14]$$

where v is the radar velocity. The PRF is chosen to be 700 Hz and shortest free-space wavelength (18 GHz) is about 16.7 cm. Equation [3.14] dictates that the radar may travel at a maximum velocity of 2.92 m/s (10.5 km/h). The frequency synthesizer has also been designed with other projects at the University of Kansas in mind. The snow radar project (NASA grant #NGT5-30508) is an airborne radar experiment, which will utilize the

frequency synthesizer developed in this thesis work. A high PRF will allow a better SNR to be obtained through integrations.

The number of integrations that can be performed follows the expression [31]:

$$N \leq \frac{f_p \sqrt{2h}}{2v} \qquad [3.15]$$

where N is the number of integrations, f_p is the pulse repetition frequency, v is the radar velocity and h is the height of the antennas above the ground. Equation [3.15] shows that the number of returns that can be integrated is directly proportional to the PRF. The system is flexibly designed so that a small adjustment in the loop filter will allow for sweeps as fast as 500 µs and a PRF of 1 kHz.

The main components of a PLL are the VCO, frequency divider, phase comparator and loop filter. The PLL in this thesis work also includes an amplifier circuit used as a signal conditioner for the VCO. A detailed block diagram of the PLL, showing component details, is pictured in Figure 3.4.

The oscillator used for the PLL is a 12 – 18 GHz VCO from Sivers IMA with a tuning voltage ranging from 0 – 20 volts. The VCO has a slew rate of 80 GHz/µs and a modulation bandwidth of 13 MHz, so it is more than capable of achieving the necessary sweep rate for both the airborne snow radar and this thesis work. The output power of

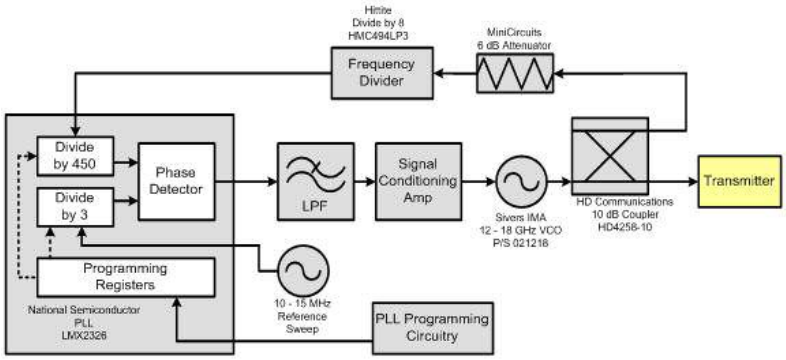

Figure 3.4: PLL Detailed block diagram.

the VCO is about 16 dBm, which will be more than sufficient for the radar.

The VCO output is fed into a directional coupler so that the output may continue to the transmitter section and also be fed back to the phase comparator to maintain lock to the reference chirp. The directional coupler is a connectorized component, and was chosen due to the unavailability of high-quality surface-mount couplers in the Ku band. The size of the coupler is reasonably small, so it does not preclude mounting of the radar on the antenna feed arm. The direction coupler is manufactured by HD Communications, HD4258-10. The coupler provides 10 dB coupling over 4 – 18 GHz.

The PLL chip used, National Semiconductor LMX2326, has a maximum input frequency of 2.8 GHz. The VCO outputs a maximum frequency of 18 GHz, so an external divider is necessary to reduce the frequency before it enters the internal divider in the PLL chip. The external frequency divider is the Hittite HMC494LP3, which is a divide-by-eight divider and has a bandwidth of DC – 18 GHz. The optimum input power to the divider is around 0 dBm, so an external attenuator is used to reduce the signal power to that level. The circuit schematic for the divider circuit is pictured in Figure 3.5. The HMC494LP3 is a single-supply chip, so DC blocking capacitors are used on all the inputs and outputs. Additionally, a terminating 50 Ω resistor is used to terminate the negative differential output in order to maintain proper matching, while utilizing only one of the divider differential outputs.

The output of the frequency divider is fed into the PLL chip for comparison to the 10 – 15 MHz reference chirp. Figure 3.6 shows the schematic for the LMX2326. The divider output and the reference sweep are not directly compared by the PLL phase detector; both signals are divided by dividers internal to the PLL chip. The dividers are

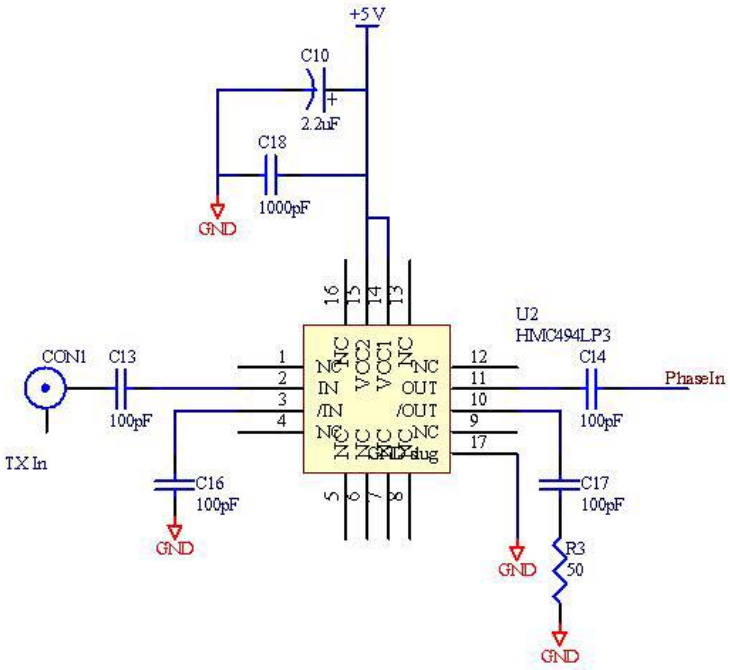

Figure 3.5: Schematic diagram of the divider circuit.

programmable, but must be programmed according to several guidelines. The following conditions govern the programmability of the internal dividers in the PLL chip:

$$B = floor\left(\frac{N}{32}\right) \qquad [3.16a]$$

$$A = N - 32 \cdot B \qquad [3.16b]$$

$$(B \geq A) \bullet (B \geq 3) \bullet (B \leq 8191) \qquad [3.16c]$$

where N is the frequency divider factor for the oscillator feedback. The minimum divisor for the reference oscillator divider is 3; and finally, the maximum phase detector frequency is 10 MHz. The above constraints are imposed by the setup of internal programming registers in the LMX2326. Additionally, the number of corrections the PLL phase detector can make is proportional to the input frequency of the phase detector. A faster lock time can be accomplished by inputting higher frequencies into the phase detector. Using the above constraints, the internal reference divider is chosen to divide

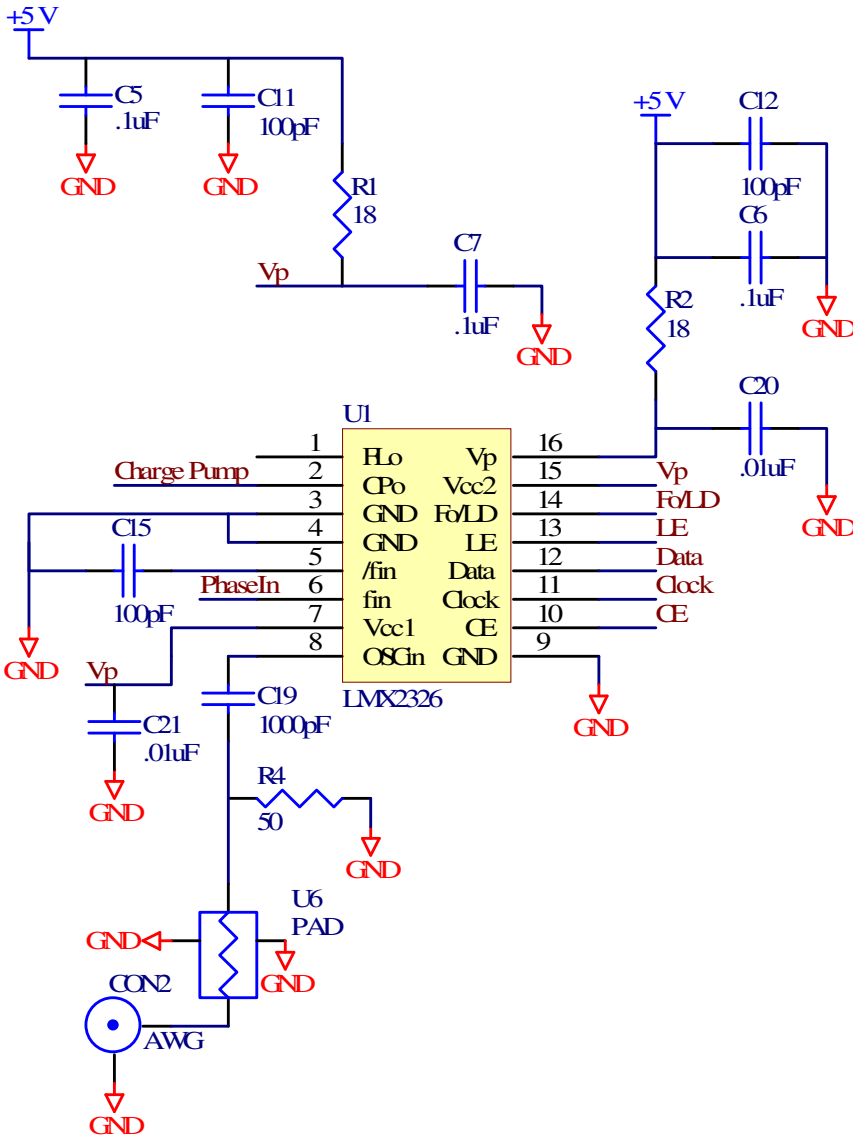

Figure 3.6: Schematic for the LMX2326 PLL chip.

by 3, and the internal oscillator divider is chosen to divide by 450; as a result, the phase detector uses a comparison sweep of 3.34 – 5 MHz.

The phase comparator of the LMX2326 is a tri-state device, which sinks and sources current to correct for phase errors between the reference and oscillator. The specification in the data sheet states that the sink and source currents are both 1 mA. In the case where the oscillator phase is lagging the reference phase, the phase comparator sources current; conversely, when the oscillator phase is leading the reference phase, the

phase comparator sinks current to reduce the phase of the oscillator. The third state is where the phase comparator neither sinks nor sources current. This happens when the phases of the reference and oscillator are matched. In effect, the output impedance of the phase comparator is very high in the off state.

As stated above, the phase comparator runs at a maximum speed of 5 MHz. The bandwidth of the phase comparator is actually larger than the output frequency because the phase comparator outputs a square wave. The square-wave output of the phase comparator contains all the harmonics associated with a square wave. The bandwidth is much too large to control the VCO; if the VCO is controlled with such a large bandwidth, the output oscillates around the reference, and never completely locks.

To limit the bandwidth of the phase comparator, a lowpass filter is used to cut out the higher frequency components of the error voltage. The lowpass filter preceding the phase comparator, known as the loop filter, is arguably the most crucial design task of the phase-locked loop. The loop filter must be designed to have enough bandwidth to be able to adjust quickly to phase errors, but not have so much bandwidth as to allow the error voltage to oscillate. The loop filter implements a three-pole, RC lowpass filter. The schematic is shown in Figure 3.7. The final component values were arrived at using simulations to optimize the lock time and stability.

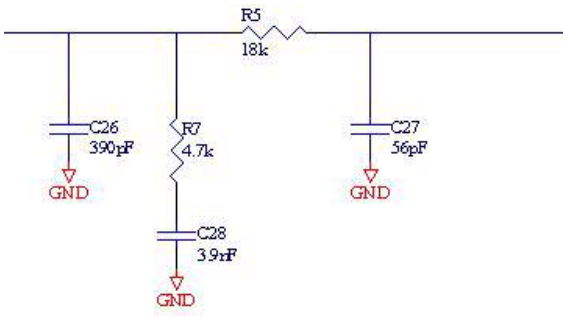

Figure 3.7: Loop filter schematic.

The LMX2326, and thus the internal phase comparator, operates on a single supply of 5 V. As mentioned before, the main oscillator has a tuning voltage range from 0 – 20 V. The phase comparator cannot develop a high enough voltage to control the VCO, therefore a signal conditioning circuit has been designed to boost the phase comparator output from 0 – 5 V to 0 – 20 V. This is accomplished using an operational amplifier in a simple non-inverting configuration. The schematic for the loop filter is shown in Figure 3.8. A filtering capacitor is added to the feedback loop to limit the amplifier bandwidth. The operational amplifier used is the AD8033, manufactured by Analog Devices. This operational amplifier was chosen for its low cost, bandwidth and ability to operate rail-to-rail under single-supply conditions. The VCO does not need negative tuning voltages, so there is no need to use a negative supply for the operational

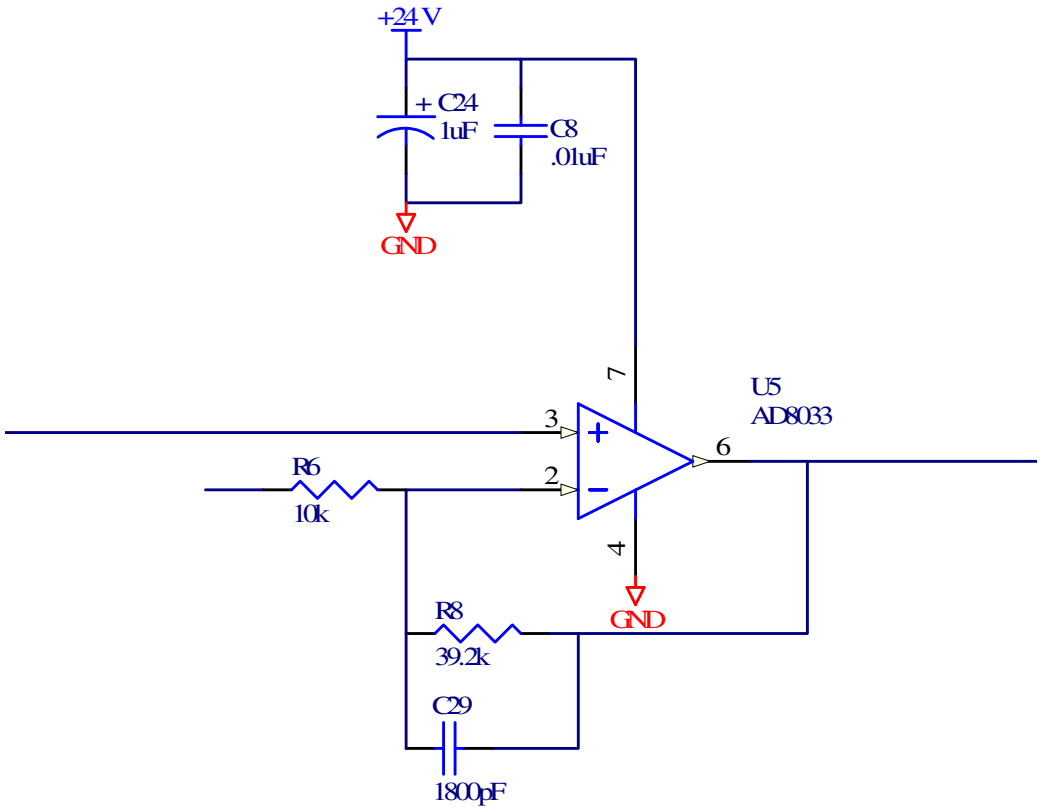

Figure 3.8: Loop amplifier schematic. The amplifier is used to condition the output signal from the phase comparator to the correct oscillator tuning voltage.

amplifier. An operational amplifier in the non-inverting configuration provides voltage gain according to the following expression:

$$v_o = v_i\left(1+\frac{R_2}{R_1}\right) \qquad [3.17]$$

where v_o is the output voltage, v_i is the input voltage, R_1 is the series resistor and R_2 is the feedback resistor. Following equation [3.17], the phase comparator will be able to ideally supply 24.6 V to the VCO control pin. Output current is not a consideration since the VCO consumes almost no tuning current (on the order of μA) and the operation amplifier is able to source over 3 mA of current. The amplifier circuit will not realize the full 24.6 V capacity because it is supplied by a 24 V source voltage.

The LMX2326 is fully programmable. There are three registers that need to be programmed after power is applied to the chip. The registers are volatile memory, so the chip must be programmed after every power cycle. The programming of the chip is done utilizing a complex programmable logic device (CPLD). The programming circuitry,

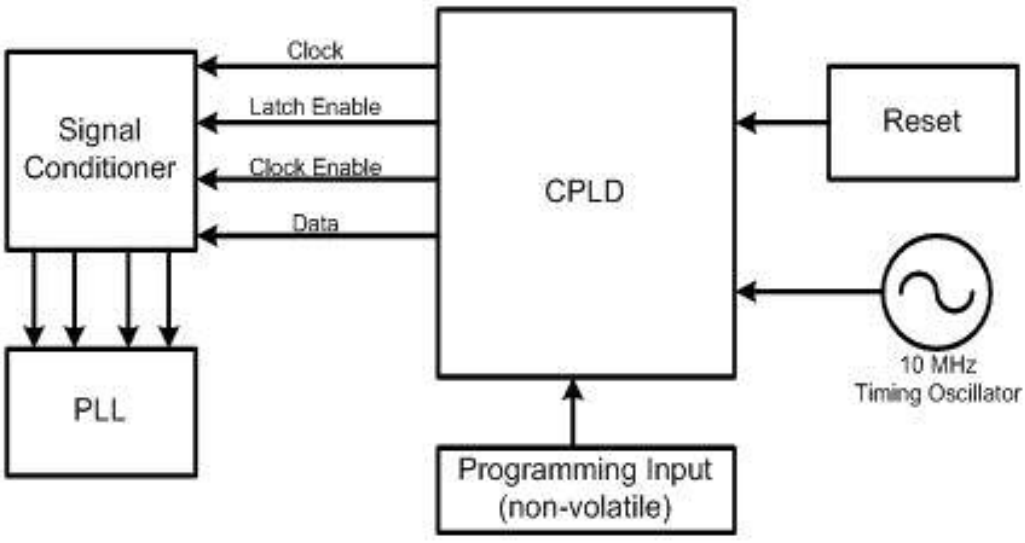

Figure 3.9: Simplified block diagram for the PLL programming circuitry.

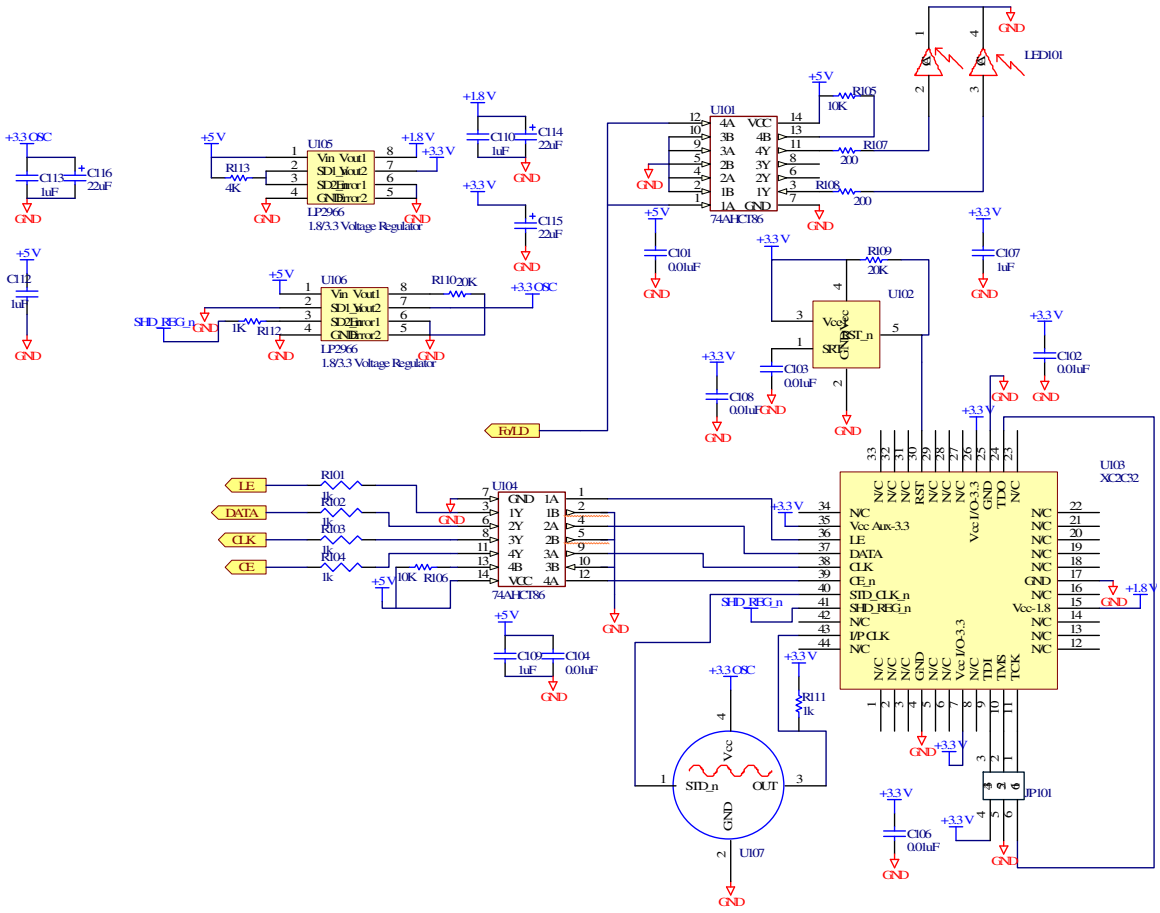

Figure 3.10: Detailed schematic of PLL programming circuitry.

including the CPLD and support circuitry, was designed previously by Parthasarathy for use in a 500 – 2000 MHz radar [26], but adapted for use for in this radar. Figure 3.9 shows a simplified block diagram for the PLL programming circuitry; Figure 3.10 shows a detailed schematic. When the radar is powered on, the CPLD outputs four streams of data to the LMX2326 chip. The clock signal provides the clock for PLL data, the clock enable pin notifies the PLL chip that programming is taking place, the latch enable line controls which of the three registers is being programmed and the data line contains the register programming information. The CPLD chip needs only to be programmed once. The logic within the CPLD is programmed from Xilinx ISE software using a serial interface cable.

3.2.3 Transmitter / Receiver

The transmitter and receiver sections consist of connectorized components purchased from several vendors. The original design intent was to use surface-mount components to construct the receiver, but changed to connectorized components due to the limited availability, cost and quality of drop-in components. The transmitter consists of two amplifiers, one coupler and a circulator. The receiver provides no gain, consisting of only the circulator, an attenuator and a mixer. The block diagram for the transmitter and receiver is pictured in Figure 3.11.

The main amplifier is a limiting amplifier with an input range of -10 – 0 dBm. The limiting amplifier provides a flat amplitude response over the entire operational bandwidth, within 1.5 dB; the output power is approximately 14 dBm regardless of input power. A limiting amplifier provides amplitude compression by saturating the

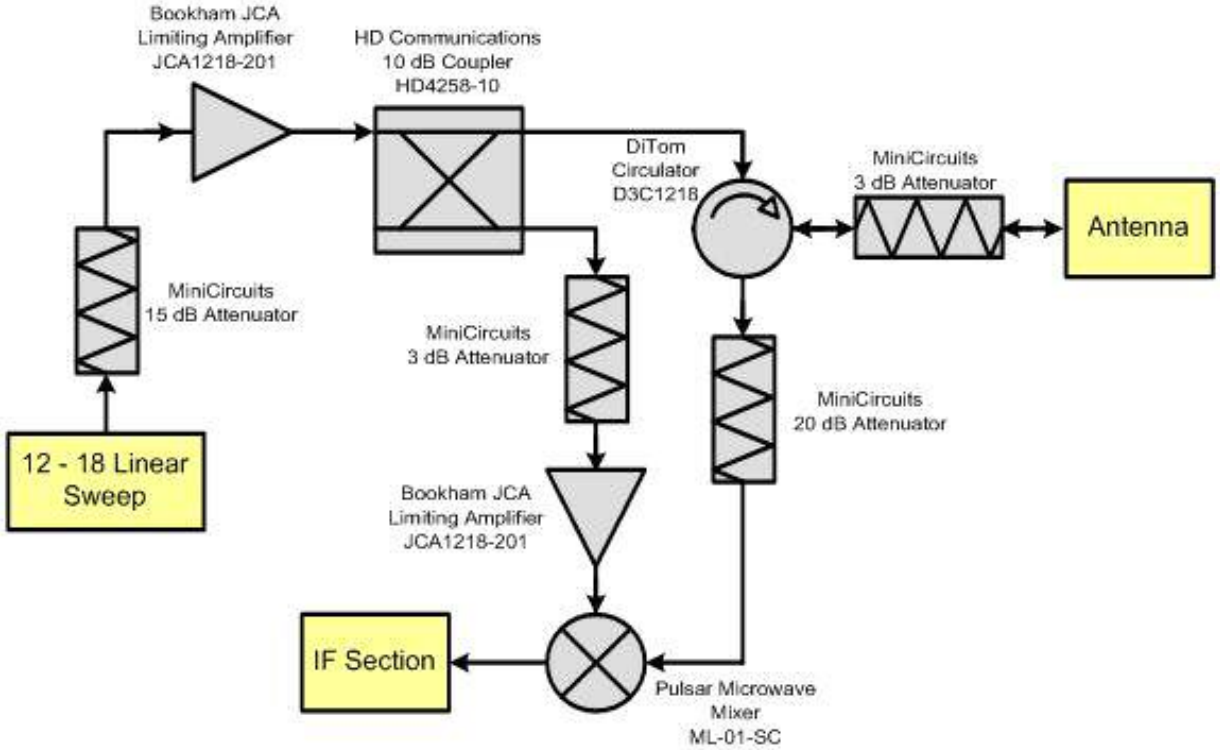

Figure 3.11: Transmitter and receiver detailed block diagram.

transistors, turning a sinusoidal input into a square wave output. Saturating the transistors ensures that any sinusoidal input will be amplified to the same level, clipping the maximums of the sinusoidal curves to the same amplitude. Figure 3.12 illustrates the limiting action of an amplitude compression amplifier in the time domain. Although the amplitude of the resulting signal is constant, it now more closely resembles a square wave. Since the resulting waveform is a square wave, odd-order harmonics associated with square waves will now populate the frequency spectrum. Figure 3.13 illustrates the effect of amplitude compression in the frequency domain. The original 5 kHz signal has only one peak in the frequency domain. The amplitude compressed signal has additional odd-order harmonics, with the most signal energy still centered at 5 kHz. The amplitude compression amplifier used in the radar creates the same harmonic distortion, but does not cause any serious design problems. The harmonics generated are far out of band,

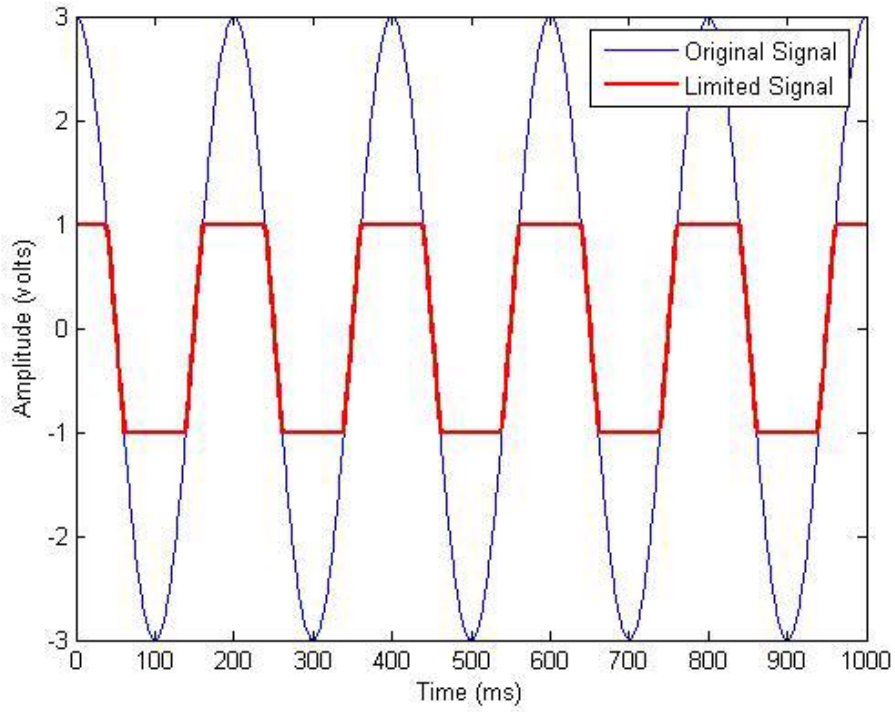

Figure 3.12: Amplitude compression in the time domain.

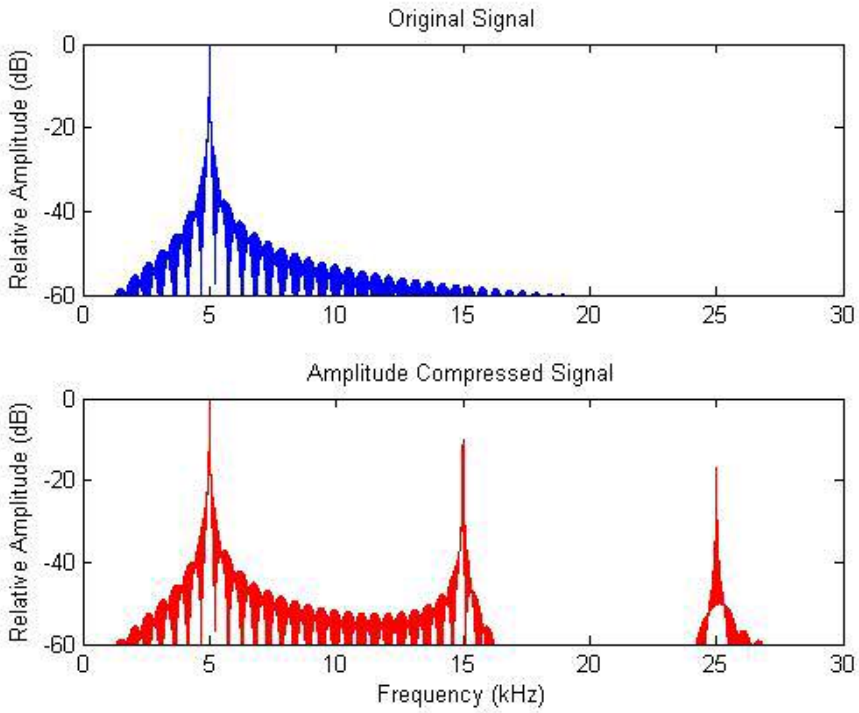

Figure 3.13: Amplitude compression in the frequency domain.

from 36 – 54 GHz. There are some second-order harmonics generated by the amplifier, but they are also out of band, 24 – 36 GHz, and suppressed by approximately 70 dB.

The amplifier output is coupled to another limiting amplifier to drive the mixer LO input. The through coupled output is fed into the circulator, which is used to direct signals in and out of the antenna. A circulator is a non-reciprocal device; energy directed into port one is directed out of port two, energy directed into port two is directed out of port three and energy directed into port three is directed out of port one. Port one is ideally completely isolated from input on port two, etc. A circulator typically is comprised of a 3-way junction and one or more ferrite materials. The ferrite materials are set up in such a way as to form a resonant cavity, providing easy power flow in one direction, and preventing power flow in the other direction [28]. The circulator used in this thesis work is manufactured by DiTom and provides about 23 dB of isolation

between ports with an insertion loss of about 0.5 dB. The circulator is used to isolate the receiver branch from power directed out to the antenna and to isolate the transmitter branch from power directed in from the antenna. The circulator facilitates the use of a single antenna for this radar.

A second limiting amplifier is used preceding the mixer LO input to drive the mixer at the specified LO input, which is 7 dBm. The mixer is manufactured by Pulsar Microwave and has an IF bandwidth from DC – 1 GHz, and RF / LO bandwidth of 6 – 18 GHz. The conversion loss is 6.5 dB. The mixer is used as a matched filter for the FMCW radar. Signals arriving from the antenna are time-delayed (by travel time to the target) and then mixed with the instantaneous transmit frequency to form a sum and difference frequency, which is used as the range measurement. A 20 dB attenuator is used preceding the RF mixer input to reduce harmonics in the beat frequency spectrum. In general, harmonics are greatly reduced when the RF input is 20 dB below the LO input. The IF output of the mixer is output to the IF section for further spectrum conditioning.

3.2.4 Antenna System

The antenna system consists of a wideband horn antenna, a parabolic reflector, an adjustable horn mount, and antenna pointing system. The antenna system utilizes a parabolic reflector in conjunction with the wideband feed horn to generate plane-wave illumination of the target area. Due to the narrow beam-width of the antenna, a precise antenna aim is needed. An automatic pointing system has been developed to keep the antenna pointing at nadir.

3.2.4.1 Offset-Fed Parabolic Reflector

A traditional horn antenna is used as the parabolic reflector feed. The horn antenna has a spherical wave front; the center of the wave front, or phase center, must be placed in the focal point of the parabolic reflector. The reflector used, Ku-Band / TXFCC-090KUG, is manufactured by Patriot Antenna Systems. The reflector is 90 cm in diameter (bore sight), with a focal length of 58.6 cm and offset angle of 21^{o}. The feed horn used is a double-ridged wave guide horn, model 3117 by ETS – Lindgren, with a bandwidth from 1 – 18 GHz and mid-band beamwidth of approximately 38^{o}. The gain of the parabolic reflector is approximately 40 dBi and the gain of the horn antenna is approximately 13 dBi. The configuration of the antenna system is pictured in Figure 2.10.

The primary design problems were to place the phase center of the feed horn at the focal point of the antenna and to minimize diffracting fields at the edge of the reflector dish.

The feed horn was properly positioned by placing the feed horn at the original focal length and parametrically tuning its position for best results. To obtain the field data for the purpose of evaluating the structure of the plane-wave, the antenna was pointed horizontally and connected to a network analyzer. A second horn antenna was connected to the second port of the network analyzer as a field probe. The probing horn antenna was mounted to an actuator for automatic measurement of the field. The test setup is pictured in Figure 3.14. The amplitude and phase data were taken from S21 measurements taken with an Agilent network analyzer in a room which was not padded with radiation absorbers to diminish reflections. In order to receive only the direct path

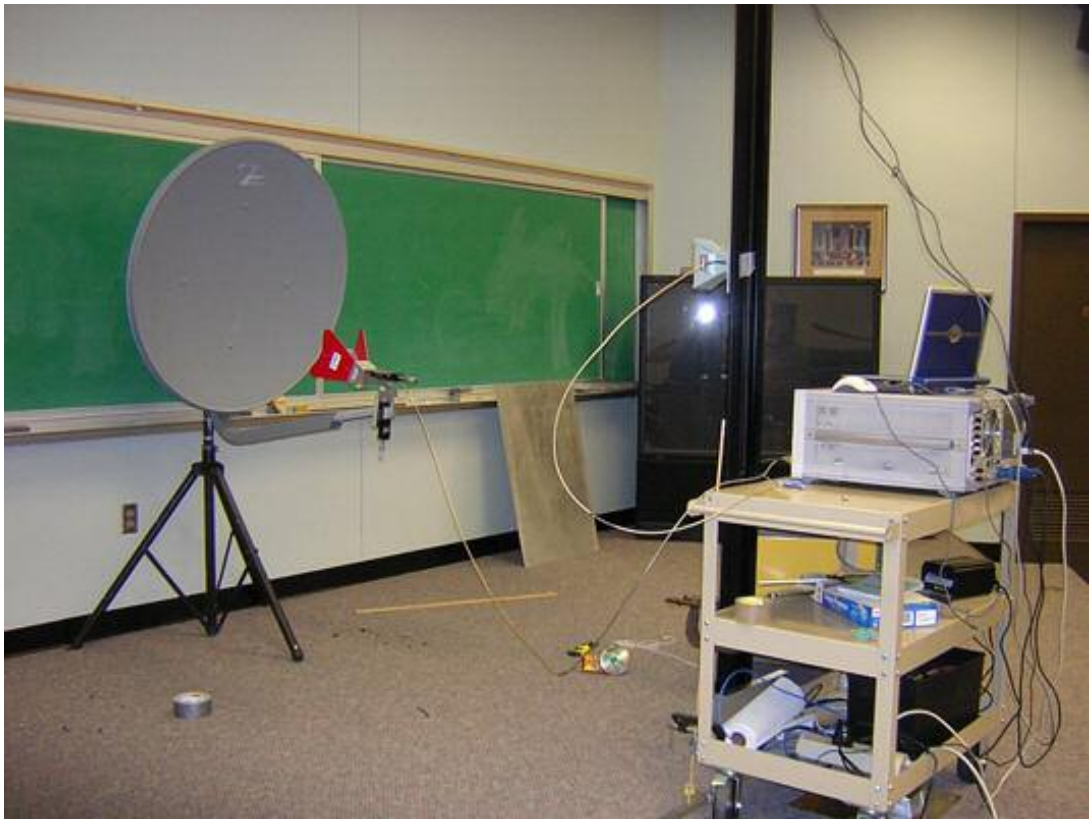

Figure 3.14: Antenna field measurement and adjustment setup.

from the parabolic dish antenna to the probe antenna, the network analyzer was calibrated and a time-domain filter was applied to S-parameter measurements. The parabolic reflector antenna was set in a stationary position while the field probe was placed on a computer-controlled actuator, which was mounted on a movable stand. The actuator movement was controlled and field data were recorded using software developed in Matlab.

The radiation field generated by the feed horn antenna is wider than the reflector dish diameter; therefore, there is field spillover and energy will be diffracted from the edges of the reflector. The diffracting fields from the parabolic dish edges were reduced by placing absorbing material on the parameter of the dish, Eccosorb ANW-72. The Eccosorb material provides 20 dB attenuation to normally incident energy.

3.2.4.2 Antenna Pointing System

The antenna generates plane-wave illumination. Due to the extremely narrow effective beamwidth of plane-wave illumination, any deviation of antenna aim off the target incurs significant loss in signal. Additionally, deviations in antenna aim off nadir will cause the coherent return to reflect out of the range of the antenna aperture. Because the radar will be mobile and traveling over uneven terrain, an antenna pointing system has been designed to sense the antenna tilt and compensate. The block diagram of the system is shown in Figure 3.15.

The most salient components of the antenna pointing and terrain compensation system are the field-programmable gate array (FPGA), the tiltmeter and actuator system. Figure 3.16 shows a functional diagram, which overviews the algorithm used to compensate for uneven terrain.

The tiltmeter used is the MD900-TS, manufactured by Applied Geomechanics. The tiltmeter has a sensitivity of 0.004^{o} and can measure tilt to $\pm 25^{o}$. The tiltmeter is

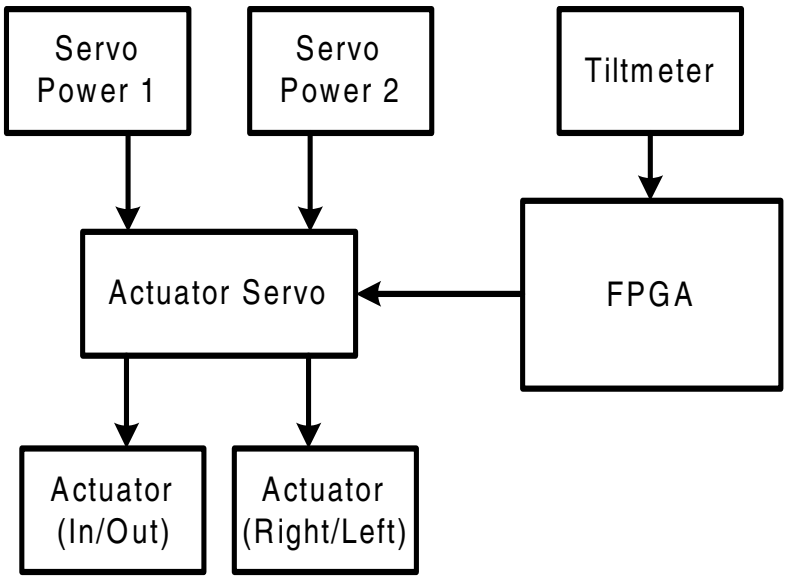

Figure 3.15: Block diagram of antenna aim and terrain compensation system.

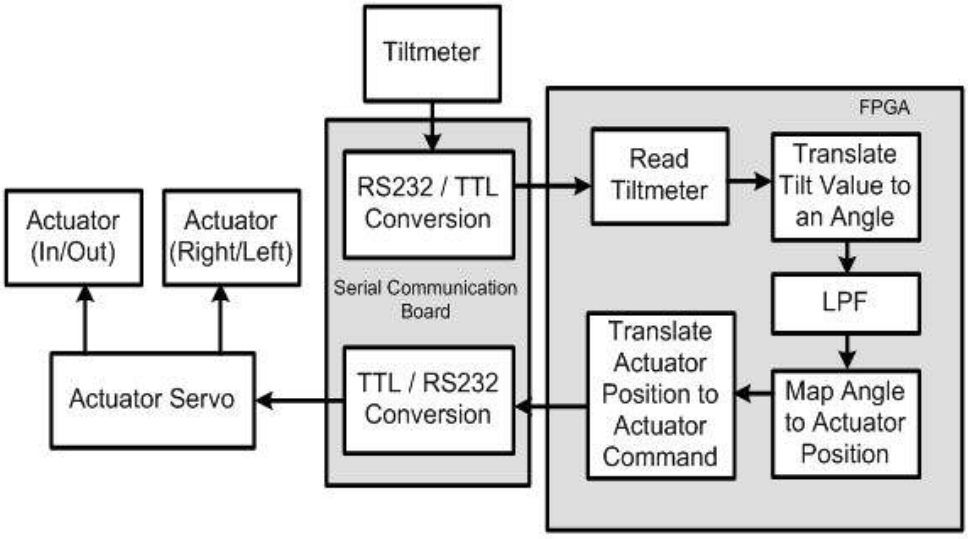

Figure 3.16: Functional diagram of terrain compensation system.

used to sense the tilt angle of the sled. The tiltmeter sends RS232 data to the FPGA at a baud rate of 19200. Notably, the tiltmeter uses a mercury bubble to sense inclination, which makes it very susceptible to acceleration.

The FPGA implements software, written in C, which performs all the necessary functions of interpreting the tilt data and providing a compensating movement command to the actuator servo. After receiving characters from the tiltmeter, the software translates the characters into a number representing the angle in incline. That angle is then stored (along with the previous two measurements) and used in a lowpass filter, to filter noise out of the angle measurement. As mentioned previously, the tiltmeter is susceptible to acceleration events. Acceleration causes the mercury bubble to slosh around, causing the tiltmeter to give erroneous readings. The filtered angle measurement is mapped to an actuator position, and the position is then translated into characters and sent to the actuator servo in RS232 format. The angle-to-actuator-position mapping was found by recording the antenna angular position over all actuator positions, then fitting a first-order polynomial to the data.

The lowpass filter implemented in the FPGA software follows expression [3.18], and is plotted in Figure 3.17. The lowpass filter is a third-order finite impulse response (FIR) filter.

$$H\left(e^{j\omega}\right)=\frac{b_1+b_2e^{-j\omega}+b_3e^{-j2\omega}}{a_1+a_2e^{-j\omega}+a_3e^{-j2\omega}} \qquad [3.18a]$$

$$a = \{28\ 56\ 28\} \qquad [3.18b]$$

$$b = \{10000\ -18739\ 8864\} \qquad [3.18c]$$

The large coefficient values are due to the inability of the FPGA to process floating point numbers; therefore, the filter coefficients are implemented as integers. The main concern in the filter design was the tradeoff between sufficient noise filtering delay. An *n*-order FIR filter will tap the signal *n* times and uses *n*-1 delays. The time delay between input and output is proportional to the number of delays the filter requires. Using more signal taps allows for more control over the cutoff frequency and affords a sharper roll- off, but causes the output to be delayed. Since the radar is mobile, a maximum travel velocity will be imposed based on the filter chosen. A third-order filter is used in the design,

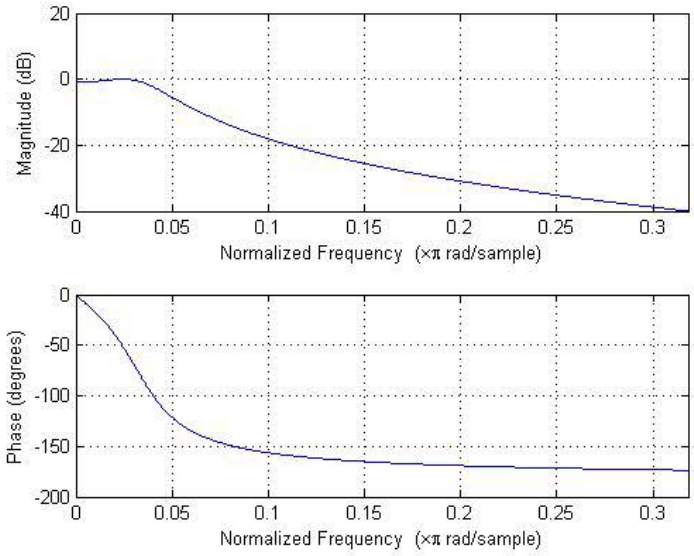

Figure 3.17: Tiltmeter angle measurement normalized lowpass filter response.

which will allow the filter to eliminate much of the noise caused by accelerations, and creates a delay of only about 500 ms.

3.2.5 Intermediate Frequency Section

The intermediate frequency (IF) section is used to filter unwanted signals from the beat frequency spectrum and amplify the beat spectrum to utilize the full dynamic range of the data acquisition system. The block diagram for the intermediate frequency section is shown in Figure 3.18.

After the signal is returned to the receiver, it is mixed with the instantaneous transmit signal to form a sum and difference frequency. The range information is contained in both parts of the signal, but it is practical to only process the difference frequency due to the bandwidth of the sum frequencies. The beat spectrum has a large amount of energy in the lower frequencies caused by reflections internal to the system, antenna-cable interface, diffracting fields around the parabolic dish and circulator feed-through. These unwanted effects are concentrated in the lower frequency band because they experience only small time delays between transmitter and mixer. This is convenient because they can be easily reduced or eliminated using a highpass filter. Using a highpass filter will greatly attenuate signals arriving before the surface return, and the cutoff frequency can be placed near the first layer return to reduce the surface return power without degrading nearby layer returns. After filtering low-frequency

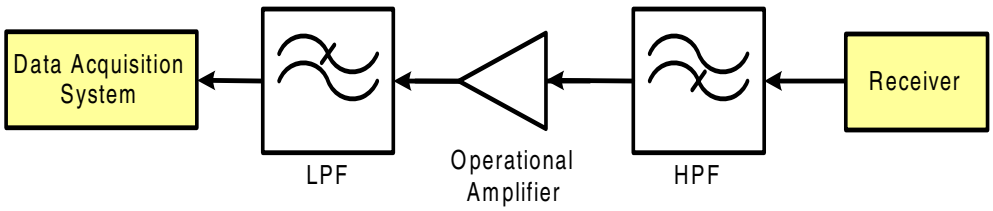

Figure 3.18: IF section block diagram.

signals from the beat spectrum, the signal is amplified to utilize the dynamic range of the data acquisition system. Finally, the signal is lowpass filtered near the Nyquist frequency to remove any signals that would cause aliasing during sampling.

To design the highpass filter, the valid beat frequency range must be known. The antenna is approximately 2 m from the surface; according to equation [2.3], the first layer will produce a beat frequency of 80 kHz. Since the next stage is providing more than enough amplification according to equation [3.13], the cutoff frequency of the highpass filter can be located slightly higher than 80 kHz. Additionally, it is expected that the pass band will shift slightly lower after implementation. The cutoff frequency is designed for 90 kHz. The filter is also implemented using Gaussian filter coefficients produced by Agilent Advanced Design System (ADS). The Gaussian filter design will significantly reduce the ringing, which can saturate the amplifier or DAQ. The highpass filter schematic is shown in Figure 3.19.

The amplifier stage will be deigned to boost the strongest return to utilize the full dynamic range of the DAQ. The transmitter output is about 10 dBm. Using the equation for reflection at dielectric interfaces, the surface reflection coefficient is estimated to be about 15 dB. After the receiver and conversion loss of the mixer, the top layer signal will be at approximately -40 dBm. A gain of 40 dB will be sufficient to maximize the dynamic range of the DAQ if the passband of the highpass filter is placed near the surface

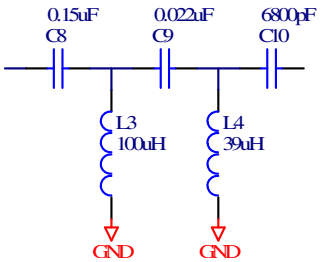

Figure 3.19: Schematic diagram of the IF section highpass filter.

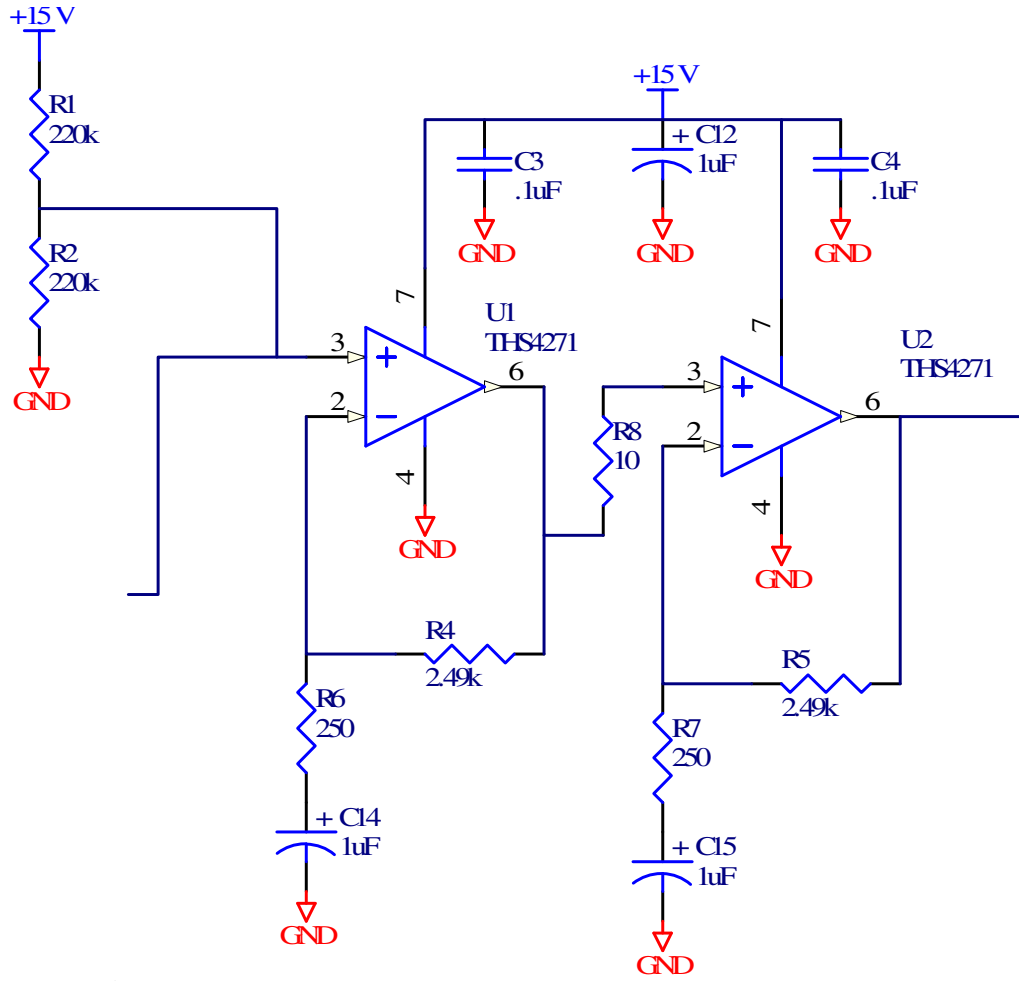

Figure 3.20: Schematic diagram of the IF section amplifier stage.

return. The schematic diagram of the intermediate frequency section amplifier is shown in Figure 3.20.

At the time of design, the sampling frequency of the data acquisition system was intended to be 50 MHz. Additionally, a contingency of using an oscilloscope for the DAQ was also under review. Under those design considerations, the amplifier stage was designed to have a bandwidth of 25 MHz (since the DAQ is not able to properly digitize signals near the Nyquist frequency) and to use operational amplifiers with a gain bandwidth of 2000 MHz. A gain of 40 dB translates into a gain of 100 (linear). Since the other sections of the radar require no negative supply, the amplifier stage is designed

to also run from a single positive voltage. The operational amplifier that meets the constraints is the THS4271, which is manufactured by Texas Instruments. If the operational amplifier is driven to produce the gain in one stage, the harmonic distortion is too great. The amplifier stage of the IF section will be constructed in two stages by cascading two of the operational amplifiers. A schematic diagram of the two-stage amplifier section is shown in Figure 3.20. Since the amplifier is operating in single supply mode, the input signal must be DC biased before amplification. Input and output capacitors block the DC bias applied to the positive terminal of the amplifier from leaking into the output of the IF section. The operational amplifier follows the gain equation of [3.17], with each stage providing an amplification of 20 dB.

The final stage of the IF section is the lowpass filter. The lowpass filter attenuates any frequencies beyond the range of the data acquisition system. The filter is implemented as a third-order Butterworth filter; the schematic diagram is shown in Figure 3.21. In accordance with the data acquisition system's sampling rate of 50 MHz, the filter has a cutoff frequency of 25 MHz. The filter values were chosen according to table values for a standard Butterworth filter.

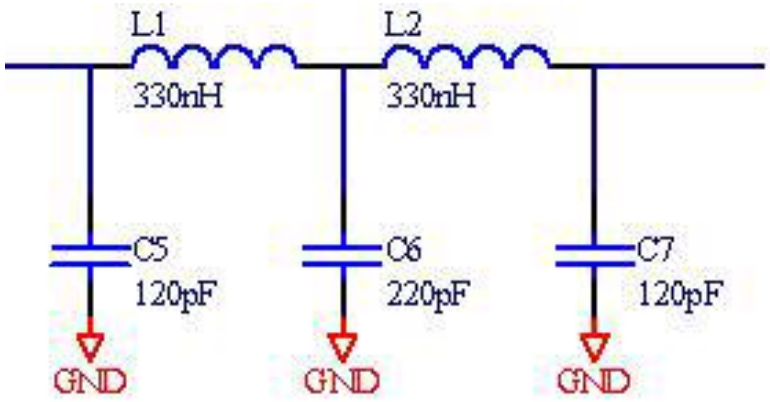

Figure 3.21: Schematic diagram of the IF section lowpass filter

3.2.6 Sled

The radar sled was designed at Honeywell in Kansas City, Missouri and manufactured by the University of Kansas physics machine shop. The sled provides a gimbal mount for the antenna, so that the antenna pointing system may keep the antenna pointed at nadir regardless of sled inclination. The sled was also designed with a wide base to help level out small surface features in the terrain. Because the radar sled must be shipped to remote polar locations, the sled was designed to be contained on a pallet sized for the U.S. Air Force C-130 cargo plane. Although the sled covers an area of approximately 36 ft^2 and stands to a height of over 10 ft, it breaks down into pieces which are less than 102 inches in length. The sled can be assembled entirely without tools, with the exception of one joint, facilitating user assembly wearing gloves.

CHAPTER 4

SIMULATION, IMPLEMENTATION AND LAB MEASUREMENTS

4.1 Introduction

Modern radar system design requires knowledge of electrical design techniques, computer aided design (CAD) software and simulation tools. Although good electrical design skills are essential when designing sophisticated electrical systems, the use of CAD software and simulation tools are also essential to reducing the cost of system development. Using computers to design and simulate a system, several iterations of a prototype construction may be avoided, and real-world noise problems and non-ideal effects may be accounted for before the first prototype is constructed.

Understanding of electrical issues alone does not insure practical system design. Mechanical considerations must be accounted for in system realization. Issues like temperature and component durability may be intuitive for the electrical designer, but other system practicalities are more easily overlooked. Reasonability of design, such as size constraints, manufacturability and portability are also crucial to system design.

4.2 Frequency Synthesizer

The frequency synthesizer uses a phase-locked loop to generate a high-frequency, highly-linear transmit sweep based on a reference chirp generated from the data acquisition system. The phase-locked loop was simulated and optimized in ADS. After final construction, subsystem-level testing was done in laboratories at the University of Kansas.

4.2.1 Simulation and Lab Measurements

The loop filter in the phase-locked loop has been optimized for the fastest lock time while providing sufficient frequency stability. The design tradeoff is between phase stability and the loop's ability to react quickly to changes in the reference frequency. If the loop filter is tightened, the phase stability will increase, but the loop bandwidth will be reduced. If the bandwidth is increased, or the loop filter loosened, the PLL will be able to track fast changes in the reference frequency, but at the cost of increased phase noise. Ideally, the frequency sweep should be completely linear, but since the resolution of the system is finite, linearity within the bandwidth of a single range bin will keep the effects of unwanted frequency modulation from corrupting the beat frequency spectrum.

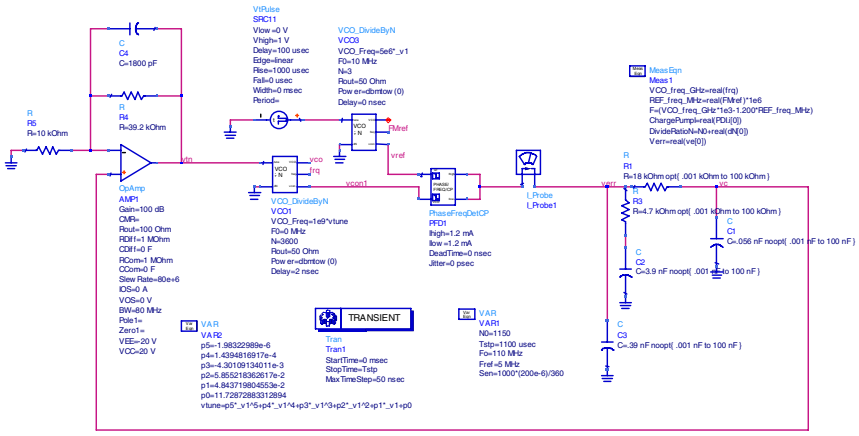

Figure 4.1: ADS simulation of phase-locked loop.

Increased phase non-linearity can and must be tolerated, but at the cost of signal-to-noise ratio in the beat frequency spectrum. The ADS simulation is shown in Figure 4.1.

The loop filter was designed as a third-order RC filter design, but the specific values for the resistors and capacitors were determined using optimization routines in ADS. The most significant simulation observations are the use of a phase detector model and a VCO model. Figures 4.2 and 4.3 show the ADS device models. The phase

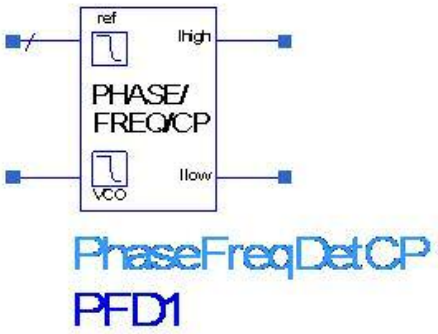

Figure 4.2: Phase detector model.

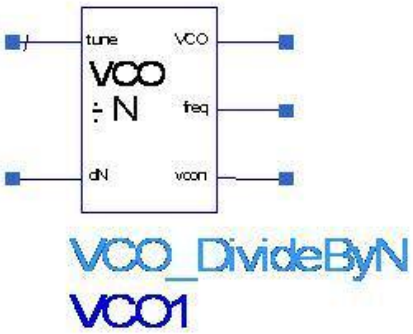

Figure 4.3: VCO model.

detector model (Figure 4.2) has an input for both the reference signal (ref) and the VCO signal (VCO), and it has differential current outputs (ihigh and ilow). The VCO model (Figure 4.3) has two inputs—a tuning voltage (tune) and a secondary divide ratio modulator (dN). The outputs are a sinusoid output (VCO), a frequency demodulated output (feq) and a divided VCO output (vcon).

The phase detector model simulates the tri-state design of the LMX2326 PLL chip because the differential current outputs sink and source current when there is a phase error; otherwise, the model neither sources or sinks current—behaving like a high-impedance device. The model allows adjustment of the sink / source currents that enables the close matching of the device performance. The model was set to provide 1.2 mA sink and source currents.

The VCO model was used for both the reference sweep and the main oscillator. The main oscillator model was set to divide the output by 3600 (accounting for the external divide-by-eight chip and the PLL internal divide-by-450 register) and the secondary divide ratio modulator was not used (grounded). The VCO model allows for definition of a non-linear tuning curve. The VCO output is controlled by an equation using the tune pin on the model. The voltage tuning curve was found by lab testing the Sivers IMA VCO and recording the input and output characteristics. The lab data was fit to a fifth-degree polynomial for use in the simulation. Figure 4.4 shows the measured tuning curve and the polynomial fit used in simulations. The divided output pin (vcon) was used as the phase detector input and the undivided output was unused. The frequency demodulated output was used to track the frequency of the VCO for

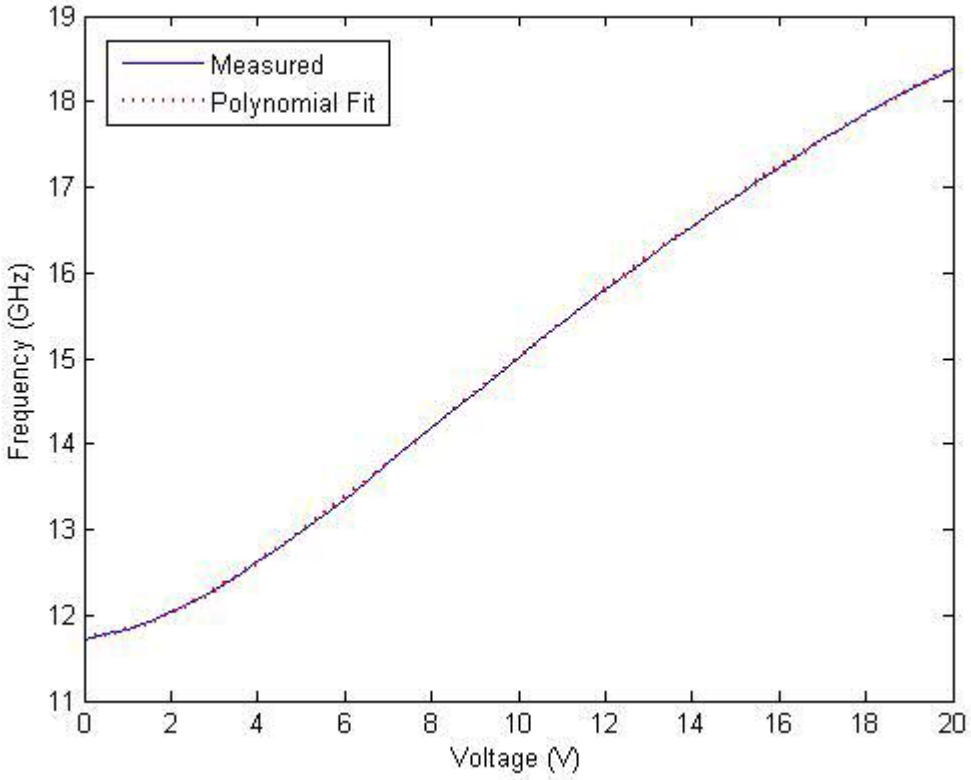

Figure 4.4: VCO tuning curve. The blue shows the tuning curve measured in the lab, and the red shows the polynomial curved used in simulations.

optimization purposes. The reference VCO was set to generate 10 – 15 MHz by setting the center frequency to 10 MHz, setting the tuning curve to be 5 MHz/V, and applying a tuning waveform to modulate the device to 15 MHz. The divide parameter was set to three (accounting for the PLL internal divide-by-3 register). The frequency demodulated output was used to track the frequency of the reference for optimization purposes.

The optimization goals were to minimize the frequency deviations during the lock time and to constrain the frequency deviation during the sweep to the lowest level possible. The optimization goals were evaluated using the frequency demodulated outputs of the VCO models and the following expressions:

$$f_{vco} - f_{ref} \leq f_{error} \qquad [4.1]$$

where f_{vco} is the VCO frequency, f_{ref} is the reference frequency and f_{error} is the allowable frequency deviation. It should be noted that these optimization goals were enforced

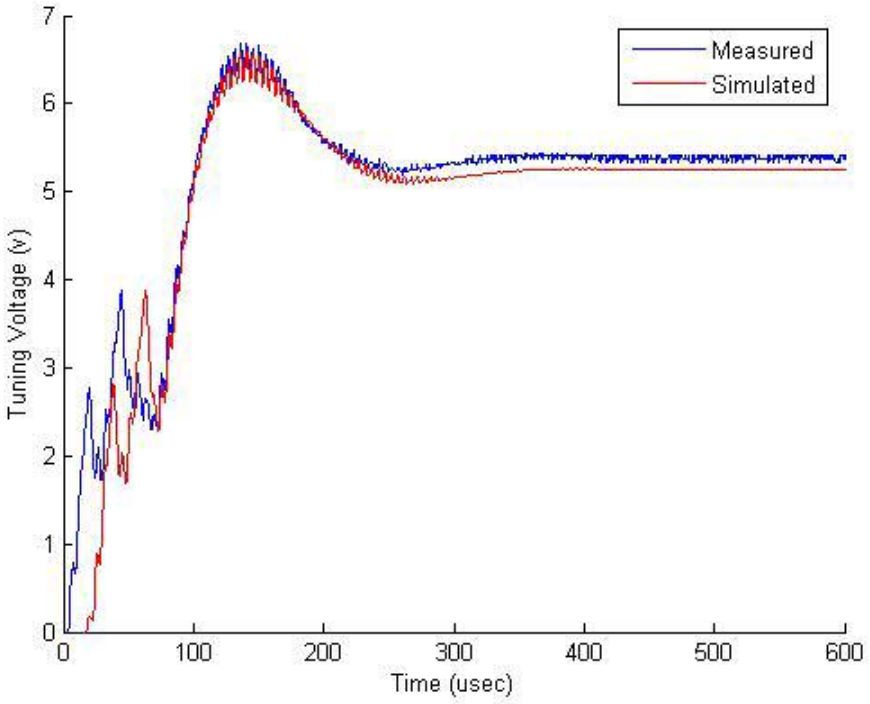

Figure 4.5: Single-frequency PLL lock time.

under design for a 2 kHz PRF and a sweep time of 250 μs. Figure 4.2 compares the simulated and measured single-frequency lock times of the PLL. Figure 4.2 illustrates the excellent match between the simulation and measured results.

4.2.2 Implementation

Implementation for the frequency synthesizer included design and layout of a circuit board, and an aluminum housing for the board. Due to the high frequencies on the circuit board, an extremely good ground must be established; signals must not travel great lengths to find ground. Careful attention was paid to line widths, distance to ground and line lengths for the several components operating in the gigahertz range.

One of the first considerations for board construction was the circuit board substrate needed. Typically, high-frequency circuit boards use material that reduces the loss factor of the substrate. Many high-frequency boards constructed at the University of Kansas have used Rogers 4350 material, with a dissipation factor of 0.0035. The necessity for using a high-frequency substrate was evaluated on the basis of how much high-frequency signal would need to be on the board. The biggest drawback for using FR4 material is the large loss associated with RF signals. After drafting a layout, it was determined that the longest line length would be 550 mil. A simulation using Agilent LineCalc showed that 18 GHz over that length would incur a loss of less than 1 dB. There are only two parts carrying frequencies in the gigahertz range; they are located as close to each other as possible in an effort to keep transmission lines short. The VCO outputs a signal at 18 GHz to the divider, which outputs a signal at 2.25 GHz. The divider was located on the edge of the board (because the feedback signal comes in from an external coupler) and the PLL chip was located directly next to the divider.

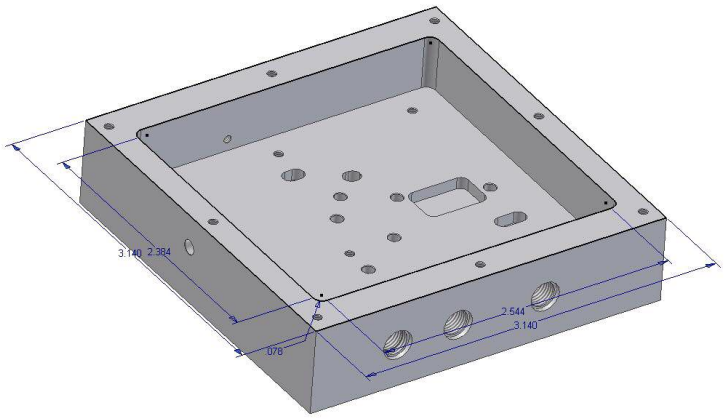

Figure 4.6: Aluminum housing design for PLL circuit board.

The path to ground is extremely important in high-frequency board design. A special aluminum housing was designed to house this board so that the ground plane on the bottom of the board will be in full contact with it. An AutoCAD drawing of the housing is shown in Figure 4.6. With the cover secured on top of the housing, it also protects other parts of the radar from the RF signals generated in the PLL housing.

The final dimensions of the frequency synthesizer (not including external coupler) are 3.140 x 3.140 inches. The final implementation is pictured in Figure 4.7.

Figure 4.7: Final implementation of frequency synthesizer.

4.3 Transmitter and Receiver

The radar in this thesis work is implemented as a monostatic radar. As such, the transmitter and receiver are closely related and must share one antenna. The transmitter and receiver were implemented using external, connectorized components; those components were individually tested in labs at the University of Kansas. Testing was performed on a network analyzer, and the results used in system simulations.

The characteristics of the transmitter and receiver components were recorded with ADS software and a network analyzer. The following tables and plots show the attributes of the limiting amplifier, coupler and circulator.

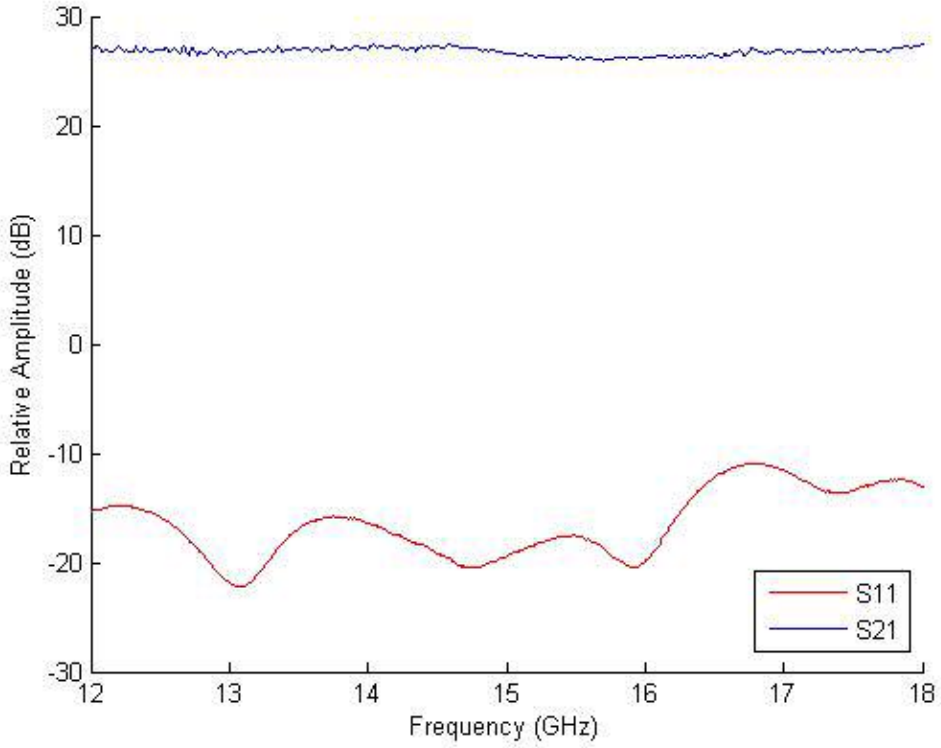

Figure 4.8: S-parameters for the limiting amplifier.

Gain	27 dB (max)
Gain Variation	1.4 dB (max)
Return Loss	10 dB (min)

Table 4.1: Limiting amplifier characteristics.

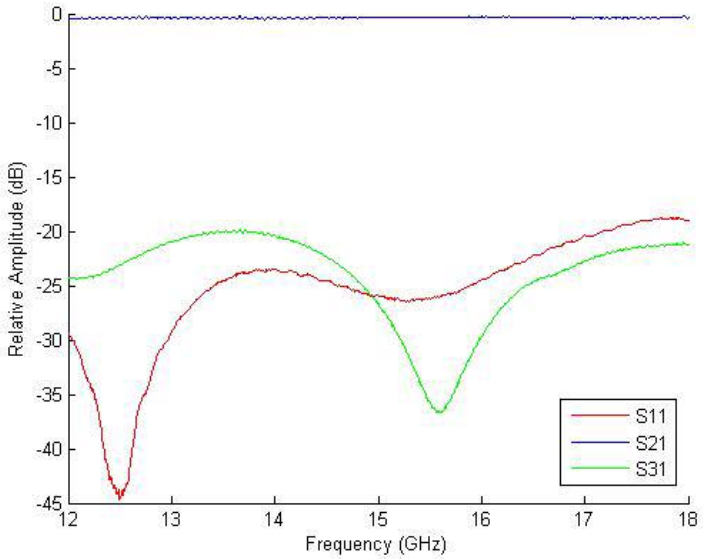

Figure 4.9: S-parameters for port one of the circulator.

Insertion Loss	0.5 dB (max)
Return Loss	19 dB (min)
Isolation	20 (min)

Table 4.2: Circulator characteristics (typical).

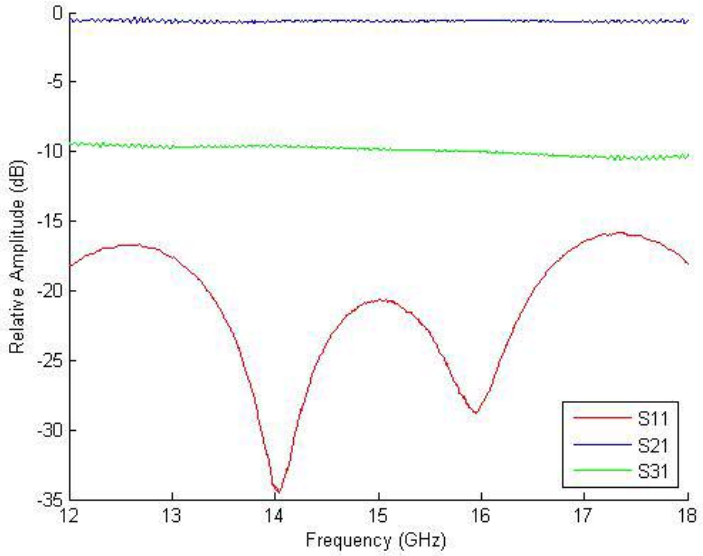

Figure 4.10: S-parameters for port one of the coupler.

Insertion Loss	0.7 dB (max)
Return Loss	16 dB (min)
Coupling	10 dB
Coupling Variation	±0.5 dB

Table 4.3: Coupler characteristics (typical).

4.4 Antenna System

The antenna system includes the wideband horn antenna, the parabolic reflector and the antenna pointing system. The antenna system radiation field was tested both in a stationary position in labs at the University of Kansas and dynamically in Greenland.

4.4.1 Implementation

The antenna system was implemented by removing the 14 GHz feed horn that came with the parabolic reflector and replacing it with the wideband feed horn. A different mount was constructed to hold the feed horn due to the size difference from the original horn and because the horn mount needs fine adjustment to be able to center the phase center in the focal point of the reflector dish. The feed horn on the mounting is pictured in Figure 4.11.

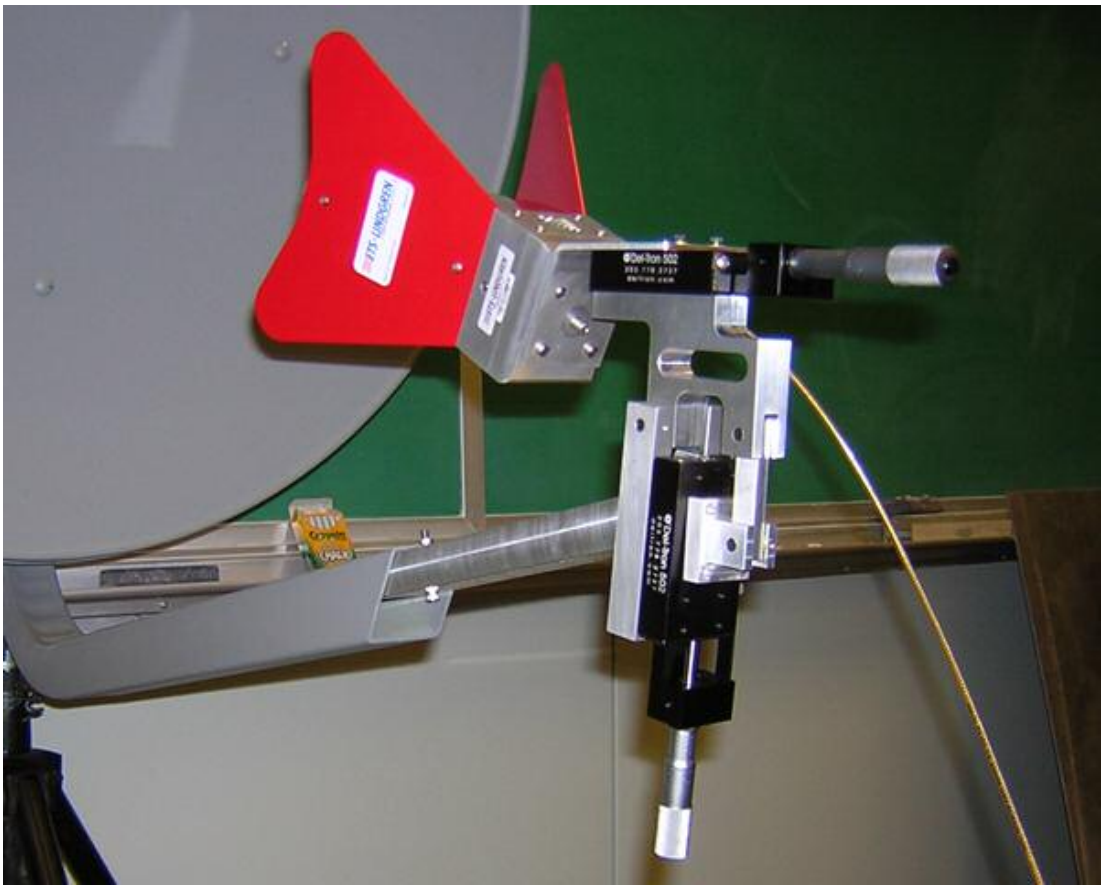

Figure 4.11: Antenna feed horn mount.

Figure 4.12: Parabolic reflector dish with Eccosorb on edges.

The feed horn mounting has been designed to accommodate the larger, wideband feed horn. The feed horn position can be adjusted using the ball slide positioning mechanism. The ball slide allows adjustment to move the horn towards or away from the reflector dish, or to change the pointing angle up or down. Adjustments can be made on the order of 1 mil. The mount was designed and fabricated by the Department of Physics machine shop at the University of Kansas.

Eccosorb was placed on the parameter of the parabolic reflector to minimize the effects of fringing fields. The Eccosorb was held by Velcro and can be seen in Figure 4.12.

The antenna pointing system consists of a tilt sensor, motion compensation actuators, a movement control system and a gimbal mount for the antenna. This system can be seen in Figure 4.13. The tilt sensor was mounted on the sled to implement a control system with no feedback mechanism. The tiltmeter is too sensitive to acceleration to be mounted on the reflector dish; mounting on the dish and using positive feedback to control the antenna aim would produce oscillation. The actuator servo and power, along with the movement control system, are located in the rack. The motion

Figure 4.13: Antenna and antenna pointing system.

control system is implemented using an FPGA. The FPGA chip is mounted on an evaluation board that has external sockets for interfacing other devices. A circuit board containing an RS232 interface system was designed and constructed to attach to the FPGA evaluation board using the external sockets. The motion control system is pictured in Figure 4.14.

Figure 4.14: Motion control system.

4.4.2 Lab Measurements

Lab measurements were taken on the stationary antenna system, and the field was tested again during field experimentation.

In order to ensure the antenna is providing plane-wave illumination, the amplitude and phase of the field was measured at a distance of 2 m, which is the same distance that the radar will be above the surface of the ice sheet. The test setup is pictured in Figure 3.13. The field was sampled from 10 – 20 GHz, and data were taken with 10 cm horizontal resolution and 2 cm vertical resolution using an automated measurement system that incorporated an actuator-mounted field probe antenna. Figure 4.15 shows the field amplitude and Figure 4.16 shows the field phase. Any disruption from the equal

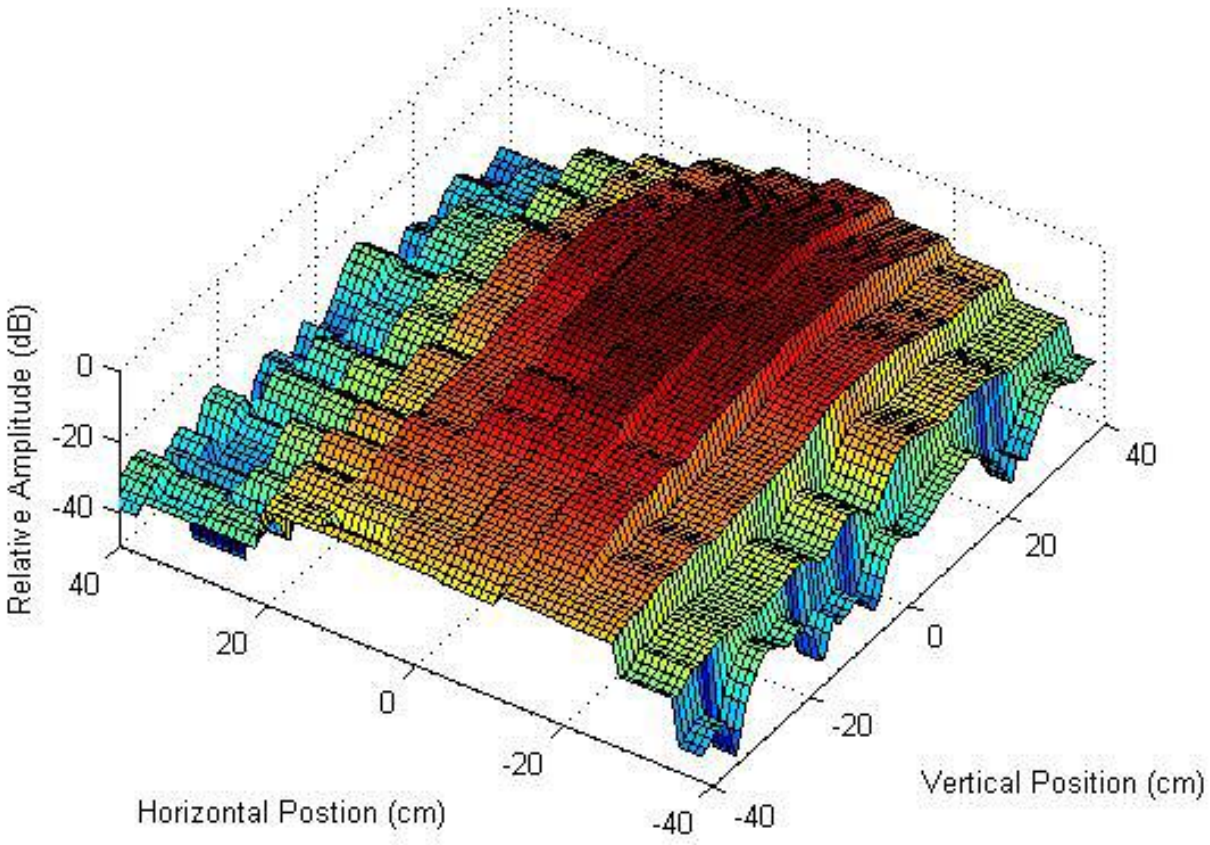

Figure 4.15: Amplitude characteristics of plane-wave field at 15 GHz.

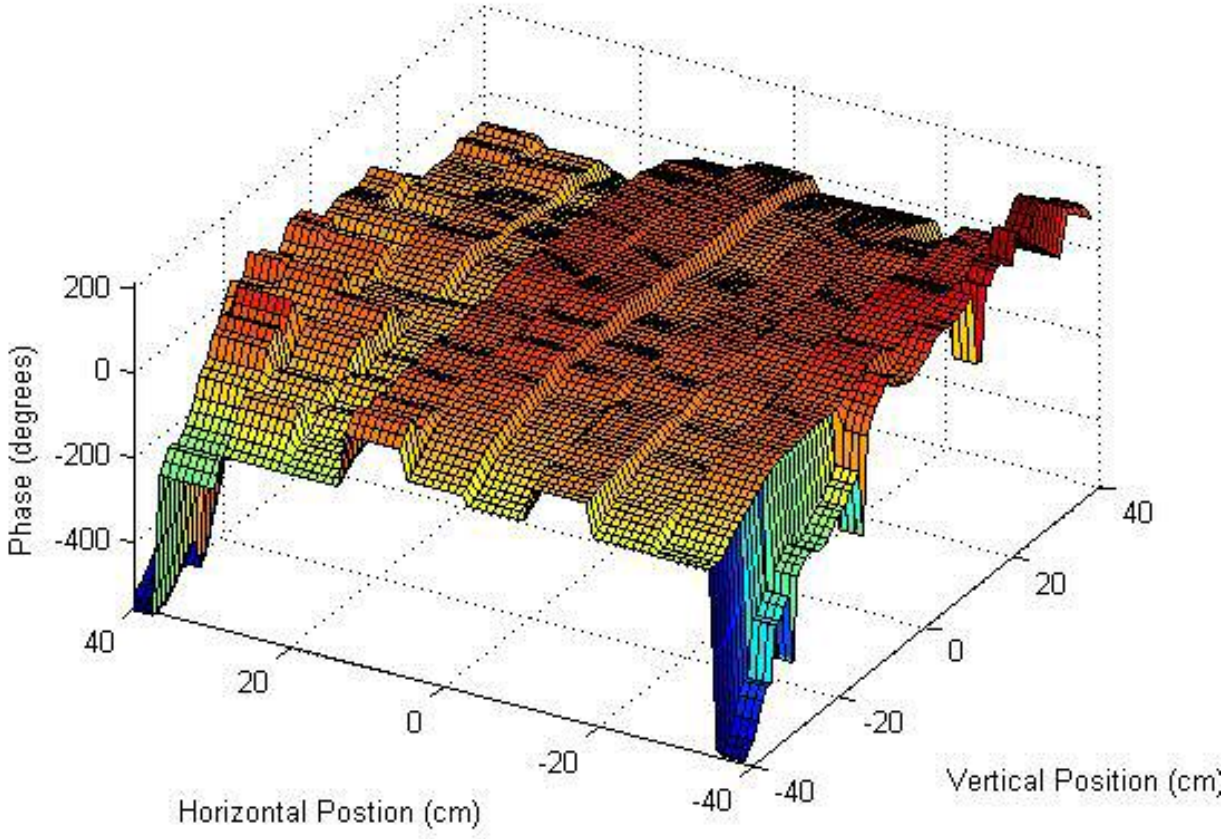

Figure 4.16: Phase characteristics of plane-wave field at 15 GHz.

phase front will degrade the radar resolution by introducing incoherent scattering, but will also reduce the power returned to the focal point of the parabolic reflector. The power returned to the focal point of the reflector can be estimated using the following expression:

$$\iint_S e^{j2\pi\Delta\phi} \qquad [4.1]$$

where S is the surface of the wave front and $\Delta\varphi$ is the phase deviation from the equal-phase wave front. Equation [4.1] shows that the power will add at the focal point of the reflector, and any phase deviations will cause destructive interference and reduce the total power at the focal point. Using Riemann sums to estimate the power returned to the focal

point, the plane-wave shown in Figure 4.16 will suffer a 35.6% power loss due to phase deviation errors. It should be noted, though, that the plot shown in Figure 4.16 may contain significant errors. The field was measured using an actuator to control probe antenna movements in the vertical position in 2 cm steps, but was moved manually in the horizontal direction. A small change in distance to the antenna will significantly change the phase measurement. For example, a distance deviation of only 0.5 cm at the center frequency of 15 GHz will produce a relative phase shift of 72 ^{o}. Additionally, energy on the edge of the aperture will not likely return to the focal point of the reflector. A better estimation of phase performance can be evaluated using a single vertical field slice. One such measurement is plotted in Figure 4.17. The phase degradation on the left side of the plot is most likely due to the interference caused by the feed arm, and it is not likely that much of that signal will return to the focal point. The wave front shown in Figure 4.17

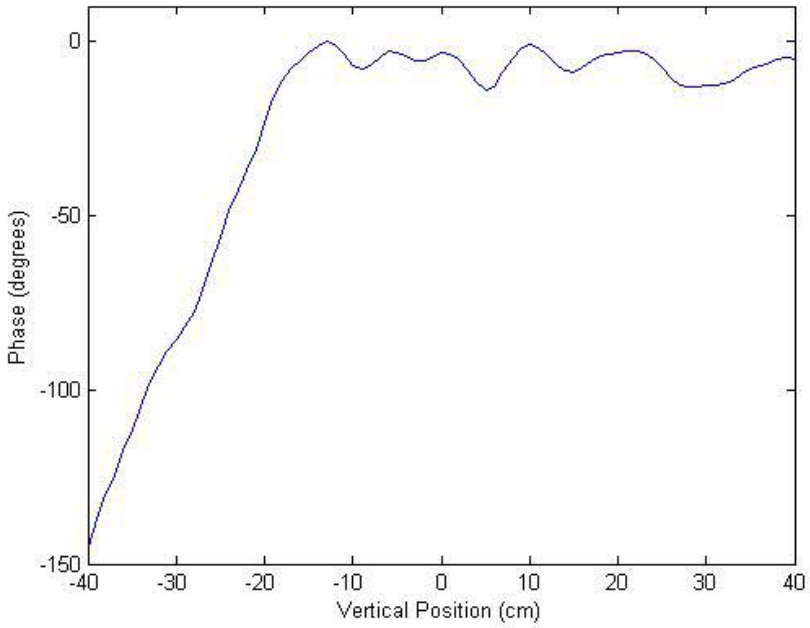

Figure 4.17: Vertical slice of antenna phase characteristics at 15 GHz. Slice taken from center of aperture.

will suffer a power loss of only 18.8% due to phase errors. Using the field returned from the top 60 cm of the aperture shows that phase inconsistencies will cause a loss of less than 0.25%.

Ideal plane-wave illumination will not incur any spreading losses. Spreading losses for the antenna system were found by tracking the power returned from a plate target at increasing distances. A metal plate was placed at nadir and moved away in steps of 50 cm. Figure 4.18 shows the power returned from targets at increasing distances compared with expected returns from a target using an antenna with a spherically spreading wave front. Although perfect plane-wave illumination is not shown in the plot, the plot shows that spherical spreading is not following the pattern of a traditional horn

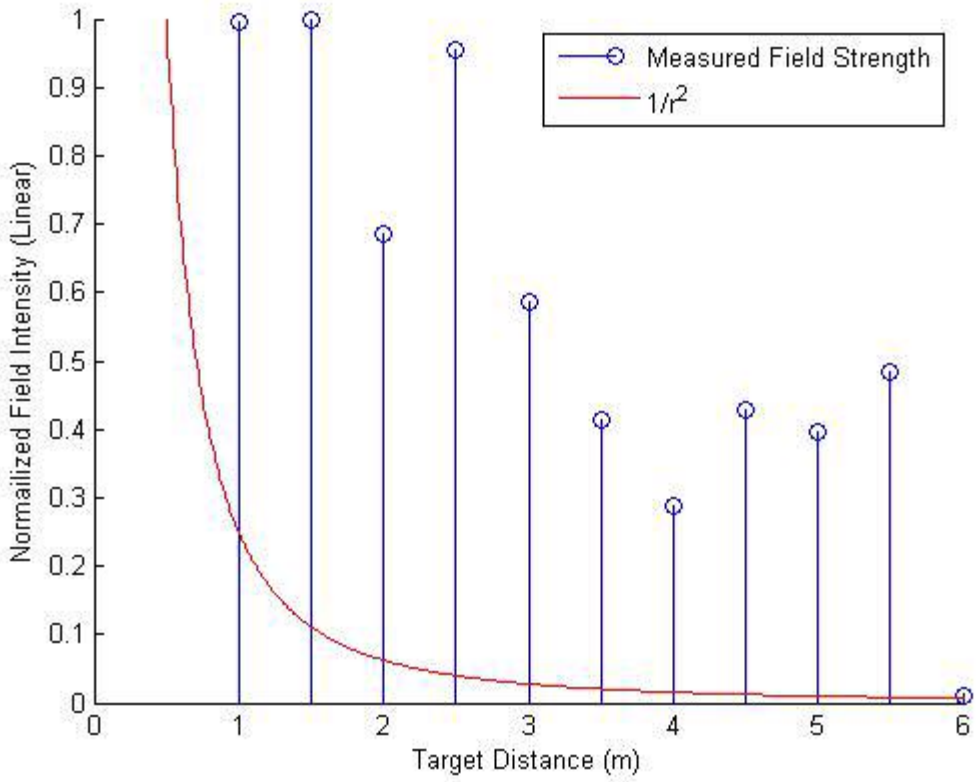

Figure 4.18: Return power from targets. The blue shows measured returns from targets using the parabolic reflector, while the red shows theoretical expected power from a traditional horn antenna

antenna. It should be noted that the metal plate target test is prone to errors from target orientation. Since the metal plate was positioned manually, it is likely that errors arose from the metal plate not being parallel with the plane wave front. In that case, a portion of the specular power would not have been returned to the antenna. In any case, it is clear that the illumination created from the parabolic reflector does not experience typical spreading losses.

The plane-wave illumination has an effective beamwidth where specular power is returned to the parabolic reflector. The beamwidth measurement was taken using a metal plate. Figure 4.19 shows the antenna beamwidth for angles towards and away from the sled, while Figure 4.20 shows the beamwidth for angles right and left of the sled. The beamwidth was measured to be approximately 1.2 ^{o} for angles towards and away from the sled and 1.4 ^{o} for angles right and left of the sled.

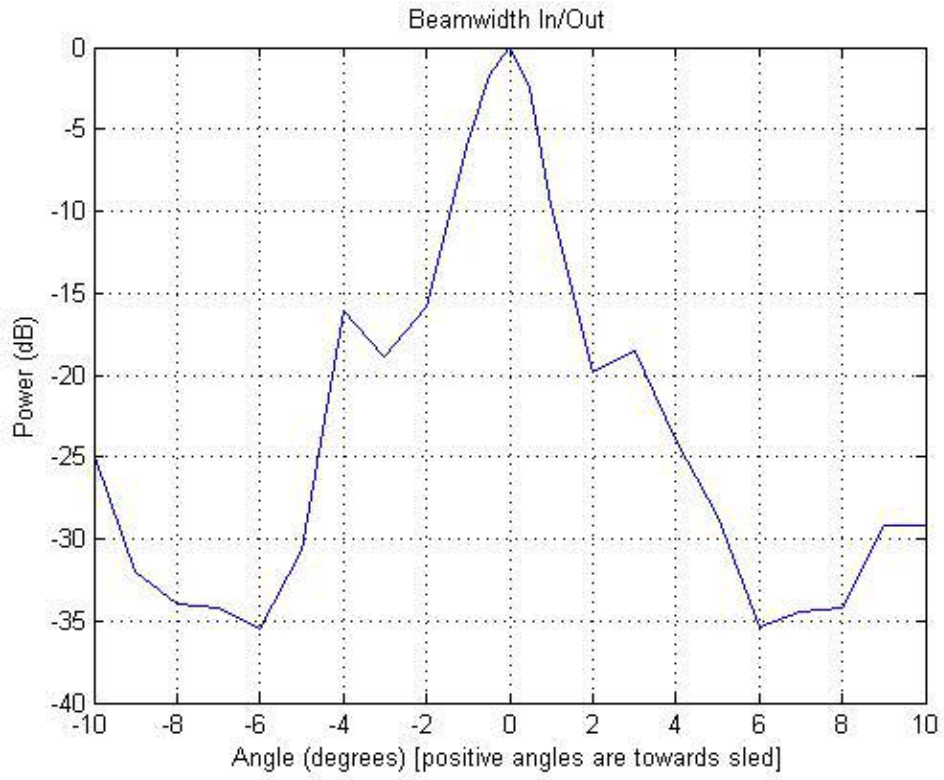

Figure 4:19: Antenna pattern (towards and away from sled).

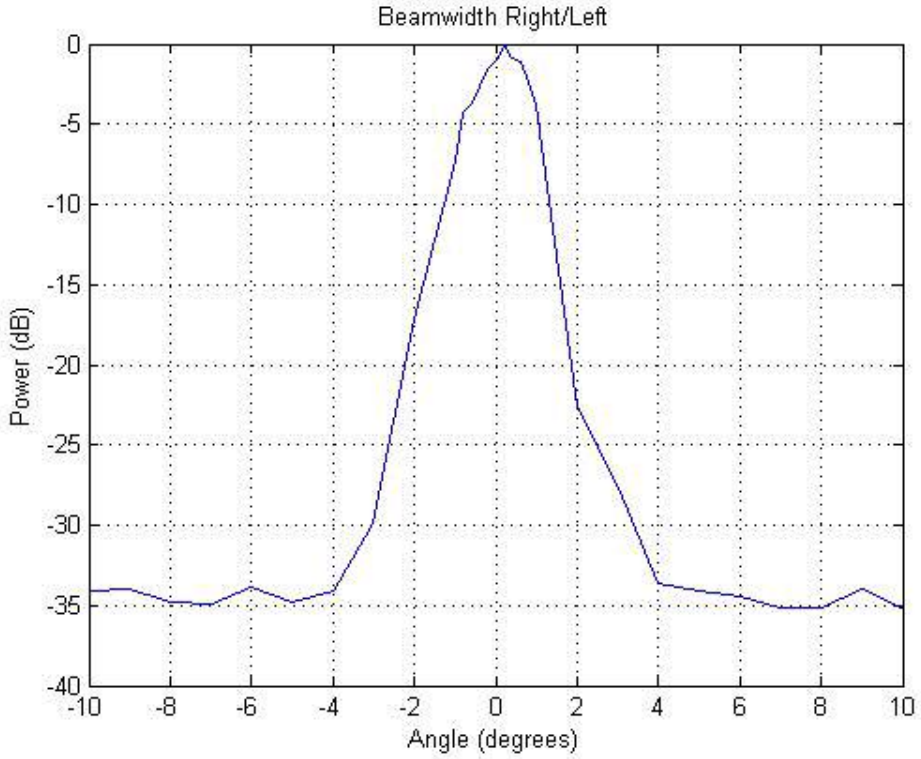

Figure 4.20: Antenna pattern (right and left of sled).

4.5 Intermediate Frequency Amplifier

The intermediate frequency amplifier is used to boost the beat frequency signal to utilize the dynamic range of the data acquisition system, and it is used to filter out beat frequencies that are not of interest. The design was simulated using ADS software and the circuit board was designed in Protel. Measurements were taken in labs at the University of Kansas to insure performance.

4.5.1: Simulation

Simulations were performed in Agilent Advanced Design System software. The simulation can be seen in Figure 4.21. In order to more closely simulate the non-ideal effects of the inductors, s-parameter models were inserted into the simulation to include the parasitic impedances of the components. The SPICE model of the operational

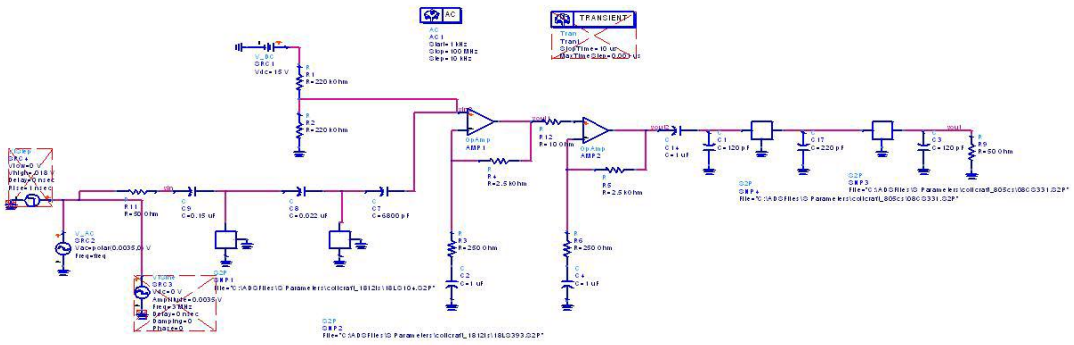

Figure 4.21: Simulation of IF section in ADS.

amplifier used was unavailable at the time of simulation, so a model which included non-ideal effects was used to simulate the THS4271 operation amplifier. The capacitors were modeled with an ideal model since no s-parameter models were available for the capacitors. The simulation results can be seen in Figure 4.22. The simulation shows that the intermediate frequency section gives a maximum gain of 42.3 dB over a bandwidth of 90 kHz to 30 MHz.

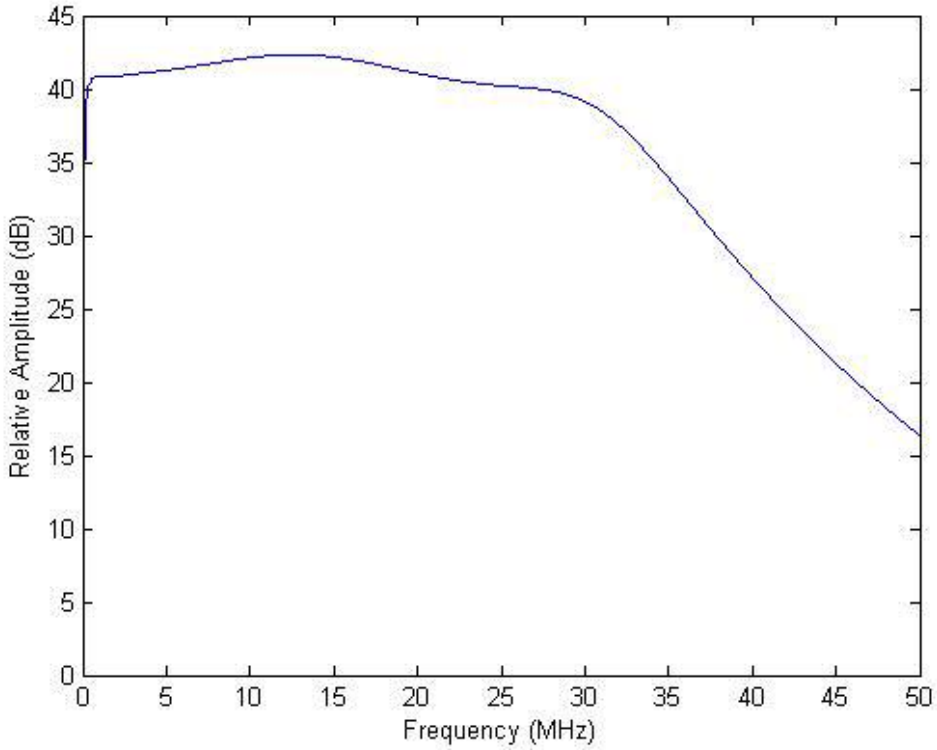

Figure 4.22: Simulation results for IF section.

4.5.2 Implementation

The intermediate frequency section was implemented on a 4-layer board using FR4 substrate. The highest frequency of interest on the circuit board is less than 25 MHz; there are no significant losses over that frequency range, so the FR4 substrate is sufficient for construction. The circuit board layout of the intermediate frequency section is shown in Figure 4.23. The feature of the layout most worth mentioning is layout considerations taken for the high-speed operational amplifiers. There are layout recommendations given in the data sheet. Most high-speed operational amplifiers require that there be no copper poured under the amplifier package. The green area under the amplifiers is a gerber file marker for an area where no copper is to be used. The circuit board has been mounted into a 1.25 x 2.5 x 0.75 inch RF enclosure purchased from Compac.

4.5.3 Lab Measurements

Measurements for the performance of the IF section were taken in labs at the University of Kansas. Due to the schedule of field experimentation, detailed plots of

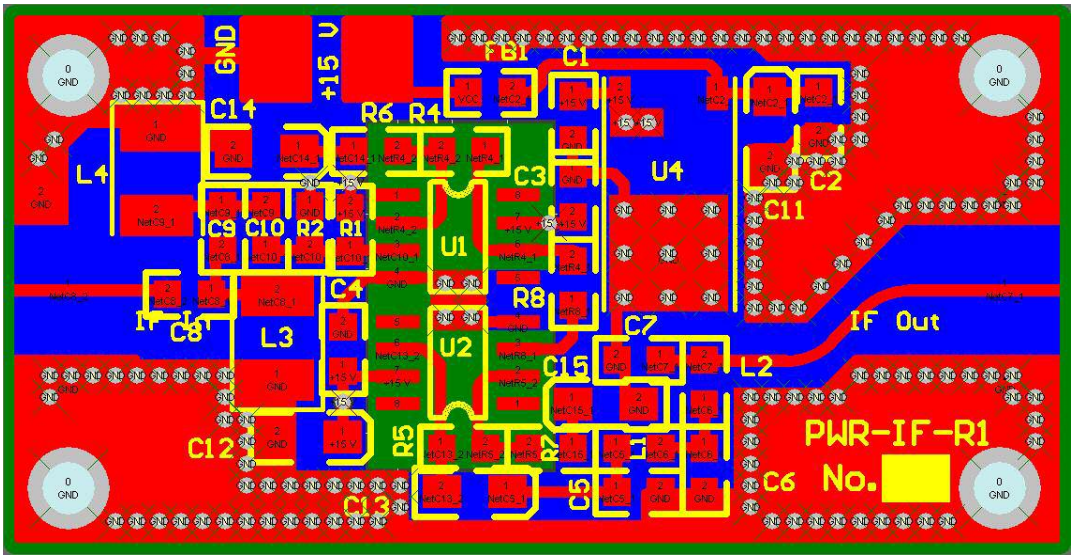

Figure 4.23: Circuit board layout for IF section.

the IF section gain and bandwidth are unavailable. Testing showed a gain of approximately 40 dB through the bandwidth of interest. Because the sampling rate of the data acquisition system was reduced to 5 MHz after design, an external lowpass filter with a cutoff frequency of 2.1 MHz from Mini-Circuits was used after the IF section to eliminate signals that would cause aliasing.

4.6 Integrated System

After subsystem design, the system was integrated for final testing and experimentation. The transmitter and receiver section was simulated in ADS to show expected beat frequency spectrum. System-wide measurements were taken in labs at the University of Kansas to test overall system performance with and without the antenna, and a simulation was constructed in Matlab to show expected returns from layers with differing densities.

4.6.1 ADS Target Simulation

The s-parameters from the receiver components were obtained using a network analyzer and loaded into ADS to simulate transmitter and receiver performance. The simulation is shown in Figure 4.24. Targets are simulated using delay components. The delay component is able to have a specified impedance as well as a specified delay time. In order to simulate a reflection from a distant layer, the delay component is specified to have a characteristic impedance equal to 50 Ω and a delay equal to the time it would take for light to travel the distance to the surface. For the sake of comparison, the simulation was conducted to match testing performed in the lab. The simulated target is a delay line, six feet (1.83 m) in length. The simulation uses a characteristics impedance of 50 Ω and

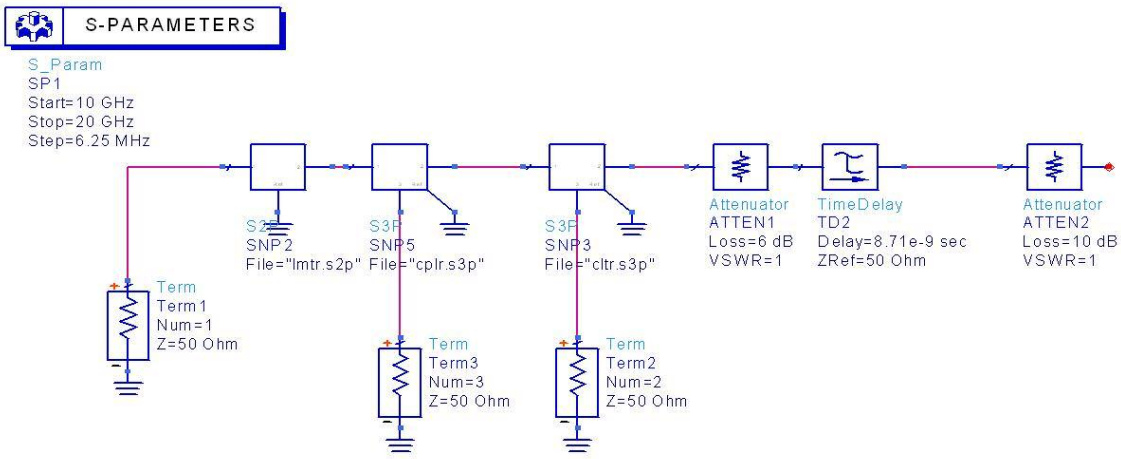

Figure 4.24: Advanced Design System target simulation.

a delay time of 8.71 ns, which simulates a target at 1.83 m and accounts for the speed of light inside the cable, which is 0.7*c*. The simulation results are pictured in Figure 4.25.

The spectrum shows that the beat frequency is centered at 110 kHz. The spectrum also shows that there is a significant amount of power from port one of the circulator that bleeds through to port three. The isolation for the port is 20 dB, and the simulation shows that it is within that specification. The signal power from port one seen

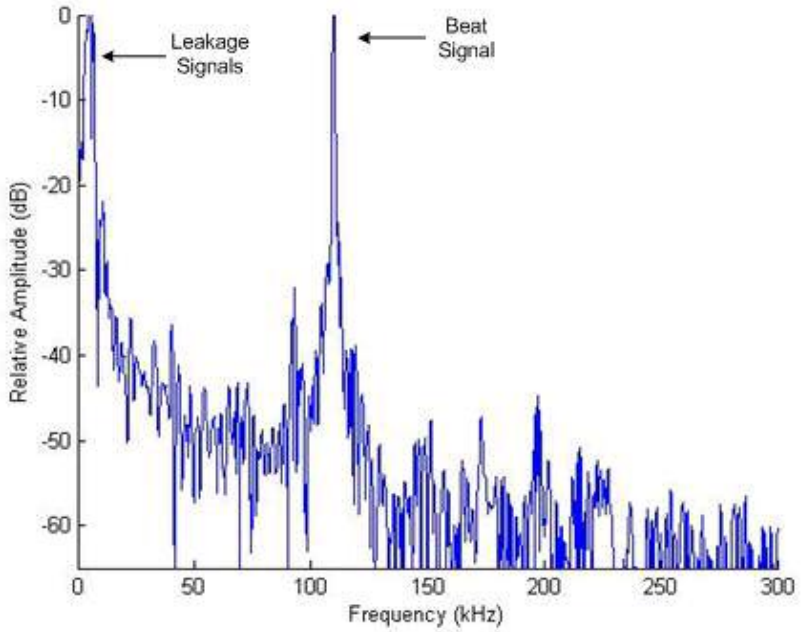

Figure 4.25: ADS target simulation results.

on port three experiences a very short delay time, thus will produce a beat frequency which will fall in the stop band of the IF section highpass filter. The signal power seen at 93 kHz and 197 kHz are side lobes created from amplitude and phase modulation—the highest peak at 93 kHz being associated with the circulator feed-through signal. Some of the effects of amplitude modulation can be reduced by deconvolving system effects from the return. The phase modulation is introduced by the limiting amplifier. The phase response of the limiting amplifier is shown in Figure 4.26. Side lobes from phase modulation are not necessarily symmetrical.

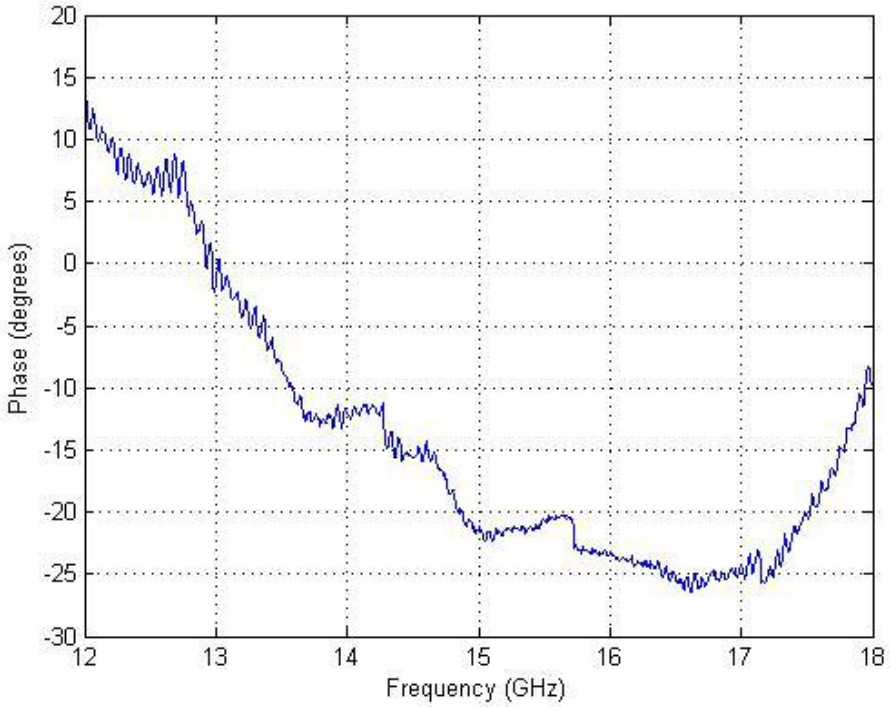

Figure 4.26: Phase response of limiting amplifier.

4.6.2 Radar System Implementation

The radar system is designed to be mobile, so final system integration and implementation included mounting the radar system to the sled. The final implementation of the radar can be seen in Figure 4.27. All components of the radar

Figure 4.27: Final radar system implementation.

were contained in a 4 x 6 x 2.5 inch RF enclosure manufactured by Compac. The radar box is mounted on the feed arm of the parabolic reflector to facilitate the use of a short cable to the antenna. The sled control system (excluding the actuators and tilt sensor) are located inside the rack, housed inside the main control box. Three cables run back to the data acquisition system, also mounted in the rack; one cable carries the reference chirp signal, another carries the IF signal back to the DAQ and another provides the DC power to the radar. The DAQ is also connected to a GPS receiver that sends location data, which is correlated with the recorded measurements. The main control box has three additional cables: one linking the tilt sensor with the motion control system and the other two to link the two actuators to the servo. The system is able to be maintained with one small generator.

The sled has a triangular base fitted with four 2 x 4 inch studs to support the generator and the equipment rack. The sled also has a chair installed in front of the equipment rack, where an operator can sit and track system performance while taking mobile measurements.

4.6.3 Radar System Lab Measurements

The radar system was tested in labs at the University of Kansas without the antenna system using delay lines as well as using a metal plate target.

A coaxial cable, six feet in length, was used to simulate a target. The coaxial cable was terminated with a 10 dB attenuator and a short. The signal velocity in the cable is about 70% the speed of light. Figure 4.28 shows the beat frequency spectrum from the coaxial cable simulated target compared to the simulated results. According to equation [2.3], there should be a strong peak at about 105 kHz; the plot shows a strong peak at 110 kHz. The amplitude is somewhat lower due to the loss incurred by the cable. The cable losses present in the lab experiment are not accounted for in the simulation. The beat frequency is reasonable considering the added cable length of the attenuators and the relatively unmeasured cable length. A second strong peak is seen at 216 kHz; this is a multiple of the main return, having reflected from the circulator and traveled back down

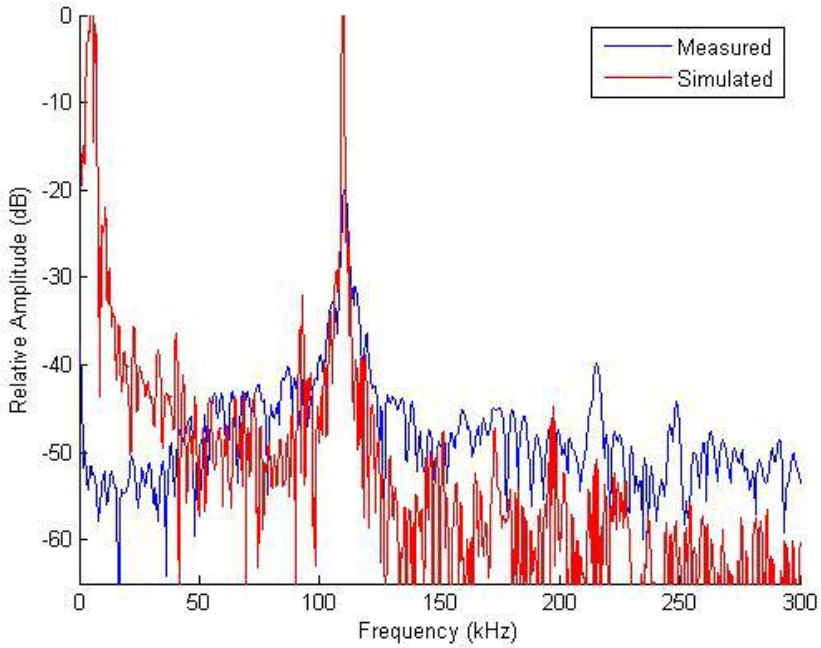

Figure 4.28: Beat frequency spectrum for delay line simulated target. The blue plot shows measured results and the red plot shows simulated results.

the cable. This multiple will not likely be seen during field experiments because the return power will not be nearly as strong as the power seen returning from the end of a low-loss coaxial cable. The spectrum shows the characteristic signs of amplitude modulation, which is evident when looking at the beat signal in the time domain. The side lobes created by amplitude modulation can be somewhat reduced after measurement during data processing. The leakage signals seen in the simulation are not present in the lab measurements due to the presence of the highpass filter.

A metal plate was used as a simulated target after the antenna was integrated into the system. Because nearly all the power is reflected back off the metal plate (some is scattered), the metal plate simulated target measurement was taken using a 20 dB attenuator placed before the antenna. Figure 4.29 shows the returned power from the metal plate. The multiple returns are due to the multiple reflections between the antenna and the metal plate, which will not take place when imaging the ice sheet. The results

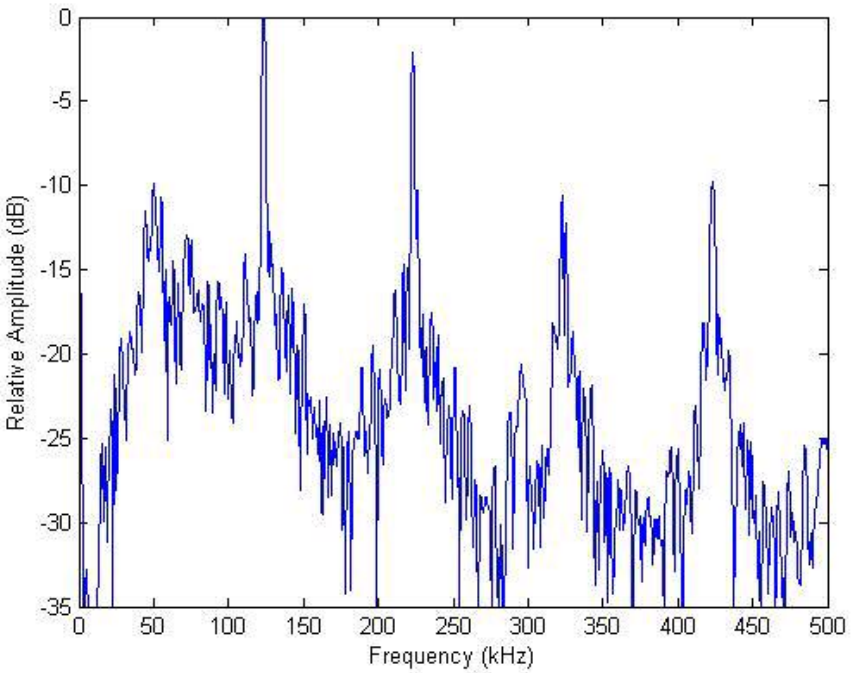

Figure 4.29: Beat frequency spectrum for metal plate simulated target.

show slightly more amplitude modulation than with the delay line test, which is reasonable since the antenna voltage standing wave ratio (VSWR) is not constant over the bandwidth of the antenna.

4.6.4 Target Medium Simulation

In order to make a comparison with data taken from the field experiment, a simulation has been run to estimate the returns from a given density profile. Due to computer memory restrictions, a brute force simulation could not be done; the 12 – 18 GHz transmit sweep would need a minimum of 36 million points. The FMCW radar interaction with the target medium was simulated with a step-frequency radar concept developed by Iizuka et al [11].

The characteristics of the near-surface firn were cataloged by David Braaten and Kirby Zimmerman during the field experiment in Greenland. Density measurements from two snowpits were taken with 5 cm resolution. The data collected were cataloged in a depth versus density profile. Matzler et al. [19] has shown that snow density can be related to a dielectric constant. The relationship between density and dielectric constant follows the expression:

$$\varepsilon_r = 1 + 1.7\rho + 0.7\rho^2 \qquad [4.2]$$

where ρ is the density of snow in g/cm^3. Using equation [4.2], the density information was converted into a depth versus dielectric constant profile. The reflection coefficient between adjacent layers can be calculated using equation [2.20].

A brief summary of the operation of step frequency radar is to record returns from a target at multiple frequencies, keeping track of the amplitude and phase information from each frequency step. The returns for each frequency step resemble the Fourier

transform, so taking the inverse Fourier transform will take the target back into the range bin domain, where the targets can be resolved into different range bins. Equations defined by Iizuka et al. have been modified to neglect the effect of spherical spreading and to account for the change in the velocity of light in firn layers of differing density.

The step frequency radar is stepped in increments of Δf a total of N times. The returns from each frequency step, H_n, are recorded. The return from the field is generated by the sum of all the scatterers:

$$H_n = \sum_{k=0}^{N-1} s_k E_o \exp\left[j4\pi \frac{f_o + n\Delta f}{c} \left(\sum_{i=0}^{k} \sqrt{\varepsilon_i} \right) \Delta z \right] \quad n = 0, 1, 2, \ldots, N\text{-}1 \qquad [4.3]$$

where s_k is the scattering from the target, f_o is the starting frequency, E_o is the amplitude of the transmit signal, ε is the relative dielectric constant of the target layer and Δz is the range bin size. Taking the inverse Fourier transform of H terms will yield an intensity measure, h_k, for each range bin. The intensity for each range bin can be found using the expression:

$$h_k = \sum_{n=0}^{N-1} H_n e^{-j2\pi \frac{kn}{N}} \qquad [4.4]$$

with the imposed condition:

$$\frac{2\Delta f N}{c} = 1 \qquad [4.5]$$

Information from the stratigraphy of the two snow pits was used to supplement the low resolution of the density data; the stratigraphy data showed places where thin ice crusts had accumulated. The results using data from two density profiles are shown in Figure 4.30 and Figure 4.31.

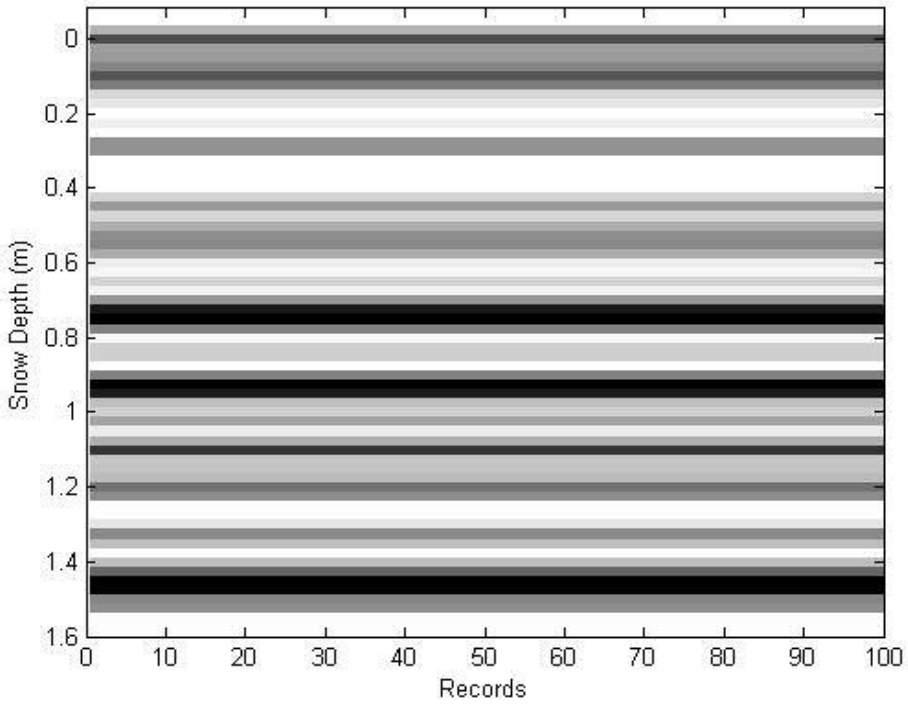

Figure 4.30: Simulated radar return from snowpit #2.

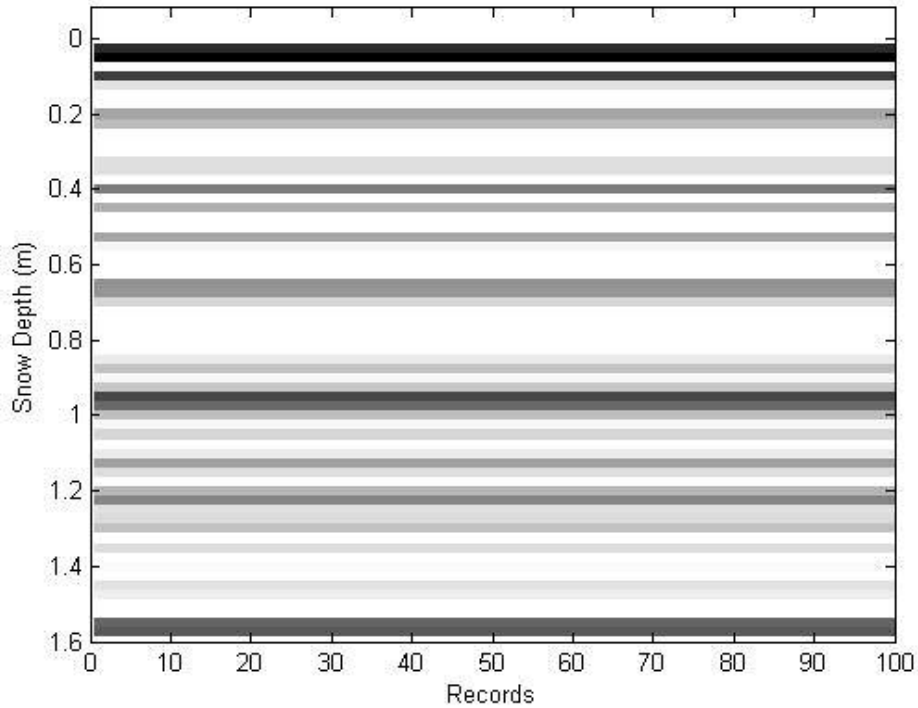

Figure 4.31: Simulated radar return from snowpit #3.

CHAPTER 5

DATA PROCESSING

5.1 Introduction

After the beat spectrum is digitized by the data acquisition system, the DAQ stores the beat signal information in binary files. A program is needed to decode the binary data file and retrieve information from the file, such as GPS data, signal data and time information. Although some of the signals recorded by the DAQ may look familiar and be somewhat recognizable to an electrical engineer, the data are far more useful in forms other than a time-domain signal, or even frequency-domain signal representation. The data processing software created in this thesis work uses processing algorithms developed by Kanagaratnam [14] and adapts them for use specific to the radar system in this thesis work. Furthermore, the data processing software has been developed to be usable by a person with little experience or knowledge about radar systems, and can easily be operated to produce quality image data.

5.2 Layer Image Formation

The end product of the data processing is an image that shows layering information from the near-surface layers, as in Figure 5.1. The radar image seen in Figure 5.1 is more than just a simple concatenation of intensity profiles; the final radar

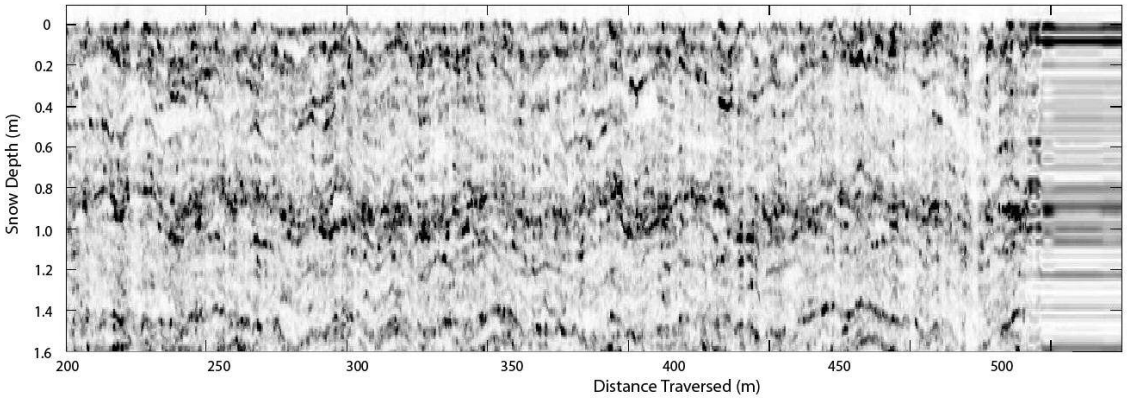

Figure 5.1: Radar image of near-surface layers.

image has been processed using mathematical domain transformations, filtering, system effect deconvolution, as well as image processing techniques such as median filtering and the use of level thresholds. The most significant steps in the data processing procedure are outlined as follows:

1. Read data from binary files.
2. Discard data taken during lock acquisition period.
3. Find radar point-spread-function using response from metal plate target.
4. Deconvolve system effects from data.
5. Apply Hanning window to the time-domain data.
6. Transform radar data to the frequency domain.
7. Perform coherent integration.
8. Construct a range profile.
9. Determine GPS location of data.
10. Filter and threshold image data.

After completion of the preceding steps, the image and data are saved to files. The data processing software has been developed in Matlab, and must be run in the Matlab operating environment.

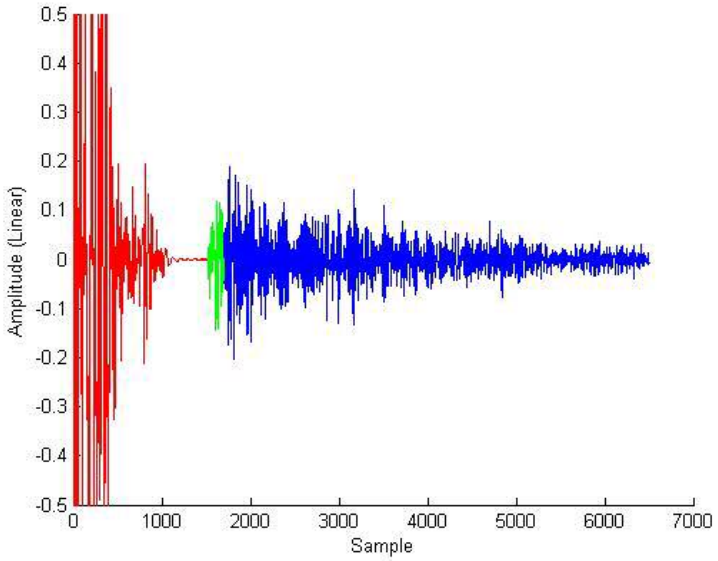

Figure 5.2: Typical radar beat signal recorded by the DAQ. Sweep recovery time (red), sweep lock acquisition (green), linear sweep (blue).

The data acquisition system stores the time-domain data in binary files and tags them with a GPS location and a time. The radar data contained in a binary is simply a single radar return, which has been digitized by the DAQ. Figure 5.2 shows a typical radar return in the time-domain. The first segment of the radar data contains erroneous data recorded during the sweep recovery time (red); the second segment of the data contains the beat spectrum obtained during the chirp. Not all of the data in the second segment are used for processing. The first part of the transmit sweep is relatively non-linear due to the high FM bandwidth associated with changing the locked VCO from a constant locked frequency to sweeping frequency (green). Figure 5.3 shows which parts of the radar data are used and unused. The red data plot shows data which will be used in processing; the blue will be discarded for processing. The user is prompted to verify the portion of data that will be used in processing. If the data set automatically selected does not seem to be consistent with the timing of the linear portion of the chirp, the user can choose to

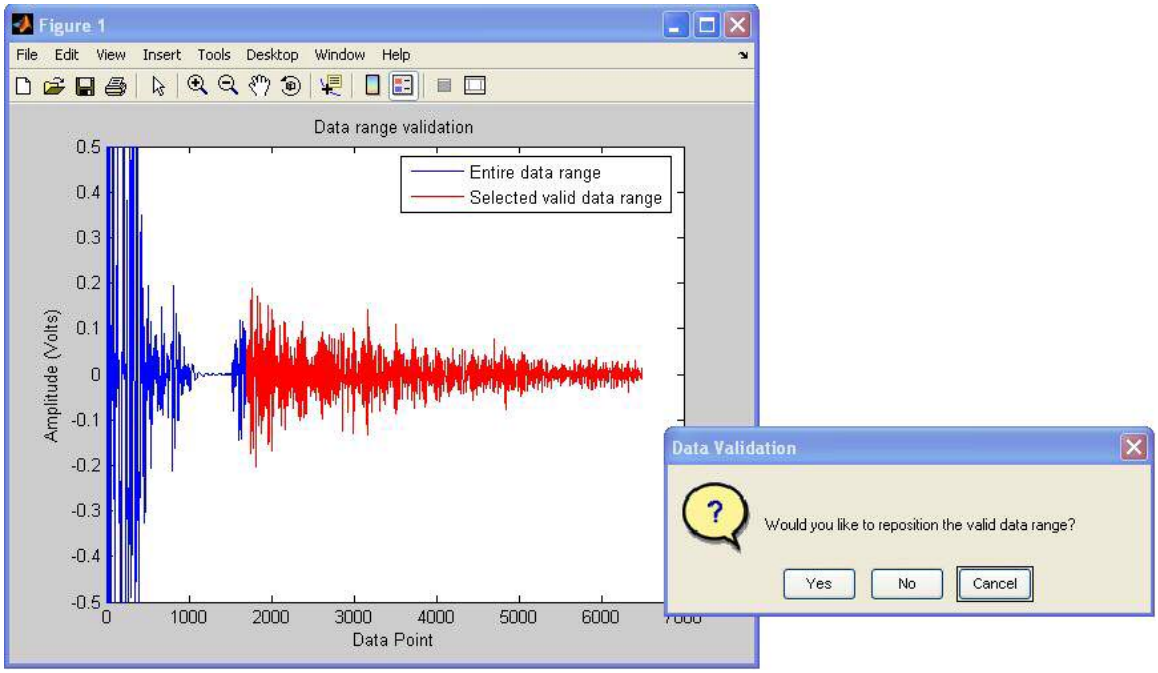

Figure 5.3: User entry screen for selecting most linear part of sweep.

manually define new start and stop points by graphically selecting the new bounds on the plot.

After the data set has been defined, the system effects of the radar are deconvolved from the radar data. The point-spread-function (PSF) of the radar is found by recording the return from a metal plate. Ideally, a metal plate target should return an exact replica of the transmit signal. To a large extent, any distortion in the response from the metal plate shows the transfer function, or point-spread-function, of the radar. Once the point-spread-function of the radar is found, it can be deconvolved out of the data. The metal plate return for this radar includes several reflections, as demonstrated in Figure 4.28. In order to extract only a single return from the metal plate, the beat signal is transformed to the time domain and filtered. Figure 5.4 shows the frequency-domain metal plate response and the filter transfer function used to extract only a single return from the metal plate. Transforming the single reflection back to the time domain shows

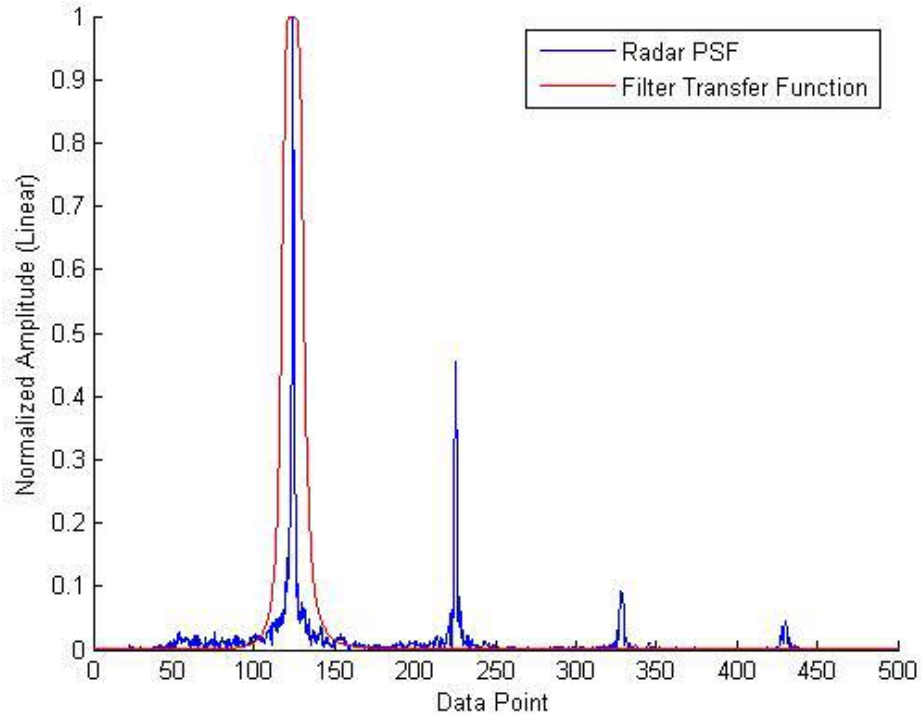

Figure 5.4: Metal plate response and filter transfer function.

the amplitude modulation imposed by the system. The envelope of the signal will reveal the amplitude-modulating signal spectrum. The envelope of the signal can be extracted using the Hilbert transform. The Hilbert transform is defined as follows:

$$\hat{x}(t) = \frac{1}{\pi} \int_{-\infty}^{\infty} \frac{x(\alpha)}{t-\alpha} d\alpha \qquad [5.1]$$

where α is a dummy integration variable. The envelope of the signal can be found in the absolute value of the Hilbert-transformed signal. The time-domain representation of the metal plate response and the corresponding envelope from the point-spread-function is shown in Figure 5.5. The envelope information is deconvolved out of the system to reduce amplitude modulation side lobes.

Since the beat frequency signal is time-limited, there will be frequency side lobes when the signal is transformed to the frequency domain. The side lobes for a single

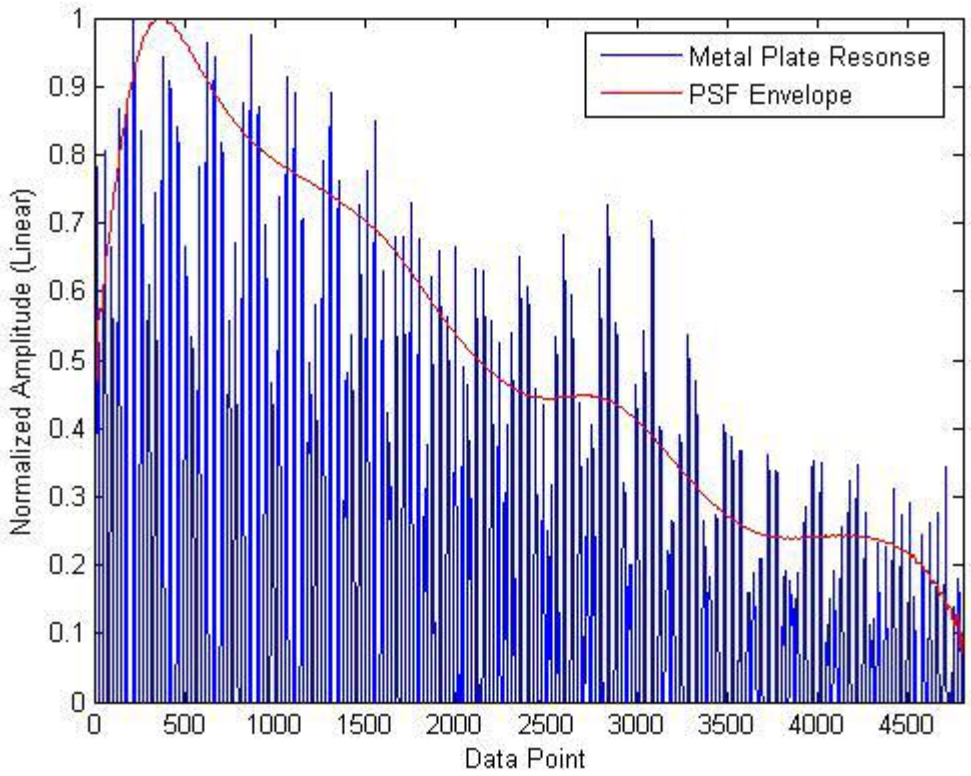

Figure 5.5: Time-domain metal plate response and PSF envelope.

frequency will be 13 dB below the main lobe. Multiplying the signal with a Hanning windowing function, while expanding the main lobe slightly, will reduce the side lobes to 32 dB below the main lobe.

After the system effects have been deconvolved from the data set and windowing has been applied, the time-domain beat signal is transformed into the frequency domain using the Fast Fourier Transform (FFT). The number of FFT points is calculated to be the nearest power of two that exceeds the number of time-domain data points. Figure 5.6 shows the zero-padded frequency-domain beat signal.

After the data are transformed to the frequency domain, the returns are integrated coherently. The number of integrations can be redefined in the program, but it is hard-coded to perform 10 coherent integrations.

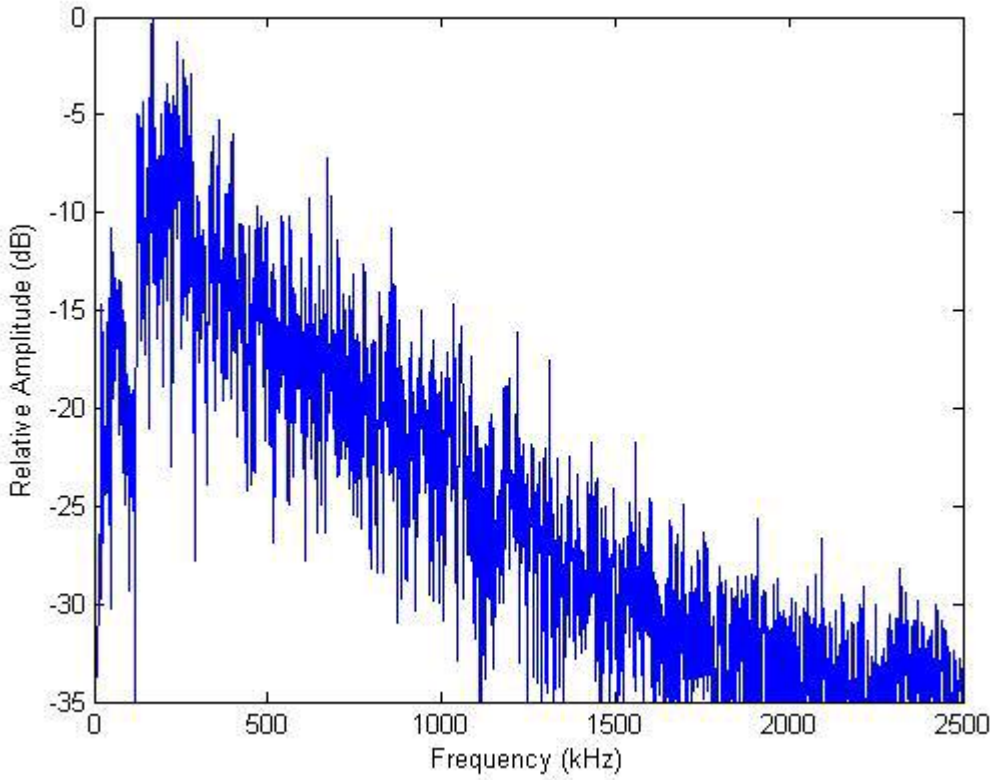

Figure 5.6: Beat signal in the frequency domain.

The range profile is derived using time-range bins and density data taken from ice cores and snowpits. Time and range bins can be derived from the number of points used in the data acquisition system and sampling frequency information. To assign a distance to a time bin, information about the target medium must be known. Since the radar beat frequency is derived from the time delay of the return signal, signal travel distance is dependent on the speed of the signal. The velocity of the electromagnetic energy is defined by the following equation:

$$v = \frac{c}{\sqrt{\varepsilon_r}} \qquad [5.2]$$

Preliminary range profiles used a single velocity of light based on an average dielectric

constant of 1.6, which is the estimated average dielectric constant of firn near the surface. A more accurate range profile has been constructed using density data. The near-surface density profile was assembled from data taken during the field experiment for this thesis work—from Summit, Greenland, in 2005. This profile covers depths up to about 2 m. Deeper density profiles, compiled from density data taken from GISP2 ice cores in 1994, supplement the near-surface profiles for depths below 2 m. The amalgamated dielectric profile is shown in Figure 5.7. The firn density starts at about 2 m, which accounts for the location of the antenna over the surface of the ice sheet. The range profile is constructed by the following equation:

$$r(n) = r(n-1) + \frac{c}{\sqrt{\varepsilon(n)}} \frac{t_{step}}{2} \qquad [5.3]$$

where t_{step} is the time extent of one range bin, and $r(n)$ is the depth of the n^{th} range bin.

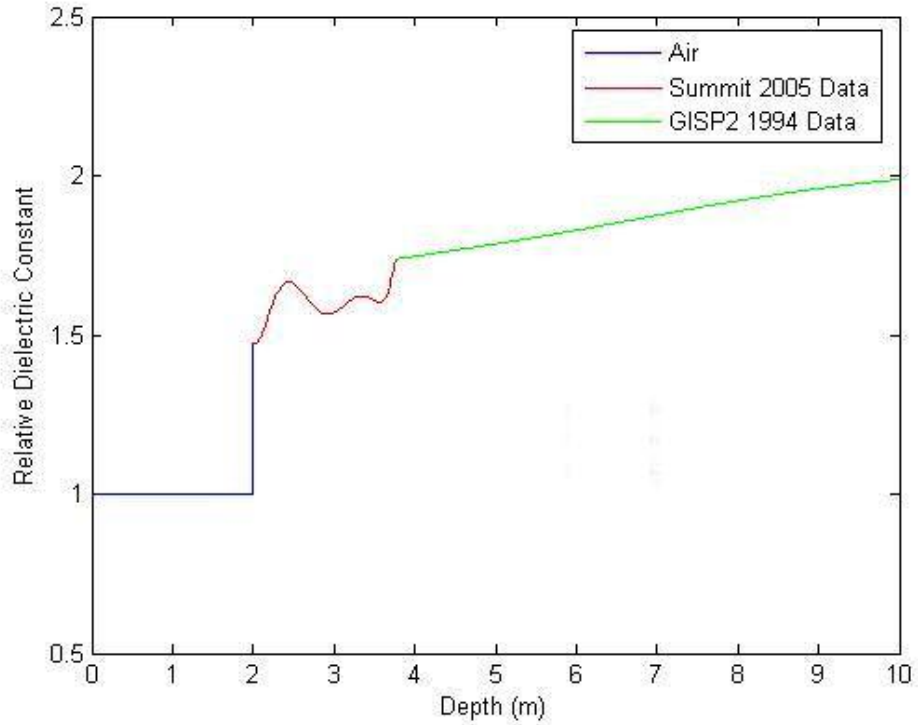

Figure 5.7: Dielectric profile compiled for developing a range profile.

Each set of radar returns has a GPS location attached to it. Using the GPS location information, distance between measurements, based on the Great Circle latitude and longitude algorithm, can be derived.

Image processing techniques, applying level thresholds and filtering, are employed to make layer visualization easier before the image is stored to disk. Applying thresholds to the image helps layer visualization by utilizing the intensity range of the image more efficiently. Without applying thresholds, noise and extremely strong returns are factored into the intensity scale. Raising the threshold floor and lowering the threshold ceiling improves the visualization of weaker layer returns, and reduces much of the noise. A median filter is used to smooth the image over the horizontal axis. This provides more layer continuity. Using a median filter that takes two pixels from previous data and two pixels from subsequent data improves layer permanence without greatly sacrificing resolution in layer details.

5.3 Determination of Accumulation Rate

One significant finding of this thesis work is the variation of the accumulation over distances. A program has been developed in Matlab which allows layers to be tracked and corresponding accumulations accurately calculated. The program is designed with the intention to allow users with no background in Matlab to operate the software.

The program relies on considerable user discretion to identify the layers, but uses GPS data to calculate distances and the same range profile developed for layer image forming. The program asks the user to identify the top layer with 50 points. The programs recalls an image (processed with the layer imaging software) and waits for the

user to input a layer definition by clicking the mouse over points on the layer. After 50 points are collected, the user is asked if 50 more points are needed to define the layer. The same routine is used to define the second layer. After the upper and lower layers are defined, the difference of the two layers determines the accumulation. An example of the layer tracking algorithm can be seen in Figure 5.8.

Since the layer tracking is completely user dependent and the annual accumulation is calculated by finding the difference between the two defined layers, the user must know how to identify boundaries between annual layers. The output of the program is a matrix, which contains depth and distance information for both layers that can be used at the user's discretion.

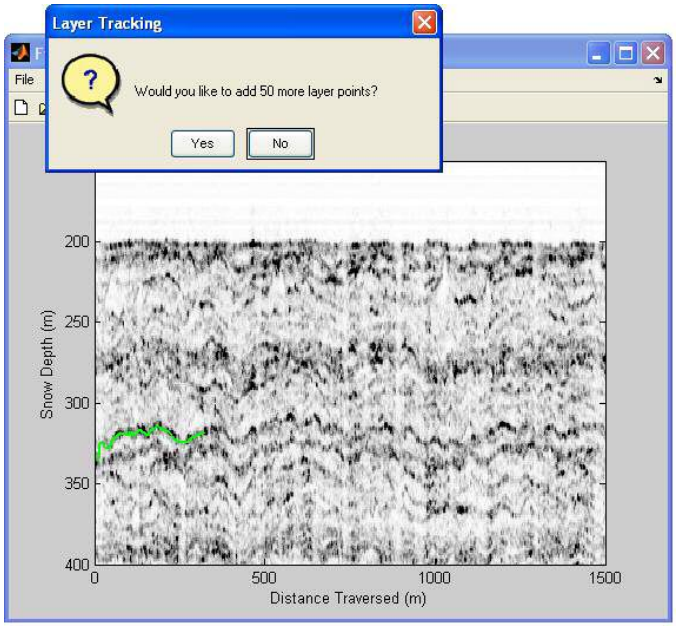

Figure 5.8: Example of layer definition process. The green line shows the currently defined layer.

CHAPTER 6

FIELD EXPERIMENT

6.1 Introduction

The radar system was successfully tested at the Summit camp, Greenland, in July 2005. A large amount of data was collected from various locations around Summit camp. The locations include areas adjacent to bamboo stakes measured either weekly or monthly throughout the year to track snow accumulation. Additionally, four snowpits were dug to compare radar data with actual stratigraphy and density. More than 200 sample traces were collected to compare with the snowpit observations. Each sample trace uses 10 sweeps, which are coherently integrated to improve signal-to-noise ratio. The average snow density was used to determine the dielectric constant, which enables the estimation of the propagation velocity in firn. The results show a high correlation between the snow pit stratigraphy and reflecting layers mapped with the radar. Returns from layers were observed with the radar operated at a single spot, and with the radar traveling at a nearly constant speed along a line over a distance in excess of 4 km.

6.2 Measurements Taken in Summit, Greenland

Summit Camp, Greenland, is located at the highest point on the Greenland ice sheet. The location of Summit Camp is shown on the map in Figure 6.1. Measurements

Figure 6.1: Map of Greenland with Summit Camp marked [8].

were taken outside of the camp area, on paths of undisturbed snow. Most of the measurements were taken in motion, while other measurements were taken while stationary in order to verify stratigraphy at that location.

Mobile measurements were taken with the radar towed by a snowmobile. An example of the radar taking a measurement in motion can be seen in Figure 6.2. Data

Figure 6.2: Radar system taking measurements while mobile.

were taken on six days between July 17 and July 24, 2005. Data taken during the first two days were used for preliminary system evaluation, while data taken on the last four days were used to evaluate the success of the system and obtain useful information about the near-surface layers. A sample of raw radar, the beat frequency spectrum, can be seen in Figure 6.3. These data still contain the effects of amplitude modulation. The only processing done on the data set in Figure 6.3 is windowing using a Hanning window and using the fast Fourier transform (FFT) to display the data in the frequency domain. The beat spectrum shows strong layer reflections throughout the data set. A trend of amplitude reduction is seen, which is caused by the expected attenuation from the firn. The feed-through signal from low circulator isolation is seen in the lower portion of the spectrum, and is properly attenuated, preventing the strong return from masking the surface return and nearby layers.

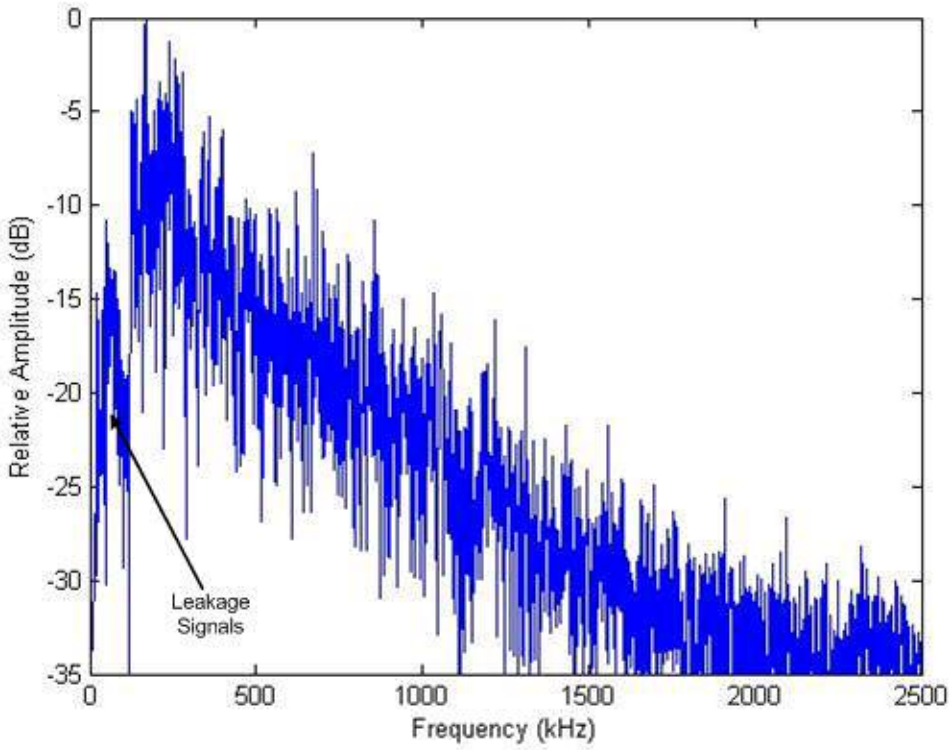

Figure 6.3: Beat spectrum from near-surface layers. Data taken on July 22.

After data processing, an image is formed by concatenating the data taken over a length. GPS data is taken with each measurement, so it is possible to mark each return to a location and display a distance after concatenating the data. Examples of measurements taken in motion can be seen in Figure 6.4 and Figure 6.5. These images are derived from radar data taken preceding the locations of snowpit number two and snowpit number three. The images in Figure 6.4 and Figure 6.5 have undergone many data processing steps, including system deconvolution and range correction based on snow density. The image shows that many layers are being resolved, and single layers can be tracked throughout the length of the measurement. The data also shows that the annual layers, marked by hoar layers (dark lines), have significant depth variation associated with them.

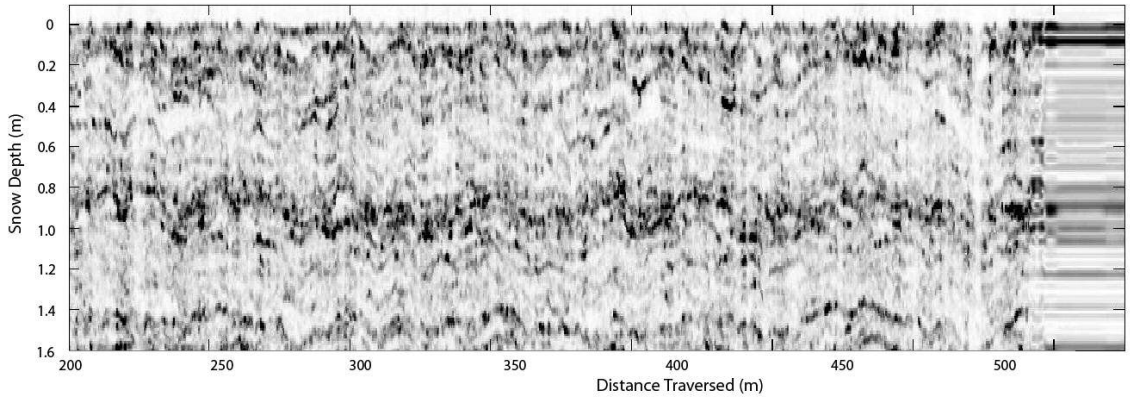

Figure 6.4: Measurement taken in motion, preceding snowpit #2.

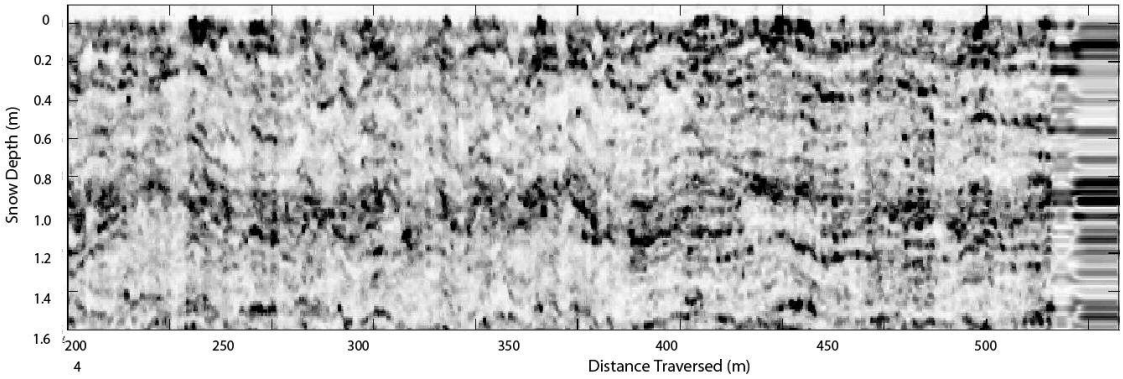

Figure 6.5: Measurement taken in motion, preceding snowpit #3.

This observation is significant because it shows that the yearly accumulation rate measured can be dependent on the measurement location.

Stationary measurements were taken to verify the proper operation of the radar. During several mobile measurements, the radar was stopped to take stationary data. The spot where stationary data was taken was marked so that a snowpit could be dug in that location. Snowpits were dug in four separate locations to depths of between 1.8 and 2.2 m. In two of the snowpits, only stratigraphy and temperature data were taken; in the other two pits, stratigraphy, temperature and density information were taken. Density information was taken by removing a known volume sample from the firn at 5 cm intervals and weighing it. The snow was placed in individually weighed plastic bags. The weight measurement was taken at the time of sample and was measured to the nearest tenth of a gram. The weight of the plastic bag was subtracted from the measured weight. Stratigraphy information was taken by cleaning one wall of the snowpit and fixing a meter stick to the snow wall to measure depth. This process is pictured in Figure 6.6. Layer location was detailed to an accuracy of 0.5 cm. Figure 6.7 shows a plot

Figure 6.6: Snowpit with cleaned wall and meter stick for measurement.

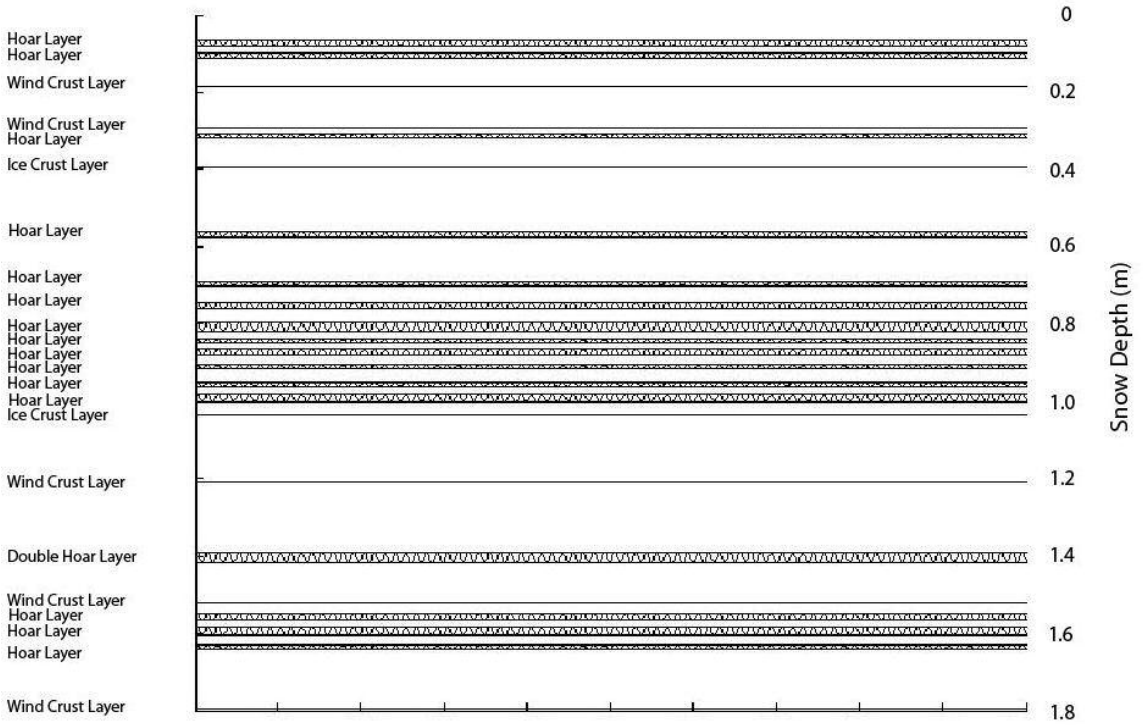

Figure 6.7: Stratigraphy data from snowpit #2. Crosshatched layers represent hoar layer boundaries.

detailing stratigraphy location and layer composition of snowpit number two.

6.3 Accumulation Rate Measurements

The accumulation data is derived from the layer data taken by the radar. Zebker et al. [23] have shown that hoar layers can be used to define annual accumulation boundaries. The annual hoar layers are some of the most distinct layers found in the radar images. Figure 6.4 and Figure 6.5 illustrate that hoar layers can be tracked over a distance. Using software developed in Matlab, the accumulation rate, as defined by hoar layer boundaries, can be determined and tracked over distances. Figure 6.8 shows a radar image through which hoar layers have been tracked. The upper hoar layer is marked in blue, while the lower hoar layer is marked in red. Taking the difference between the

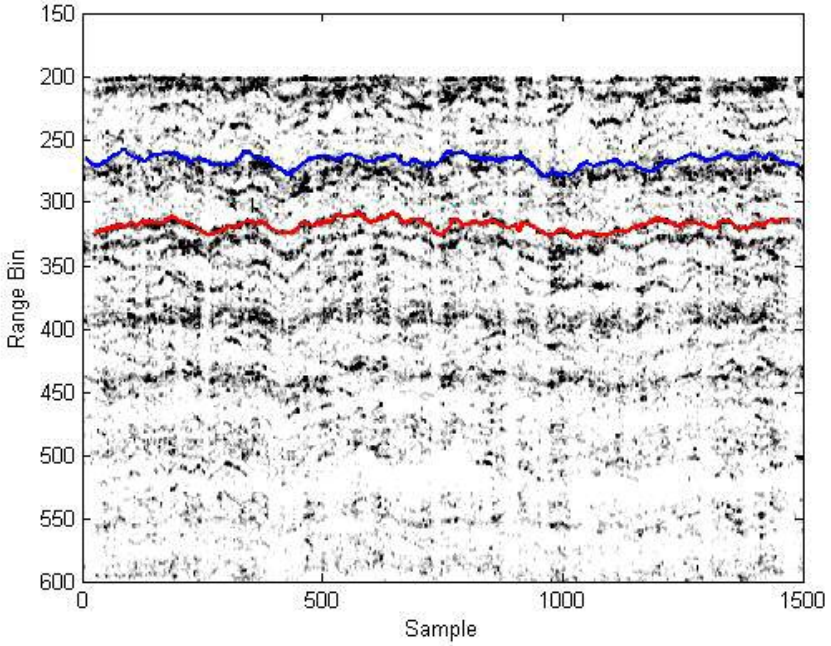

Figure 6.8: Image of near-surface layers with two hoar layers marked.

depths of the upper and lower layer gives an estimate of the accumulation rate. Figure 6.9 shows a plot of accumulation depth, as defined by in Figure 5.8. Hoar layer depth for the year shown reveals an RMS accumulation 62 cm. Other layers seen below the defined layers in Figure 6.8 also yield accumulation estimates of around 60 cm.

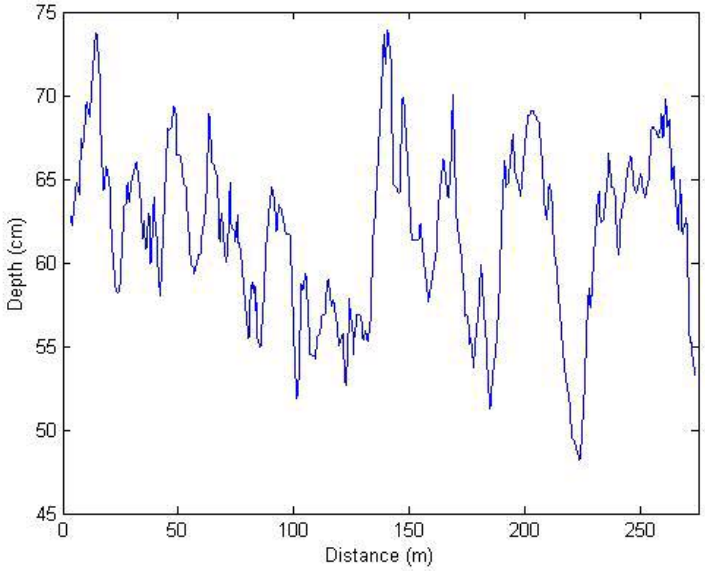

Figure 6.9: Accumulation rate derived from layer tracking.

6.4 Analysis of Results

A standard for comparison has to be obtained in order to evaluate the performance of the radar system. Several different standards were developed to determine the quality of data obtained from radar measurement for both stationary and mobile measurements.

It is relatively intuitive to establish a standard of comparative evaluation for stationary measurements. Stationary measurements were taken and locations marked. Following the stationary measurements, the area illuminated was excavated to obtain stratigraphy, temperature and density information about the near-surface layers. This information was used for direct comparison to radar images formed. In addition, the density information from the snowpit was used to form a model for the expected signal return from the firn.

Much of the validity of mobile measurements rests on the performance of the radar while taking stationary measurements. It can be generally concluded that if the radar is accurately representing layer information during stationary measurements, then it is likely mapping layers correctly while taking mobile measurements. Additionally, accumulation rates for the geographical vicinity are known, and can be compared with radar imagery.

Radar images compared with both stratigraphy and propagation models showed almost one-to-one matching throughout the near-surface layers. Figure 6.10 and Figure 6.11 show a comparison of mobile and stationary measurements, as well as stratigraphy and propagation model predictions. Although the matching between the propagation model is not one-to-one, there is a high correlation between the returns seen in the stationary radar data and the returns in the propagation model.

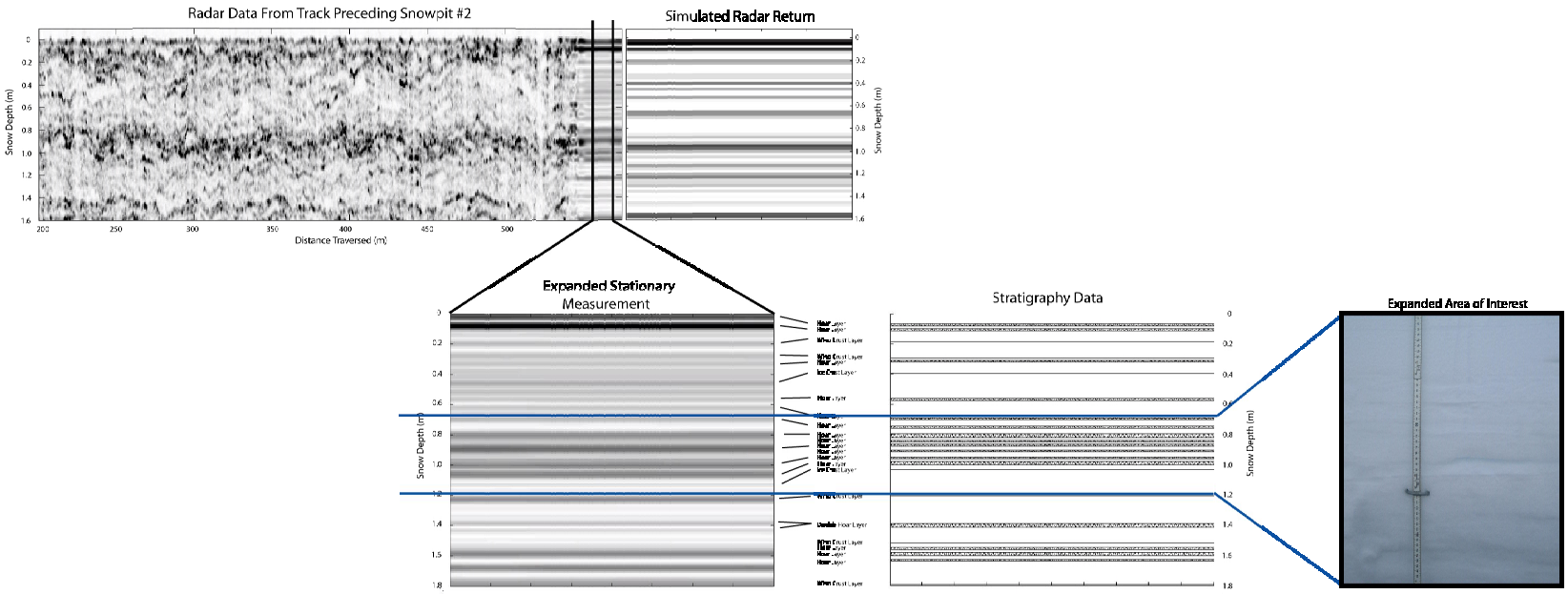

Figure 6.10: Data from snowpit #2. Chart shows mobile and stationary radar images, as well as stratigraphy and propagation model.

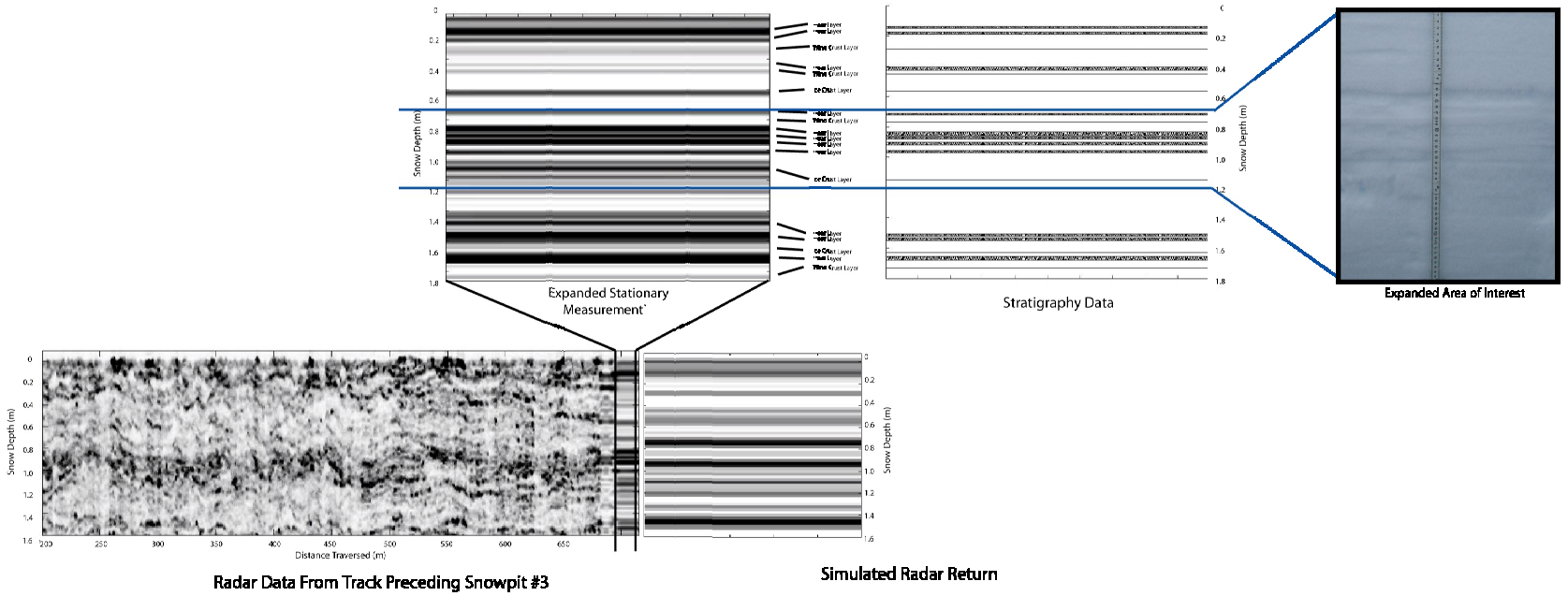

Figure 6.11: Data from snowpit #3. Chart shows mobile and stationary radar images, as well as stratigraphy and propagation model.

The mobile measurements support findings by other researchers that accumulation tends to be about 65 cm/yr in similar locations [5]. Dibb et al. have shown accumulation in a known measurement location, where accumulation can be measured against an array of 100 stakes, to be about 65 cm/yr with an approximate error window of ± 5 cm. Measurements taken with the radar in this thesis work show an RMS accumulation of 62 cm. A significant finding supported by this thesis work is that accumulation thickness can vary significantly from location to location. Figure 6.9 demonstrates that depending on the location of measurement, an accumulation estimate can vary more than 20 cm from the mean accumulation. Figure 6.12 highlights this variance in accumulation by providing a zoomed view of Figure 6.9, showing the accumulation thickness over the distance of 50 m. According to data taken in Greenland shown in Figure 6.9, accumulation measurements have a standard deviation of more than 5 cm (8.1%) from the mean accumulation.

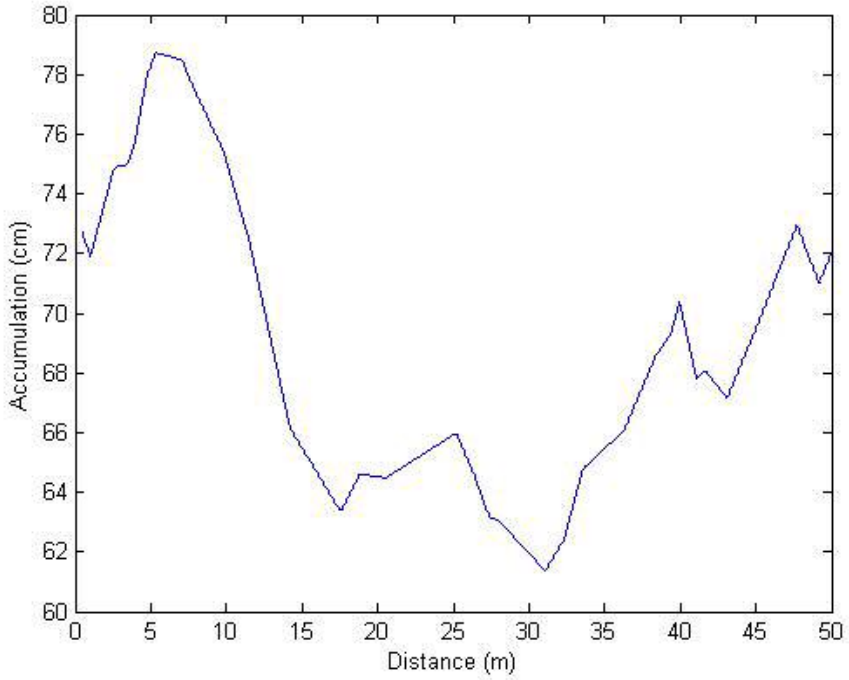

Figure 6.12: Accumulation thickness variation over 50 m.

CHAPTER 7

CONCLUSIONS AND FUTURE WORK

7.1 Conclusions

A mobile radar with the capability to image near-surface layers with fine resolution has been developed and evaluated. The radar uses plane-wave illumination and a bandwidth of 6 GHz at a center frequency of 15 GHz to achieve a resolution of about 3 cm. A sled has been developed to compensate for changes of the terrain, which allows the radar to consistently receive specular returns and avoid most energy from incoherent sources. The system was developed and simulated in software such as Advanced Design System and Matlab. The models obtained from the simulations were used to evaluate the performance of the system, and laboratory measurements found the system to meet or exceed the requirements for detecting near-surface internal layers in polar ice sheets.

The radar was field tested in Summit, Greenland, during the 2005 field season. Results showed that the radar is capable of tracking many internal layers within the near-surface firn. The data obtained from the Greenland field experiment also demonstrates that accumulation depth measurements can be highly dependent on the location of measurements, with deviations from RMS accumulation exceeding 20%.

7.2 Future Work

Although the radar system is completely functional and is capable of regular use in field experiments, modifications can be made to improve performance in certain areas. Two of the most significant areas are the motion compensation system and the frequency synthesizer. Other improvements include improving the environmental stability of the radar, and increasing the sophistication of the layer tracking and accumulation profiling program.

One factor that limits the velocity at which the radar can be pulled is the PRF. The maximum velocity at which the radar can travel is governed by equation [3.13], which states that the maximum velocity of a mobile, monostatic radar system is directly proportional to the PRF. Increasing the PRF would allow the radar to travel faster, but increasing the PRF also means decreasing the sweep time of the transmit chirp. In the current configuration, decreasing the chirp time introduces unacceptable frequency modulation into the transmit sweep. This can be compensated by tightening the loop filter in the PLL, but doing so causes the recovery time (the time between end of the sweep at 18 GHz and start of the next sweep at 12 GHz) to exceed half the cycle time. A proposed circuit modification is currently under development at the University of Kansas to allow switching of the loop filter bandwidth for the different stages of the chirp—allowing a tight loop filter to govern the bandwidth during sweep time, while allowing a much looser filter to permit quick recovery to the starting frequency.

The velocity of the sled may also be increased by the installation of a more responsive terrain compensation system. The tilt sensor is too sensitive to acceleration events to allow unfiltered tilt data to be used in antenna pointing. Limiting the bandwidth

provides a more accurate tilt measurement; but after filtering, the tilt measurement is delayed, causing the sled to compensate for terrain travel some time previous to it. The terrain compensation system could benefit by the addition of two quick acting, low-noise gyroscopes. A proposed design exists, along with partial implementation.

Overall stability of the radar could be improved by compensating changes in the environment. The radar is operated in both the northern and southern poles, where conditions can vary significantly. Although temperatures during the field season in Greenland do not push system components to their lower limit, temperatures in Antarctica may cause the system to malfunction. Future work to improve the environmental stability of the radar should investigate which components are sensitive to temperature and design ways of maintaining those components at a steady temperature.

Although the accumulation tracking software is functional, the implementation is crude and lacking sophistication. The annual layers are defined manually, using graphical input from a user, which is time consuming. An algorithm implementing a Gaussian highpass image filter could expose only strong layer returns—likely to be hoar layers, which create annual accumulation boundaries. The filtered image could facilitate automated layer tracking algorithms already in use at the University of Kansas.

REFERENCES

[1] Akins, T. Private Communication. Lawrence, KS, 2005.

[2] Arcone, Steven A., Vandy B. Spikes, Gordon S. Hamilton and Paul A. Mayewski. "Stratigraphic Continuity in 400 MHz Short-Pulsed Radar Profiles of Firn in West Antarctica." *Annals of Glaciology*. Vol. 39. 2004.

[3] Berdow, J., R. Porco, A.K. Fung, S. Tjuatja, K. Jezek, S.P. Gogineni, A.J. Gow. Determination of Volume and Surface Scattering from Saline Ice Using Ice Sheets with Precisely Controlled Roughness Parameters." *IEEE Transactions on Geoscience and Remote Sensing*. Vol. 33, No. 5. 1995.

[4] Davis, Curt H., Yonghong Li, Joseph R. McConnell, Markus M. Frey and Edward Hanna. "Snowfall-Driven Growth in East Antarctic Ice Sheet Mitigates Recent Sea-Level Rise." *Science*. Vol. 308, 2005.

[5] Dibb, Jack E., and Mark Fahnestock. "Snow Accumulation, Surface Height Change, and Firn Densification at Summit, Greenland: Insights from 2 Years of In Situ Observation." *Journal of Geophysical Research*. Vol. 109. 2004.

[6] ESA – Living Planet Programme – CryoSat. http://www.esa.int/esaLP/LPcryosat.html

[7] Gogineni, S., T. Chuah, C. Allen, K. Jezek and R.K. Moore. "An Improved Coherent Radar Depth Sounder." *Journal of Glaciology*. Vol. 44, No. 148, 1998.

[8] Greenland Summit Camp, http://www.summitcamp.org/

[9] Griffiths, H.D., "The Effects of Phase and Amplitude Errors in FM-Radar"

[10] ICESAT Web Page. http://icesat.gsfc.nasa.gov/

[11] Iizuka, Keigo, Alois P. Freundorfer, Kam Hung Wu, Hirotaka Mori, Hisanao Ogura, and Van-Khai Nguyen. "Step Frequency Radar." Journal of Applied Physics. Vol. 56, No. 9. 1984.

[12] Johnson, R.C. and D.W. Has, "Performance of a Compact Antenna Range." *Digest IEEE International Symposium on Antennas and Propagation*, 1975.

[13] Kanagaratnam, P. “High-Resolution Radar Backscatter from Sea Ice and Range-Gated Step-Frequency Radar Using the FM-CW Concept.” M.S. Thesis, Electrical Engineering and Computer Science, The University of Kansas, 1995.

[14] Kanagaratnam, P. “Airborne Radar for High-Resolution Mapping of Internal Layers in Glacial Ice to Estimate Accumulation Rate.” Ph.D. Dissertation, Electrical Engineering and Computer Science, The University of Kansas, 2003.

[15] Kanagaratnam, Pannir. Private Communication, Lawrence, KS. 2005.

[16] Knight, P.G. *Glaciers*. Routledge: Oxford, UK, 1999.

[17] Leysinger Vieli, Gwendolyn, Martin J. Siegert and Antony J. Payne. “Reconstructing Ice Sheet Accumulation Rates at Ridge B, East Antarctica.” *University of Bristol*.

[18] Massom, Robert A., Hajo Elcken, Christian Haas, Martin O. Jeffries, Mark R. Drinkwater, Matthew Sturm, Anthony P. Worby, Xingren Wu, Victoria I. Lytle, Shuki Ushio, Kim Morris, Phillip A. Reid, Stephen G. Warren and Ian Allison. “Snow on Antarctic Sea Ice.” *Reviews of Geophysics*. Vol. 39, No. 3. August, 2001.

[19] Matzler, Christian. “Microwave Permittivity of Dry Snow.” *IEEE Transactions on Geoscience and Remote Sensing.* Vol. 34, No. 2. 1996.

[20] Munk, J., K.C. Jezek, R.R. Forster and S.P. Gogineni. “An Accumulation Map for the Greenland Dry-Snow Facies Derived from Spaceborne Radar.” *Journal of Geophysical Research*. Vol. 108, No. D9, 2003.

[21] National Geographic News. http://news.nationalgeographic.com/news/2004/11/1109_041109_polar_ice.html, Handwerk, B., “Arctic Melting Fast; May Swamp U.S. Coasts by 2099.”

[22] National Geographic News. http://news.nationalgeographic.com/news/2004/04/0420_040420_earthday.html, Lovgren, S., “Warming to Cause Catastrophic Rise in Sea Level?”

[23] Oveisgharan, Shadi and Howard A. Zebker, “Estimating Snow Accumulation from InSAR Correlation Observations.” *Stanford University*. 2005.

[24] Paden, John. Private Communication. Lawrence, KS. 2004.

[25] Paren, J. G. and G. de Q. Robin. “Internal Reflections in Polar Ice Sheets.” *Journal of Glaciology*, Vol. 14, No. 71. 1975.

[26] Parthasarathy, R. "A Fine-Resolution Radar for Near-Surface Layer Mapping." M.S. Thesis, Electrical Engineering and Computer Science, The University of Kansas, 2003.

[27] Pistorius, Carl W.I. and Walter D. Burnside. "An Improved Main Reflector Design for Compact Range Applications." *IEEE Transactions on Antennas and Propagation*. Vol. AP-35, No. 3. 1987.

[28] Pozer, David M. *Microwave Engineering*. John Wiley & Sons, Inc. 1997.

[29] Remcom, http://www.remcom.com/examples/xfdtdexampleDetailUpdated.php?exampleID=72&thisProduct=XFDTD%20v6, "XFDTD v6 Example: Horn Antenna."

[30] Vickers, R. S., and G. C. Rose. "High Resolution Measurements of Snowpack Stratigraphy Using a Short Pulse Radar." *Proceedings of the Eighth International Symposium on Remote Sensing of Environment*. Vol. 1, pp. 261-267, Ann Arbor, Michigan, October 2-6, 1972.

[31] Wehner, D.R. *High-Resolution Radar 2nd Edition*, Artech House: Norwood, MA, 1995.

[32] Winebrenner, Dale P. and Robert J. Arthern. "Mapping Greenland Accumulation Rates Using Observations of Thermal Emission at 4.5-cm Wavelength." *Journal of Geophysical Research*. Vol 106, No. D24, 2001.

[33] Wingham, D.J., and the CryoSat Science Advisory Group. "CryoSat Calibration & Validation Concept. Doc. CS-PL-UCL-SY-0005." November 14, 2001.

[34] Colbeck, Samuel C., J. Bruce Jamieson. "The Formation of Faeted Layers Above Crusts." *Cold Regions Science and Technology*. Vol. 33. 2001.

[35] Pfeffer, W.T., R. Mrugala. "Temperature Gradient and Initial Snow Density as Controlling Factors in the Formation and Structure of Hard Depth Hoar." *Journal of Glaciology.* Vol. 48, No. 163, 2002.

[36] Steffen, K., W. Abdalati, I. Sherjal. "Faceted Crystal Formation in the Northeast Greenland Low-Accumulation Region." *Journal of Glaciology*. Vol. 45, No. 149, 1999.